

**DEVELOPMENT OF PORTABLE ELECTRONIC NOSE
BASED ON NANOSTRUCTURE GAS SENSORS**

CHATCHAWAL WONGCHOOSUK

**A THESIS SUBMITTED IN PARTIAL FULFILLMENT
OF THE REQUIREMENTS FOR THE DEGREE OF
DOCTOR OF PHILOSOPHY (PHYSICS)
FACULTY OF GRADUATE STUDIES
MAHIDOL UNIVERSITY
2011**

COPYRIGHT OF MAHIDOL UNIVERSITY

Thesis
entitled
**DEVELOPMENT OF PORTABLE ELECTRONIC NOSE
BASED ON NANOSTRUCTURE GAS SENSORS**

.....
Mr. Chatchawal Wongchoosuk
Candidate

.....
Asst. Prof. Teerakiat Kerdcharoen,
Ph.D.
Major advisor

.....
Mr. Adisorn Tuantranont,
Ph.D.
Co-advisor

.....
Mr. Anurat Wisitsoraat,
Ph.D.
Co-advisor

.....
Prof. Banchong Mahaisavariya,
M.D., Dip. Thai Board of Orthopedics
Dean
Faculty of Graduate Studies
Mahidol University

.....
Assoc. Prof. Wannapong Triampo,
Ph.D.
Program Director
Doctor of Philosophy Program in
Physics
Faculty of Science, Mahidol University

Thesis
entitled
**DEVELOPMENT OF PORTABLE ELECTRONIC NOSE
BASED ON NANOSTRUCTURE GAS SENSORS**

was submitted to the Faculty of Graduate Studies, Mahidol University
for the degree of Doctor of Philosophy (Physics)

on
January 14, 2011

.....
Mr. Chatchawal Wongchoosuk
Candidate

.....
Prof. Margit Zacharias,
Ph.D.
Member

.....
Assoc. Prof. Pisith Singjai,
Ph.D.
Chair

.....
Asst. Prof. Supab Choopun,
Ph.D.
Member

.....
Asst. Prof. Teerakiat Kerdcharoen,
Ph.D.
Member

.....
Mr. Anurat Wisitsoraat,
Ph.D.
Member

.....
Mr. Adisorn Tuantranont,
Ph.D.
Member

.....
Prof. Banchong Mahaisavariya,
M.D., Dip. Thai Board of Orthopedics
Dean
Faculty of Graduate Studies
Mahidol University

.....
Prof. Skorn Mongkolsuk, Ph.D.
Dean
Faculty of Science
Mahidol University

ACKNOWLEDGEMENTS

The success of this thesis can be attributed to the extensive support and assistance from my major advisor, Assist. Prof. Teerakiat Kerdcharoen and my co-advisor, Dr. Anurat Wisitsoraat, and Dr. Adisorn Tuantranont. I am grateful to them for their valuable advice, encouragement and guidance in this research.

I am deeply grateful to Prof. Margit Zacharias, Head of Laboratory for Nanotechnology, IMTEK, University of Freiburg, Freiburg, Germany, for giving me the very good opportunity to do the research in her group and for her detailed and constructive comments in ZnO nanowire works.

I wish to express my warm and sincere thanks to Prof. Stephan Irle, Head of Quantum Chemistry Group, Department of Chemistry, Nagoya University, Nagoya, Japan, and Prof. Keiji Morokuma, Research Leader of Fukui Institute for Fundamental Chemistry, Kyoto University, Kyoto, Japan, for giving me the very good opportunity to do the research in Nagoya University, Japan, and for their detailed and constructive comments in molecular modeling works.

I deeply thank Mr. Kittitat Subannajui and Mr. Andreas Menzel, Ph.D students of IMTEK, University of Freiburg, Freiburg, Germany, who taught and helped me a lot of things related to nano fabrication process, especially ZnO nanowire growth.

I wish to thank Mr. Mario Lutz, Ph.D student of Materials Science and Engineering Programme, University of Mahidol, for his comments in LabVIEW programming and E-nose systems.

I would like to thank my friends at Thai Student Club in Freiburg Germany, at IMTEK, Germany, at Quantum Chemistry Group, Nagoya University, Japan, and at the Center of Nanoscience and Nanotechnology, Faculty of Science, Mahidol University, Thailand for their kind support and cheerfulness.

The financial support of the Commission on Higher Education for a Ph.D. scholarship under the program “Strategic Scholarships for Frontier Research Network” is gratefully acknowledged.

Finally, I am grateful to my family for their encouragement entirely care, and love. The usefulness of this thesis, I dedicate to my mother, father, elder sister and all the teachers who have taught me since my childhood.

Chatchawal Wongchoosuk

**DEVELOPMENT OF PORTABLE ELECTRONIC NOSE BASED ON
NANOSTRUCTURE GAS SENSORS****CHATCHAWAL WONGCHOOSUK 5037004 SCPY/D****Ph.D. (PHYSICS)****THESIS ADVISORY COMMITTEE : TEERAKIAT KERDCHAROEN, Ph.D.
ADISORN TUANTRANONT, Ph.D., ANURAT WISITSORAAT, Ph.D.****ABSTRACT**

This thesis provides broad knowledge and deep understanding of various topics of nanotechnology including (I) atomistic model of a nanostructure, (II) synthesis of the large scale homogenous ZnO nanostructures, (III) fabrication of nanostructure gas sensors, and (IV) invention of a portable electronic nose (E-nose). For modeling work, the formation mechanism of silicon carbide nanotubes (SiCNTs) has been investigated by using the DFTB method. The results show the important role of defects on the side wall of tubes. The SiCNTs prefer to form sp^2 bonds between a Si atom and a C atom. In case of ZnO nanostructures growth, a shape diagram of ZnO nanostructures grown by thermal evaporation has been presented. The roles of substrate temperature and powder source temperature in the evolution of the ZnO morphology and the mechanisms leading to the different morphologies have been highlighted. For gas sensor works, fabrication of nanostructured gas sensors, including WO_3 , SnO_2 , CNT- WO_3 , CNT- SnO_2 prepared using electron beam evaporation by means of the powder mixing, have been reported. Doping of CNTs can enhance sensitivity and selectivity of metal oxides gas sensors and can also reduce operating temperature. In the last work, a portable E-nose based on hybrid gas sensors with new feature extraction methods has been described. The results show the E-noses can be widely used for many applications such as quality control of foods and beverages, air protection and human identification. It is hoped that this thesis will have many uses ranging from basic research to industrial applications.

**KEY WORDS: E-NOSE / DFTB / ZNO NANOSTRUCTURES /
NANOTECHNOLOGY / ODOR**

131 pages

การพัฒนาจมูกอิเล็กทรอนิกส์แบบพกพาได้บนพื้นฐานของก๊าซเซนเซอร์ที่มีโครงสร้างแบบนาโน
DEVELOPMENT OF PORTABLE ELECTRONIC NOSE BASED ON NANOSTRUCTURE GAS SENSORS

ชัชวาล วงศ์ชูสุข 5037004 SCPY/D

ปร.ด. (ฟิสิกส์)

คณะกรรมการที่ปรึกษาวิทยานิพนธ์: ชีรเกียรติ์ เกิดเจริญ, Ph.D., อติสร เตือนตรานนท์, Ph.D., อนุรัตน์ วิทยุภัฏสรอรรด, Ph.D.

บทคัดย่อ

วิทยานิพนธ์ฉบับนี้ได้จัดเตรียมความรู้และความเข้าใจเชิงลึกในหัวข้อต่างๆ ทางด้านนาโนเทคโนโลยี อาทิเช่น การออกแบบเชิงอะตอมของโครงสร้างวัสดุนาโน, การสังเคราะห์นาโนซิงค์ออกไซด์แบบโครงสร้างต่างๆ, การประดิษฐ์ก๊าซเซนเซอร์ที่มีโครงสร้างแบบนาโน, และการสร้างจมูกอิเล็กทรอนิกส์แบบพกพาได้ สำหรับงานด้านการออกแบบ กลไกกระบวนการเกิดท่อนาโนซิงค์ออกไซด์ไบต์ได้ถูกศึกษาโดยใช้ระเบียบวิธีทางควอนตัมDFTB ผลการทดลองได้แสดงให้เห็นถึงความสำคัญของการเกิดความบกพร่อง (Defects) ที่ผนังของท่อนาโนซิงค์ออกไซด์ไบต์ ท่อนาโนซิงค์ออกไซด์ซอบที่จะสร้างพันธะแบบ sp^2 ระหว่าง ซิงค์ออกไซด์อะตอมและคาร์บอนอะตอม ในงานด้านสังเคราะห์นาโนซิงค์ออกไซด์ ไคอะแกรมรูปร่างต่างๆของนาโนซิงค์ออกไซด์ ที่ปลูกโดยวิธีการระเหยเชิงความร้อนได้ถูกนำเสนอ บทบาทของอุณหภูมิฐานรองรับ และอุณหภูมิของสารตั้งต้นในการเกิดความหลากหลายของรูปร่างของนาโนซิงค์ออกไซด์ และกลไกที่มีผลต่อความแตกต่างของโครงสร้างดังกล่าวได้ถูกให้ความสำคัญ สำหรับงานด้านก๊าซเซนเซอร์ การประดิษฐ์ก๊าซเซนเซอร์แบบโครงสร้างนาโน อาทิเช่น WO_3 , SnO_2 , CNT- WO_3 , CNT- SnO_2 ที่ถูกเตรียมโดยวิธีสังเคราะห์อิเล็กตรอนโดยการใช้สารผสมของผงได้ถูกรายงาน การเจือด้วยท่อนาโนคาร์บอนสามารถเพิ่มคุณสมบัติการตอบสนอง และการเลือกตอบสนองให้กับก๊าซเซนเซอร์แบบโลหะออกไซด์ได้อีกทั้งยังสามารถช่วยลดอุณหภูมิการทำงานได้อีกด้วย ในงานสุดท้าย จมูกอิเล็กทรอนิกส์แบบพกพาได้โดยใช้ประโยชน์จากก๊าซเซนเซอร์แบบลูกผสมและวิธีการดึงข้อมูลแบบใหม่ได้ถูกบรรยาย ผลการทดลองได้แสดงให้เห็นว่า จมูกอิเล็กทรอนิกส์สามารถนำมาใช้ประโยชน์ได้หลากหลายด้าน เช่น สามารถใช้ในการควบคุมคุณภาพอาหาร และเครื่องดื่ม, สามารถใช้ในการป้องกันด้านอากาศ และสามารถใช้ในการระบุตัวบุคคลได้ มันจึงคาดหวังว่า วิทยานิพนธ์ฉบับนี้ จะเป็นประโยชน์ตั้งแต่่างงานวิจัยด้านพื้นฐาน จนถึงการใช้งานได้จริงในระดับอุตสาหกรรม

CONTENTS

	Page
ACKNOWLEDGEMENTS	iii
ABSTRACT (ENGLISH)	iv
ABSTRACT (THAI)	v
LIST OF TABLES	x
LIST OF FIGURES	xi
CHAPTER I INTRODUCTION	1
1.1 Impact of Nanotechnology in Real Life	1
1.1.1 Nanotechnology in Medicine	1
1.1.2 Nanotechnology in Energy Production	2
1.1.3 Nanotechnology in Electronics	2
1.2 Research Objectives	3
1.3 Advantages of this Research	4
1.4 Outline of Thesis	5
CHAPTER II MOLECULAR MODELING	6
2.1 Overview	6
2.2 Basics of Density Functional Theory (DFT)	7
2.2.1 Local Density Approximation	8
2.2.2 Generalized Gradient Approximation	9
2.2.3 Hybrid Functionals	9
2.2.4 Basis sets	10
2.3 Density Functional based Tight Binding (DFTB) method	10
2.3.1 Standard DFTB Model	11
2.3.2 Self-Consistent Charge DFTB (SCC-DFTB)	12
2.3.3 DFTB Molecular Dynamics Simulation	13

CONTENTS (cont.)

	Page
CHAPTER III FORMATION OF SILICON CARBIDE	
NANOTUBES FROM CARBON NANOTUBES	14
3.1 Introduction of Silicon Carbide Nanotubes	14
3.2 Methodology	16
3.3 Results and Discussion	20
3.3.1 Adding of Si Atoms between IWS	22
3.3.2 Shooting of Si Atoms on DWNT Surface	25
3.3.3 Model Final Structure of SiCNT	30
3.4 Conclusion	32
CHAPTER IV SYNTHESIS OF NANOMATERIALS	33
4.1 Top-down and Bottom-up Methods	33
4.2 Vapor–Liquid–Solid & Vapor–Solid Mechanisms	34
CHAPTER V GROWTH OF UNIFORM LARGE-SCALE	
ARRAYS OF ZINC OXIDE NANOSTRUCTURES	36
5.1 Introduction of ZnO Nanostructures	36
5.2 Experimental Details	37
5.3 Temperature Profile of the Two-zone Furnace	38
5.4 Shape Diagram of ZnO Nanostructures as a Function of T_s and T_p	39
5.5 Mechanisms of the ZnO nanostructures	42
5.6 Conclusion	46
CHAPTER VI NANOSTRUCTURE GAS SENSORS	47
6.1 Fundamental Principles of Metal Oxide Gas Sensors	47
6.2 Fabrication of Nanostructure Gas Sensors	48
6.2.1 Thermal Oxidation Technique	48
6.2.2 Electron Beam Evaporation Technique	49
6.3 Au-doped ZnO Nanostructure Gas Sensors	50

CONTENTS (cont.)

	Page
6.3.1 Background	50
6.3.2 Preparation of ZnO and Au-doped ZnO Nanostructure Sensors	51
6.3.3 Sensor Responses on Volatile Organic Compounds	52
6.4 Carbon Nanotube-doped SnO ₂ Gas Sensors	54
6.4.1 Background	54
6.4.2 Fabrication of Gas Sensors	54
6.4.3 Characterization of Gas-sensing Films	57
6.4.4 Sensor Responses	59
6.4.5 Sensing Mechanism of CNT–SnO ₂ Gas Sensors	61
6.5 Conclusion	62
CHAPTER VII HYDROGEN GAS SENSOR	63
7.1 Introduction	63
7.2 Experimental	64
7.2.1 Preparation of Materials	64
7.2.2 Fabrication of MWCNTs-doped WO ₃ Thin Film	65
7.2.3 Measurement of Gas Sensing	66
7.3 Characterization of Thin Films	66
7.4 Sensing Properties of Thin Films	68
7.5 Sensing Mechanism of MWCNTs-doped WO ₃ Thin Film	70
7.6 Conclusion	71
CHAPTER VIII ELECTRONIC NOSE	73
8.1 Introduction of Electronic Nose	73
8.2 Construction of Portable E-nose	74
8.3 Principal Component Analysis	76
8.4 Feature Extraction Techniques	77
8.5 Conclusion	79

CONTENTS (cont.)

	Page
CHAPTER IX REAL WORLD APPLICATION OF E-NOSE	80
9.1 Detection and Discrimination of Volatile Organic Compounds	80
9.2 Detection and Classification of Human Body Odor	82
9.2.1 Background	82
9.2.2 Humidity Control	83
9.2.3 Human Body Odor Collection	85
9.2.4 Evaluation of Sensor Response to Body Odor Strength	85
9.2.5 Correction of Humidity Effects	86
9.2.6 Evaluation of Sensor Response to Body Odor Strength	90
9.2.7 Detection and Classification of Human Body Odor	90
9.3 Detection of Methanol Contamination in Whiskeys	94
9.4 Conclusion	97
CHAPTER X SUMMARY	99
REFERENCES	102
BIOGRAPHY	119

LIST OF TABLES

Table	Page
3.1 Average C-C bond length of optimized structure of the DWNT obtained by DFTB method.	21
3.2 Initial velocities assigned to Si atoms.	26
5.1 Reduction of ZnO with C at different T_p temperatures, forming Zn vapor calculated following Rao	42
9.1 Specifications of each metal oxide sensor.	83
9.2 The concentration of the isovaleric acid levels that correspond to subjective impression by using human nose.	86
9.3 The absolute average percentage change of resistance of each sensor upon varying humidity generated by hardware correction.	90

LIST OF FIGURES

Figure	Page
1.1 Transmission electron microscope images of gold/silica nanoshells during shell growth.	2
1.2 ZnO nanowire nanolasers.	3
2.1 Schematic of multiscale modeling approaches.	6
3.1 (a) HRTEM images of two MWNTs (b) and SWNTs rope: each black circle is the image of one SWNT of the rope	14
3.2 HRTEM images of SiCNTs. The inset shows the EDAX result of the SiCNTs.	16
3.3 Schematic diagram of the synthesis apparatus.	17
3.4 Growth mechanism of the SiCNWs using CNTs as a template.	17
3.5 Geometry of the DWNT (armchair (3,3) in armchair (8,8)).	19
3.6 Optimized structure of armchair (3,3) in armchair (8,8).	20
3.7 (a) MBL and (b) RBD of optimized structure of the DWNT.	21
3.8 Definition of C1–C2 and C2–C3 bonds.	22
3.9 Adding of one Si atom.	22
3.10 Adding of three Si atoms.	23
3.11 MBL and RBD plots of optimized structure of the 3Si-DWNT.	24
3.12 Adding of five Si atoms.	24
3.13 Snapshots of shooting of Si atoms around the DWNT surface at 1500 K, 2000K and 3000K.	25
3.14 Snapshots of shooting of Si atoms around the DWNT surface as a function of time at 1500 K.	26
3.15 Snapshots of shooting of one Si atom at different velocity as a function of time.	27

LIST OF FIGURES (cont.)

Figure	Page
3.16 Snapshots of shooting of Si atoms at high velocity as a function of time.	28
3.17 Snapshots of shooting of Si atoms at different high velocities.	28
3.18 Optimized structure of DWNT with one vacancy defect using DFTB+.	29
3.19 Snapshots of shooting of Si atoms onto defect DWNT.	
3.20 Initial structures of SiCNTs designed from bulk phases of SiC structures.	30
3.21 Optimized structures of SiCNTs (sp^3) based on DFTB+.	31
3.22 Optimized structures of SiCNTs (sp^2) based on DFTB+.	31
3.23 Comparison between experimental result and model SiCNTs.	32
4.1 Photolithography process.	33
4.2 ZnO nanobear.	34
4.3 VLS & VS mechanisms.	35
5.1 (a) Schematic diagram of the thermal CVD growth system. (b) Temperature profile of the two-zone heating furnace. The inset in (b) shows temperature gradient versus temperature of heating 1 with a fixed heating 2 temperature of 950 °C. Heating 1 temperature is measured 12 cm away from the right edge of heating 1 zone (the edge neighboring heating zone 2).	37
5.2 SEM images of ZnO nanowires grown at position II with $T_p=950^\circ\text{C}$ and $T_s=800^\circ\text{C}$. No Au tips are noticed indicating catalyst free VS growth.	39
5.3 Shape diagram of ZnO nanostructures formed at different T_s and T_p which includes: (a) nanowires nuclei (sample A), (b) aligned nanowires (sample B), (c) mostly triangular nanosheets (sample C), (d) nanohammers (sample D), nanospears (sample E), and nanopins	

LIST OF FIGURES (cont.)

Figure	Page
<p>(sample F). Note that pure catalyst free (VS) growth is observed only at B and all others are catalyst assisted (VLS) as deduced from the Au dots at the nanostructures tips. No growth was observed on the bare surface of the samples, i.e. the nucleation was <i>always</i> catalyst assisted.</p>	40
<p>5.4 SEM image of ZnO nanostructures grown using laser ablation at $T_s=820^\circ\text{C}$ (Ar 300 mbar, 30 sccm Ar) having a similar morphology to that of samples A in the shape diagram. The inset TEM image reveals an Au dot at the tip.</p>	41
<p>5.5 ZnO nanowires with decreasing T_s.</p>	44
<p>5.6 ZnO nanostructures grown using laser ablation at $T_s=900^\circ\text{C}$ (70 torr, 50 sccm Ar) having a similar morphology to that of samples C in the shape diagram. (a) SEM image, (b) TEM image revealing an Au dot at the tip, (c) Cross-sectional HRTEM image of the tip indicating that the growth direction dictated by the tip is different than the growth direction ([0001]) of the free side of the triangular sheet. The sheet thus grows by a combination of the VS (catalyst free) and VLS (catalyst assisted) mechanisms.</p>	45
<p>6.1 Model of inter-grain potential barrier in (a) absence and (b) presence of gases.</p>	47
<p>6.2 Typical thermal oxidation furnace.</p>	49
<p>6.3 Typical electron beam vapor deposition.</p>	50
<p>6.4 FESEM images of (a) ZnO and (b) 10 wt% Au-doped ZnO nanostructure.</p>	51
<p>6.5 Produced (a) ZnO and (b) 10 wt% Au-doped ZnO nanostructure sensors.</p>	52
<p>6.6 The sensor response of (a) ZnO and (b) 10 wt% of Au-doped ZnO sensors to concentrations of VOCs.</p>	53

LIST OF FIGURES (cont.)

Figure	Page
6.7 Structure of the gas sensor; (a) top view of interdigitated electrode, (b) cross-sectional view.	54
6.8 Typical TEM images of multi-walled CNT (a) before and (b) after purification.	56
6.9 Photograph of the fabricated sensor.	56
6.10 SEM images of sensing films; (a) undoped SnO ₂ film, (b) 0.5 wt% CNT–SnO ₂ film and (c) 1wt% CNT–SnO ₂ film. The yellow circles in (b) and (c) indicate CNT fragments, (d) typical cross-sectional SEM image of CNT–SnO ₂ film and (e) typical HRTEM image of CNT–SnO ₂ film.	57
6.11 Sensor responses of undoped SnO ₂ sensor, 0.5 wt% CNT–SnO ₂ sensor and 1 wt% CNT–SnO ₂ sensor to different concentrations of (a) EtOH and (b) MeOH.	60
7.1 SEM images of the produced MWCNTs grown by the CVD process.	64
7.2 High resolution TEM image of the produced MWCNT grown by the CVD process.	65
7.3 SEM image of MWCNT-doped WO ₃ thin films on alumina substrate.	67
7.4 (a) High-resolution TEM image and (b) corresponding selected area diffraction pattern of MWCNT-doped WO ₃ thin film.	67
7.5 Sensing response to H ₂ (1,000 ppm) at different operating temperatures.	68
7.6 Sensing response of the undoped WO ₃ and MWCNT-doped WO ₃ thin films to high H ₂ concentrations (5,000–50,000 ppm) at the operating temperature of 250 °C.	69
7.7 Sensing response of MWCNT-doped WO ₃ thin film at the operating temperature of 350 °C to various concentrations of different gas vapors.	70

LIST OF FIGURES (cont.)

Figure	Page
8.1 Comparison between Mammalian Nose and E-nose.	73
8.2 Schematic diagram of the portable E-nose system.	74
8.3 Radially symmetric sensor chamber	75
8.4 Typical raw data from a sensor and the max/min feature extraction on each curve.	77 78
8.5 Correction method of baseline shift as time proceeds.	
9.1 Results of PCA for discriminate of (a) alcohols and (b) typical Thai wines.	81 84
9.2 Schematic diagram of humidity control using hardware-based method.	88
9.3 Resistance of sensors (a) TGS 813, (b) TGS 825 and (c) TGS 2602 versus relative humidity.	
9.4 (a) Sensor response to isovaleric acid at different intensity level. (b) Logarithmic plot of the sensor response.	91
9.5 The sensor response with error bar of (a) person A and (b) person B in the morning and the afternoon. L and R denote the left and right armpits, respectively.	92
9.6 The 2D-PCA of armpit odors from two persons as measured in the afternoon during 5 days.	94
9.7 (a) Raw responses (b) primary derivative and integral signals of gas sensors measured using portable E-nose.	95
9.8 PCA results using feature extraction from (a) ΔR , (b) $\Delta R/R_0$ and (c) integral and (d) primary derivative.	96

CHAPTER I

INTRODUCTION

1.1 Impact of Nanotechnology in Real Life

The first introduction to nanotechnology took place in 1959 by Prof. Richard Feynman who was awarded the 1965 Nobel Prize in Physics on quantum electrodynamics. He gave a lecture at the annual meeting of the American Physical Society in Caltech, California, on December 2, 1959 with the topic entitled “There’s Plenty of Room at the Bottom”. His talk generates the idea of a process for manipulating individual atoms and molecules that do not deny the principle of physics [1]. Up to now, more than 40 years later, nanotechnology becomes a multi-billion dollar research field that crosses many areas of research and development.

Nanotechnology can create many new materials and devices with a vast range of applications, such as in medicine, energy production, and electronics.

1.1.1 Nanotechnology in Medicine

Nanomedicine has been defined as “the monitoring, repair, construction, and control of human biological systems at the molecular level, using engineered nanodevices and nanostructures” [2,3]. Therefore, nanotechnology in medicine is the application of nanoscale technologies to the practice of medicine. It has been used for the diagnosis, prevention, and treatment of disease and to gain an increased understanding of complex underlying disease mechanisms. For example, C. Loo and his co-workers [4] demonstrated the potential of nanoshells in cancer imaging and therapy. They synthesized gold/silica nanoshells (see Fig. 1) via chemical reduction in solution and described several examples of nanoshell-based diagnostic and therapeutic approaches including the development of nanoshell bioconjugates for molecular imaging, the use of scattering nanoshells as contrast agents for optical coherence tomography (OCT), and the use of absorbing nanoshells in NIR thermal therapy of tumors.

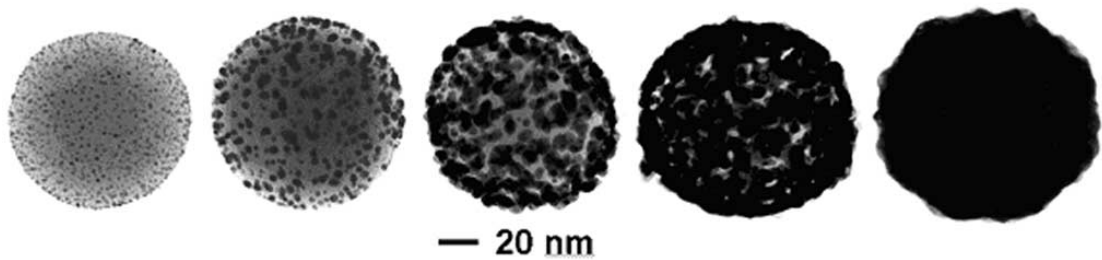


Figure 1.1: Transmission electron microscope images of gold/silica nanoshells during shell growth. (Fig. from *Tech. Canc. Res. Treat.* 3 (2004) pp. 35)

1.1.2 Nanotechnology in Energy Production

The most advanced nanotechnology related to energy production is: storage, conversion, manufacturing improvements by reducing materials and process rates, energy saving and enhanced renewable energy sources. For example, J. Rafiee, a doctoral student in the Department of Mechanical, Aerospace, and Nuclear Engineering at Rensselaer Polytechnic Institute, has developed a new method of ultra-efficient hydrogen storage based on graphene. He employed a combination of mechanical grinding, plasma treatment, and annealing to engineer the atomic structure of graphene to maximize its hydrogen storage capacity. His new material is able to store hydrogen with 14 percent efficiency, which is much better than any other material made so far. This will be useful in the development of practical hydrogen fueled cars.

1.1.3 Nanotechnology in Electronics

The field of electronics including optoelectronics and photonics has been benefiting from the ability to synthesize semiconducting nanowires and quantum dots. Advances in light-emitting diodes, photodetectors, nanolasers, solar cells, and field emission devices have been focused from many research groups. The future of these devices depends on their ability to control the size, orientation and properties of one- and zero-dimensional materials [5] that enable to improve display screens on electronics devices, reduce power consumption while decreasing the weight and thickness of the screens, increase the density of memory chips and so on. For an example, Prof. Peidong Yang and co-workers [6] reported the growth of high-quality, uniform ZnO nanowire arrays by combining a typical vapor-phase nanowire growth

process with another common thin-film growth technique: epitaxy. The resulting nanowires have a perfect hexagonal cylindrical shape with atomically smooth side and end facets as shown in Fig. 2. They used the 4th harmonic output of a Nd:YAG laser (266 nm) as the excitation source and have clearly demonstrated that these highly oriented ZnO nanowire arrays indeed serve as an excellent nanoscopic laser cavity with a lasing wavelength of 380 nm.

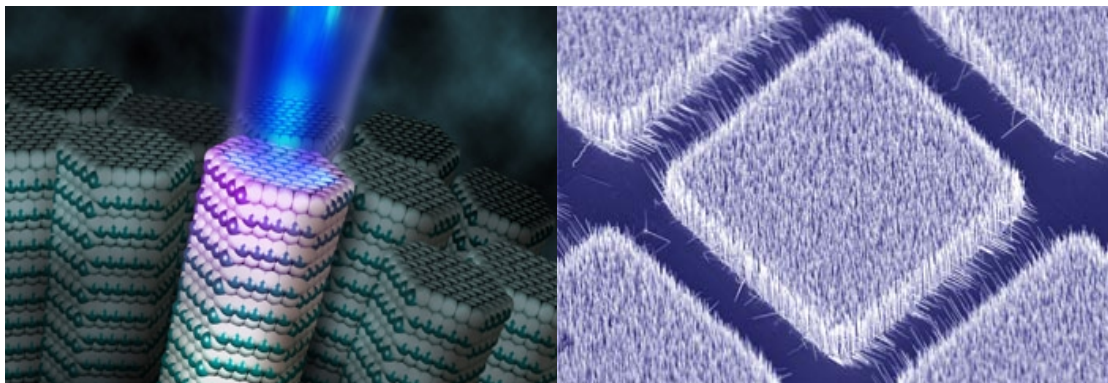


Figure 1.2: ZnO nanowire nanolasers.

(Fig. from http://www.nsf.gov/news/news_images.jsp?cntn_id=108987&org=NSF)

From points of view above, nanotechnology plays an important role for advanced technology in the 21st Century. Understanding of nanomaterial at the atomic and molecular level, finding of new nanomaterial, and providing of effective methods for nanodevice fabrication are necessary in order to use nanotechnology for improving the world in which we live. In this thesis, the use of nanotechnology in field of electronics has been demonstrated. The thesis covers the topics of nanotechnology ranging from molecular modeling, synthesis of nanomaterial, fabrication of nanodevice such as gas sensors to the real world application.

1.2 Research Objectives

- To design nanomaterial such as silicon carbide nanotubes (SiC nanotube) and study the their formations using molecular modeling based on Density Functional based Tight Binding (DFTB) method.

- To synthesize nanomaterial such as ZnO structures and study their mechanisms.
- To fabricate nanostructure gas sensor such as WO₃, SnO₂, ZnO, Au-doped ZnO, CNT-doped WO₃, CNT doped SnO₂ gas sensors.
- To construct portable electronics nose (E-nose) based on nanostructure gas sensors.
- To demonstrate the real world application of the portable E-nose.

1.3 Advantages of this Research

It provides large knowledge and deep understanding of various topics of nanotechnology. For examples, (I) this thesis has demonstrated how to model the interested nanostructure correlated with experimental work. It will be useful for modeling new nanomaterial that does not have a crystal structure before. (II) This thesis has prepared a method to optimize a thermal chemical vapor deposition system that allows a simple fabrication of these various nanoproducs, especially ZnO nanostructure. The way to synthesize the large scale homogenous ZnO nanostructures and the first shape diagram which relates the different ZnO nanostructures to source powder temperature and substrate temperature has been presented. Not only on ZnO nanostructure but also it will be very useful for producing various nanomaterials in large scale area. (III) This thesis has reported how to fabricate nanostructure gas sensor, especially CNTs–metal oxides gas sensors, by using electron beam (E-beam) evaporation process that is one of very useful methods because the E-beam offers extensive possibilities for controlling film structure and morphology with desired properties such as dense coating, high thermal efficiency, low contamination, high reliability and high productivity. However, there have been very few reports on CNTs–metal oxides gas sensors prepared by this technique because co-evaporation of CNTs/ metal oxides is a relatively new concept and, at glance, it seems to be fundamentally impossible. (IV) This thesis has presented how to construct portable electronics nose (E-nose) based on nanostructure gas sensors which is inexpensive, fast, portable, reliable and suitable for use for the detection and classification of both solid and liquid samples. The new feature extraction techniques including integral and primary derivative has been proposed for improving classification performance.

Moreover, this thesis has shown how to apply E-nose based on nanostructure gas sensors in a real-world application, i.e., for detecting methanol (MeOH) contaminant in whiskeys that will be a useful tool for quality assurance of whiskey produced by village industries, or for detecting and discriminating of human body odor that will open the door to the field of human body odor biometrics.

1.4 Outline of Thesis

Overview of this thesis is described in chapter 1. The theory of quantum mechanics including DFTB method, Self-consistent charge DFTB method and DFTB molecular dynamics simulation is given in chapter 2. An example for using DFTB to study SiC formation is shown in chapter 3. For chapter 4, reader can review the main methods including Top-down and Bottom-up methods for synthesis nanomaterials. The detail and procedures of growth of uniform ZnO nanostructures are explained in chepter 5. Fundamental principles and fabrications of metal oxide gas sensors using thermal oxidation and E-beam evaporation techniques are systematically introduced in chapter 6. Development of effective H₂ gas sensors for monitoring of H₂ leaks is presented in chapter 7. Construction of portable E-nose and its real world application are explicitly elucidated in chapter 8 and chapter 9, respectively. Finally, summary of new finding for this thesis will be concluded in chapter 10.

CHAPTER II

MOLECULAR MODELING

2.1 Overview

Molecular modeling encompasses all theoretical methods and computational techniques used to model or mimic the behavior of molecules [7]. It can be used in two important ways [8]. One particularly way is to model a molecular system prior to synthesizing that molecule in the laboratory. This is very useful information because synthesis of single compound could require months of labor and it may generate toxic waste. Another use of the molecular modeling is to understand a problem more completely. There are some properties of a molecule that can be obtained computationally more easily than by experimental such as molecular bonding, band structure, charge transfer, etc. Therefore, molecular modeling is very important work for research in nano scale. However, there are many techniques that are each appropriate at a given scale and have a corresponding capability in terms of number of atoms handled or simulation time as shown in Fig. 2.1.

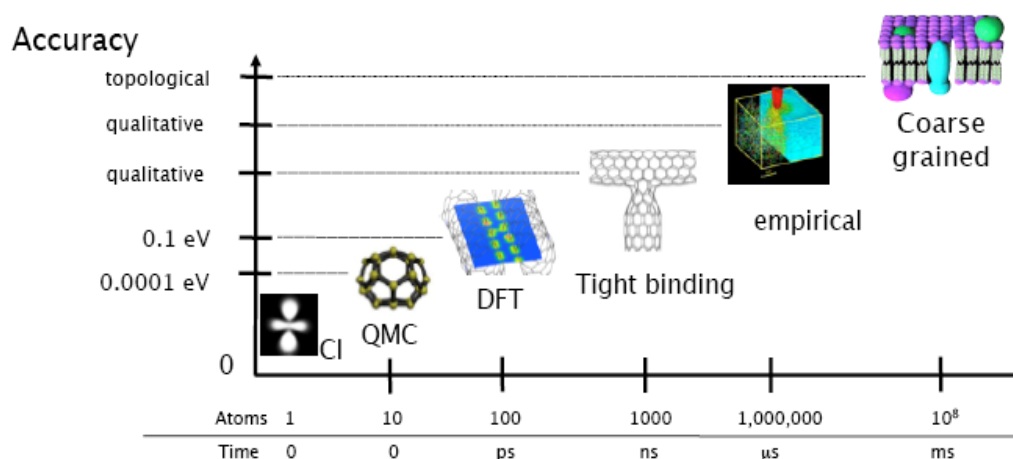


Figure 2.1: Schematic of multiscale modeling approaches.

(Fig. from <https://camtools.cam.ac.uk/access/wiki/site/5b59f819-0806-4a4d-0046-bcad6b9ac70f/research.html>)

From Fig. 2.1, the highest accuracy is achieved by the so-called “first principle methods” such as post-Hartree-Fock (Configuration Interaction (CI)), and quantum monte carlo (QMC) including properly both electronic exchange and correlation within a many-body treatment [9]. However, these calculations can only address the systems with up to 20 to 30 atoms or slightly more. In larger system including 100 to 200 independent atoms, density-functional theory (DFT) gives accurate solutions. However, DFT still becomes computationally very demanding for larger structures. Nowadays, quantum mechanics (QM) based on tight binding (TB) methods are becoming more and more popular, especially for nanoscale-sized materials including several hundreds or thousands of atoms. In this thesis, the QM based on TB methods such as density functional based tight binding (DFTB) method has been employed in model and in calculation of a nanomaterial. The basic principles of DFT and DFTB have been exhibited in this chapter. The apparent equations and theories have been reviewed from published paper, lecture notes and books [8-18].

2.2 Basics of Density Functional Theory (DFT)

A density functional theory (DFT) determines the energy of a molecule from the electron density instead of a wave function. The advantage of using electron density is that the integrals for Coulomb repulsion need be done only over the electron density, which is a three-dimensional function, thus scaling as N^3 . Therefore, the results from DFT calculation will take the faster calculations than Hartree-Fock (HF) calculations (which scale as N^4). Moreover, DFT can be included electron correlation in calculation that makes it a bit more accuracy. In addition, the better DFT functionals can give results with an accuracy similar to that of an MP_2 calculation [8].

A unique functional of a charge density ($\rho(r)$) can be represented using the Kohn-Sham eigenstates (Ψ_i):

$$\rho(r) = \sum_i^M |\Psi_i(r)|^2 \quad (2.1)$$

Where M is non-interacting electrons.

The total energy of a system of M electrons in the field of N nuclei at positions (\vec{R}) may be written as:

$$E = \sum_i^M n_i \left\langle \Psi_i \left| -\frac{\nabla^2}{2} + V_{ext} + \frac{1}{2} \int \frac{\rho(\vec{r}')}{|\vec{r} - \vec{r}'|} \Psi_i \right\rangle + E_{XC}[\rho(\vec{r})] + \frac{1}{2} \sum_{\alpha, \beta}^N \frac{Z_\alpha Z_\beta}{|\vec{R}_\alpha - \vec{R}_\beta|} \quad (2.2)$$

$$E = E_T + E_{ext} + E_H + E_{XC} + E_{II} \quad (2.3)$$

Where E_T is the kinetic energy, E_{ext} is the external interaction (including electron-ion interactions), E_H is Hartree energy, E_{XC} is the exchange-correlation energy, hiding all the difficult many-body effects, and E_{II} ion-ion interaction energy. In addition, the quality of DFT methods is completely dependent on the quality of the functionals for the E_{XC} [10].

$$E_{XC} = \int \rho(r) \varepsilon_{XC}[\rho(r)] dr \quad (2.4)$$

2.2.1 Local Density Approximation

The energy density (ε_{xc}) is always treated as a sum of individual exchange and correlation contributions. The simplest functionals (E_{XC}) depend on the density only, $E_{XC}(\rho)$. They can be described using the simple Slater function as called local density approximation (LDA). The LDA can perform quite well for geometries and vibrational frequencies. The exchange energy (E_x) for LDA can be written as;

$$E_x[\rho(r)] = -\frac{9\alpha}{8} \left(\frac{3}{\pi} \right)^{1/3} \int \rho^{4/3}(r) dr \quad (2.5)$$

Within Slater's derivation, the value for the constant α is 1. For the uniform electron gas, α is $\frac{2}{3}$. For empirical analysis, α should be $\frac{3}{4}$ that provides more accurate results than either $\alpha = 1$ or $\alpha = \frac{2}{3}$.

From Eq. (2.5), the energy density is:

$$\varepsilon_x[\rho(r)] = -\frac{9\alpha}{8} \left(\frac{3}{\pi} \right)^{1/3} \rho^{1/3}(r) \quad (2.6)$$

However, the LDA can be extended to the spin-polarized regime using

$$\varepsilon_x[\rho(r), \xi] = \varepsilon_x^0[\rho(r)] + \{\varepsilon_x^1[\rho(r)] - \varepsilon_x^0[\rho(r)]\} \left[\frac{(1 + \xi)^{4/3} + (1 - \xi)^{4/3} - 2}{2(2^{1/3} - 1)} \right] \quad (2.7)$$

$$\text{Where} \quad \xi(r) = \frac{\rho^\alpha(r) - \rho^\beta(r)}{\rho(r)} \quad (2.8)$$

Where ξ is the normalized spin polarization. α and β are spin density. ε_x^0 is given by Eq. (2.6) with the appropriate value of α (the empirical constant). ε_x^1 is the analogous expression derived from consideration of a uniform electron gas. For unpolarized system, $\xi=0$, the Eq. (2.7) will become to Eq. (2.6). For systems including spin polarization (e.g., open-shell systems), it must be used the spin-polarized formalism as shown in Eq. (2.7) called as local spin density approximation (LSDA).

2.2.2 Generalized Gradient Approximation

Even though LDA can perform quite well for geometries and vibrational frequencies, it is not very good for energies because the correlation functional depend not only on the local value of the density but also on the extent to which the density is locally changing. One obvious way to improve the correlation functional is to calculate both the density and the gradient of the density defined as generalized gradient approximation (GGA). The energy density for GGA can be written as:

$$\varepsilon_x^{GGA}[\rho(r)] = \varepsilon_x^{LSDA}[\rho(r)] + \Delta\varepsilon_x \left[\frac{|\nabla\rho(r)|}{\rho^{4/3}(r)} \right] \quad (2.9)$$

These are functionals of density and density gradient and give quite reasonable energies.

2.2.3 Hybrid Functionals

Attempts, to substitute ε_x^0 by HF exchange are not successful, but a partial mixing led to very powerful functionals, e.g. in famous B3LYP functional, which has a 20% HF content. The success is due an error cancellation, e.g. DFT underestimates reaction barriers, HF overestimates them. Therefore, the combination is about right. This can be defined as hybrid functionals. The E_{XC} for the hybrid functionals can be written a:

$$E_{XC} = (1 - a)E_{XC}^{GGA} + aE_X^{HF} \quad (2.10)$$

In case of famous B3LYP functional, $a=0.2$. the full E_{XC} B3LYP model is defined by:

$$E_{XC}^{B3LYP} = (1 - a)E_X^{LSDA} + aE_X^{HF} + b\Delta E_X^B + (1 - c)E_C^{LSDA} + cE_C^{LYP} \quad (2.11)$$

Where a , b , and c were optimized to 0.20, 0.72, and 0.81, respectively.

2.2.4 Basis Sets

A basis set is a set of functions used to create the molecular orbitals. The most common minimal basis set is Slater-type orbitals (STO-3G), in which three primitive Gaussian-type-orbitals (GTO) functions are combined into one contracted Gaussian function (CGF). The basis function (η) of a typical STO is expressed as:

$$\eta_{STO}(\zeta, n, l, m; r, \theta, \phi) = Nr^{n-1}e^{-\zeta r}Y_{lm}(\theta, \phi) \quad (2.12)$$

Where N is a normalization constant. ζ is the Slater exponent. The r , θ , and ϕ are spherical coordinates and Y_{lm} is the angular momentum part. The n , l , and m are quantum numbers: principal, angular momentum and magnetic, respectively. The GTO of the general form can be written as:

$$\eta_{GTO} = Nx^l y^m z^n e^{-\alpha r^2} \quad (2.13)$$

Where α represents the orbital exponent which determines how compact (large α) or diffuse (small α) the resulting function is. One CGF is in a form:

$$\eta_{CGF} = \sum_a^{All} d_a \eta_{GTO} \quad (2.14)$$

The relationship of charge density and basis set can be written as:

$$n(r) = \sum_i^M |\Psi_i(r)|^2 = \sum_i^M \sum_{\mu}^L \sum_{\nu}^L c_{\mu i} c_{\nu i} \eta_{\mu}(r) \eta_{\nu}(r) \quad (2.15)$$

The summation of expansion coefficients ($c_{\mu} c_{\nu}$) can be defined as density matrix (P).

2.3 Density Functional Based Tight Binding (DFTB) Method

Even though DFT methods have been successfully applied for systems of increasing complexity, methods that can include approximations to reduce even more

the computational demand without compromising the reliability of results are still required [13]. Recently, the density functional based tight binding (DFTB) have become one of the best choice in quantum chemical calculations for a broad range of problems and fields in chemistry, physics, materials science, and biochemistry [14].

2.3.1 Standard DFTB Model

DFTB is an approximate method based on the density functional framework. The DFTB can be useful in many ways. For examples, it can be used in calculations of large systems while DFT always limits system sizes or systems are limited for optimization in DFT but they can be used for extensive studies on dynamical properties in DFTB [15]. For a DFTB method, the charge density (ρ) can be written as:

$$\rho(\vec{r}) = \rho_0(\vec{r}) + \delta\rho(\vec{r}) \quad (2.16)$$

Where ρ_0 and $\delta\rho$ are a reference density and a small fluctuation, respectively. Substitution of Eq. 2.16 into Eq. 2.2 and expansion of E_{xc} in a Taylor series up to the second-order term result in:

$$\begin{aligned} E = \sum_i^M n_i \left\langle \Psi_i \left| -\frac{\nabla^2}{2} + V_{ext} + \int \frac{\rho_0'}{|\vec{r}-\vec{r}'|} d\vec{r}' + V_{xc}[\rho_0] \right| \Psi_i \right\rangle - \frac{1}{2} \iint \frac{\rho_0' \rho_0}{|\vec{r}-\vec{r}'|} d\vec{r} d\vec{r}' \\ + E_{xc}[\rho_0] - \int v_{xc}[\rho_0] \rho_0 d\vec{r} + E_{nucl} + \frac{1}{2} \iint \left(\frac{\delta\rho\delta\rho'}{|\vec{r}-\vec{r}'|} + \frac{\delta^2 E_{xc}}{\delta\rho\delta\rho'} \Big|_{\rho_0} \right) d\vec{r} d\vec{r}' \quad (2.17) \end{aligned}$$

Note that expansion of E_{xc} defines a term of $\left(\frac{\delta E_{xc}}{\delta\rho} \right)_{\rho_0} = V_{xc}[\rho_0]$

The Eq. 2.17 can be rewritten as:

$$E = \sum_i^M n_i \left\langle \Psi_i \left| \hat{H}^0 \right| \Psi_i \right\rangle + E_{rep}[\rho_0] + E_{2nd}[\delta\rho, \rho_0] \quad (2.18)$$

$$\text{Where } \hat{H}^0 = -\frac{\nabla^2}{2} + v_{ext}(\vec{r}) + \int \frac{\rho_0'}{|\vec{r}-\vec{r}'|} d\vec{r}' + v_{xc}[\rho_0] \quad (2.19)$$

$$E_{rep}[\rho_0] = -\frac{1}{2} \iint \frac{\rho_0' \rho_0}{|\vec{r} - \vec{r}'|} d\vec{r} d\vec{r}' + E_{xc}[\rho_0] - \int v_{xc}[\rho_0] \rho_0 d\vec{r} + E_{nucl} \quad (2.20)$$

$$E_{2nd}[\rho_0, \delta\rho] = \frac{1}{2} \iint \left(\frac{\delta\rho \delta\rho'}{|\vec{r} - \vec{r}'|} + \frac{\delta^2 E_{xc}}{\delta\rho \delta\rho'} \Big|_{\rho_0} \right) d\vec{r} d\vec{r}' \quad (2.21)$$

From Eq. 2.19, 2.20, and 2.21, H^0 is a reference Hamiltonian depending only upon charge density. E_{rep} is the repulsive contribution and E_{2nd} relates to the fluctuations in the charge density. In the standard DFTB scheme, the second-order correction term (E_{2nd} of equation 2.18) is neglected. Therefore, the calculation of the total energy does not depend on the charge density fluctuations and it does not have to be solved iteratively [13]. In summary, the DFTB method is derived from:

$$E_{DFTB} = \sum_i^{Valence\ orbitals} n_i \varepsilon_i + \frac{1}{2} \sum_{A \neq B}^{atoms} E_{rep}^{AB} \quad (2.22)$$

The first term of Eq. 2.22 can be obtained by diagonalization of the Hamiltonian matrix. In DFTB, the Kohn-Sham orbitals are expanded within the linear combination of atomic orbitals (LCAO) approximation using minimal localized pseudoatomic Slater orbitals, which include the confinement harmonic potential $(r/r_0)^2$ for the orbital localization. The r_0 is called as wave function confinement radius [16].

2.3.2 Self-Consistent Charge DFTB (SCC-DFTB)

In SCC-DFTB, the charge density is corrected through inclusion of the second-order contributions E_{2nd} in Eq. 2.18, which are neglected in standard DFTB. The total energies, forces, and transferability in the presence of considerable long-range Coulomb interactions have been improved in SCC-DFTB. In SCC-DFTB, the effects of charge transfer are included but changes in the shape of the charge density are neglected. Therefore E_{2nd} in 2.21 becomes:

$$E_{2nd} \approx \frac{1}{2} \sum_{\alpha, \beta}^N \Delta q_\alpha \Delta q_\beta \iint \left(\frac{1}{|\vec{r} - \vec{r}'|} + \frac{\delta^2 E_{xc}}{\delta\rho \delta\rho'} \Big|_{\rho_0} \right) F_{00}^\alpha F_{00}^\beta Y_{00}^2 d\vec{r} d\vec{r}' \quad (2.23)$$

Where Δq is the Mulliken charge. F_{00} denotes the normalized radial dependence of the density fluctuation in atom and Y_{00} is spherical angular function.

The Eq. 2.23 can be analytically solved by using the very large interatomic separation ($|\vec{r} - \vec{r}'| \rightarrow \infty$) or the interatomic distance tends to zero ($|\vec{r} - \vec{r}'| \rightarrow 0$). The details can be seen from Ref. [13,17]. Summary, the total energy within SCC-DFTB can be written as:

$$E_{SCC-DFTB} = \sum_i^M n_i \left\langle \Psi_i \left| \hat{H}^0 \right| \Psi_i \right\rangle + E_{rep}[\rho_0] + \frac{1}{2} \sum_{\alpha, \beta}^N \Delta q_\alpha \Delta q_\beta \iint \left(\frac{1}{|\vec{r} - \vec{r}'|} + \left. \frac{\delta^2 E_{xc}}{\delta \rho \delta \rho'} \right|_{\rho_0} \right) F_{00}^\alpha F_{00}^\beta Y_{00}^2 d\vec{r} d\vec{r}' \quad (2.24)$$

2.3.3 DFTB Molecular Dynamics Simulation

In classical model, molecular dynamics (MD) simulation is based on molecular mechanics. The MD simulation solves the differential equation in the Newton's equations of motion. The Newton's equations of motion for a system of N interacting atoms can be written as

$$m_i \frac{d^2 r_i}{dt^2} = F_i, i = 1, 2, \dots, N. \quad (2.25)$$

The forces can be rewritten in form of a potential function $V(r_1, r_2, \dots, r_N)$,

$$F_i = -\nabla_{r_i} V(r_1, r_2, \dots, r_N). \quad (2.26)$$

The equations are solved in small time steps using a finite difference method. The finite difference method is used to generate molecular dynamics trajectory that collects the coordinates as a function of time. For algorithms of the finite difference methods, the Verlet algorithm is widely used for integrating the equations of motion in a MD simulation. For DFTB-MD Simulation, a simple analytic expression for the atomic forces can be written as:

$$\bar{F}_\alpha = -\sum_i^M n_i \sum_{\mu, \nu}^N C_{i\mu} C_\nu \left[\frac{\partial H_{\mu\nu}^0}{\partial R_\alpha} - \left(\varepsilon_i - \frac{H_{\mu\nu}^1}{S_{\mu\nu}} \right) \frac{\partial S_{\mu\nu}}{\partial R_\alpha} \right] - \Delta q_\alpha \sum_\xi^N \frac{\partial \gamma_{\alpha\beta}}{\partial R_\alpha} \Delta q_\xi - \frac{\partial E_{rep}}{\partial R_\alpha} \quad (2.27)$$

The Eq. 2.26 is taken from the derivative of the final TB energy with respect to the nuclear coordinates. The detail of calculation can be seen from Ref. [18].

CHAPTER III

FORMATION OF SILICON CARBIDE NANOTUBES FROM CARBON NANOTUBES

3.1 Introduction of Silicon Carbide Nanotubes

Carbon nanotubes (CNTs) having nanoscale dimension (1-D) have been well-known over the past 19 years. The molecules were first discovered by Iijima in 1991 [19] when he was studying the synthesis of fullerenes by using electric arc discharge technique. The high resolution transmission electron microscopy (HRTEM) was employed for observation of that phenomenon. Carbon nanotubes that Iijima observed were so called multi-walled carbon nanotubes (MWNTs) as shown in Fig. 3.1a, nested as Russian dolls, containing at least two graphitic layers, and generally have inner diameters of around 4 nm.

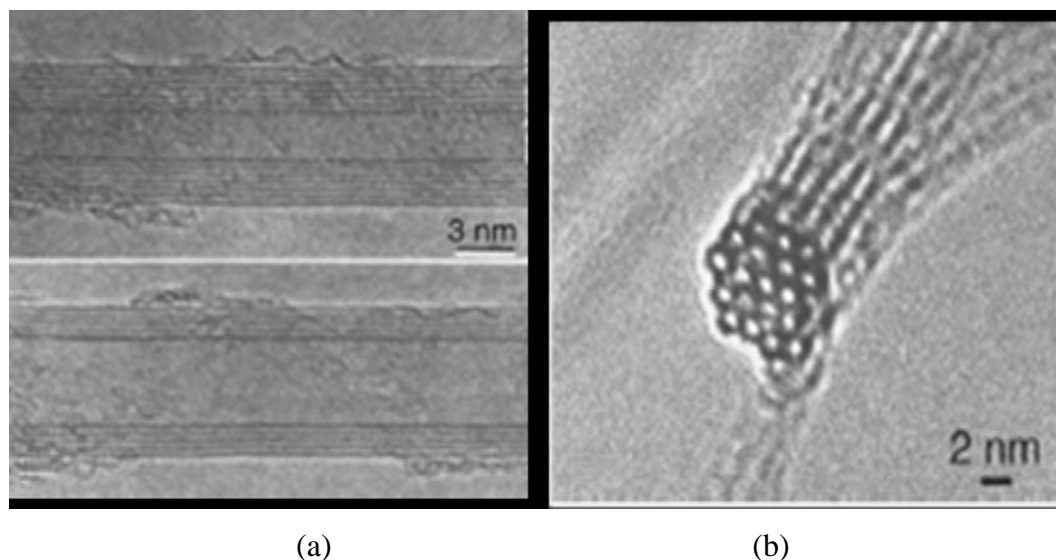


Figure 3.1: (a) HRTEM images of two MWNTs (b) and SWNTs rope: each black circle is the image of one SWNT of the rope (Fig. from Physique 4 (2003) P. 968).

Two years later, Iijima and Ichihashi of NEC [20] and Bethune and colleagues of the IBM Almaden Research Center in California [21] synthesized single-walled carbon nanotubes (SWNTs) as shown in Fig. 3.1b. The SWNTs were synthesized by the same route of producing MWNTs but adding some metal particles to the carbon electrodes. The appearance of SWNT is quite different to that of MWNT. The individual tubes have very small diameters (typically $\sim 1\text{nm}$), and are curled and looped rather than straight. In the early 1990s, two research groups predicted electronic properties of individual SWNTs [22-24]. From their calculations, they found that SWNTs can be either metallic or semiconducting depending on their chirality and diameter. By the end of that decade, these particular predictions were confirmed by experiments [25-26]. In the meantime, a lot of reviews which provide a comprehensive overview with respect to the synthesis, characterization, applications, and the basic mechanical and electronic properties of CNTs have appeared [27–30].

Recently, silicon carbide nanotubes (SiCNTs) have attracted much attention because they offer some advantages over CNTs. For example, SiCNTs exhibit high melting temperature [31] and excellent oxidation resistance at high temperature [32]. Moreover, SiCNTs have a better capacity of hydrogen storage in comparison with CNTs [33]. The first synthesis of SiCNTs was reported by Pham-Huu and his co-workers in 2001 [34]. The method used as called shape memory synthesis is based on the gas–solid reaction between a vapor of SiO and carbon nanofibers for the small diameters, and CNTs for the big diameters. Figure 3.2 shows HRTEM images of open-end SiCNTs from carbon nanofibers.

Up to now, synthesis of SiCNTs can be generally summarized into three classifies: shape memory synthesis [34-38] hydrothermal method [39], and core–shell structural method [40,41]. The shape memory synthesis and hydrothermal method depend on a high temperature (1200–1250 °C) or a high pressure (8 MPa) that are more difficult and contingent for control. For the core–shell structural method, it is an easy and controllable approach for the synthesis of tubular nanostructures. However, the removable core materials reported before were only ZnS and ZnO, both of which should be etched away using the HCl solution during the formation of the SiCNTs. Those samples usually have low purity with trace of residual core materials [42]. Therefore, deep understanding of formation mechanism is necessary for growing a

perfect SiCNTs. In this chapter, the formation mechanism of SiCNTs from CNTs under addition of Si has been investigated using quantum chemical molecular dynamics simulation based on DFTB.

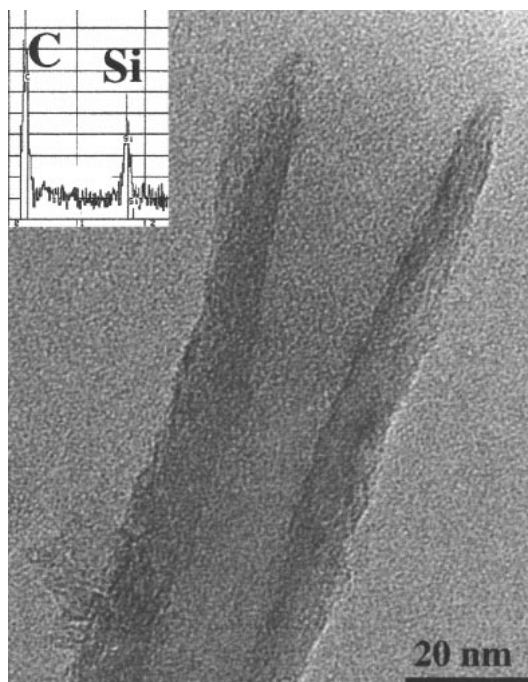


Figure 3.2: HRTEM images of SiCNTs. The inset shows the EDAX result of the SiCNTs. (Fig. from *J. Catal.* 200 (2001) P. 409)

3.2 Methodology

In real experiment, the formation of SiCNTs from CNTs refers to shape memory method [34-38]. Schematic diagram of apparatus for the SiCNTs growth is shown in Fig. 3.3. The SiO powder was placed in the center of a tube furnace (position A). The CNTs grown on silicon substrate were placed at positions B. First, the tube was evacuated to a base pressure of 10^{-2} Torr. Then, the carrier gas of argon mixed with 5% H_2 was introduced at one end of the tube flowing at 50 sccm. The pressure was kept at 500 Torr. The temperature of the furnace was increased to 1250 °C and kept at this temperature for 40 min. The temperature at the substrate position B is ~ 935 °C.

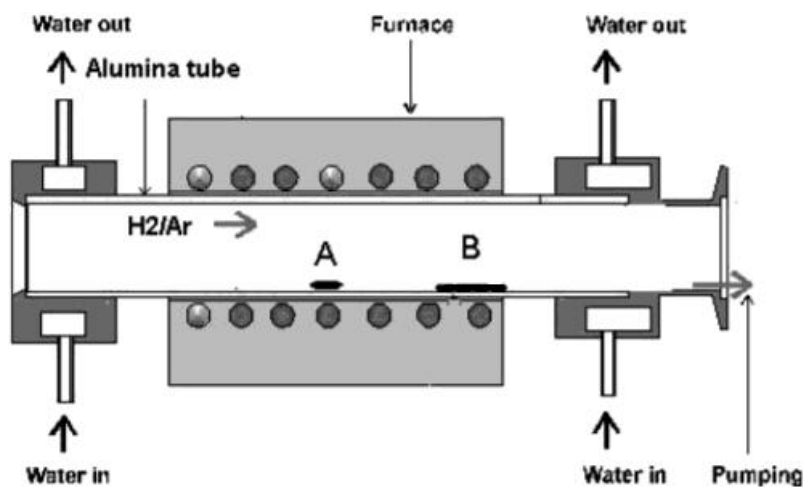


Figure 3.3: Schematic diagram of the synthesis apparatus.

(Fig. from J. Am. Chem. Soc. 124 (2002) P. 14465)

The model of growth mechanism of the SiCNTs using CNTs as a template can be considered as similar with SiC nanowires (see Fig. 3.4).

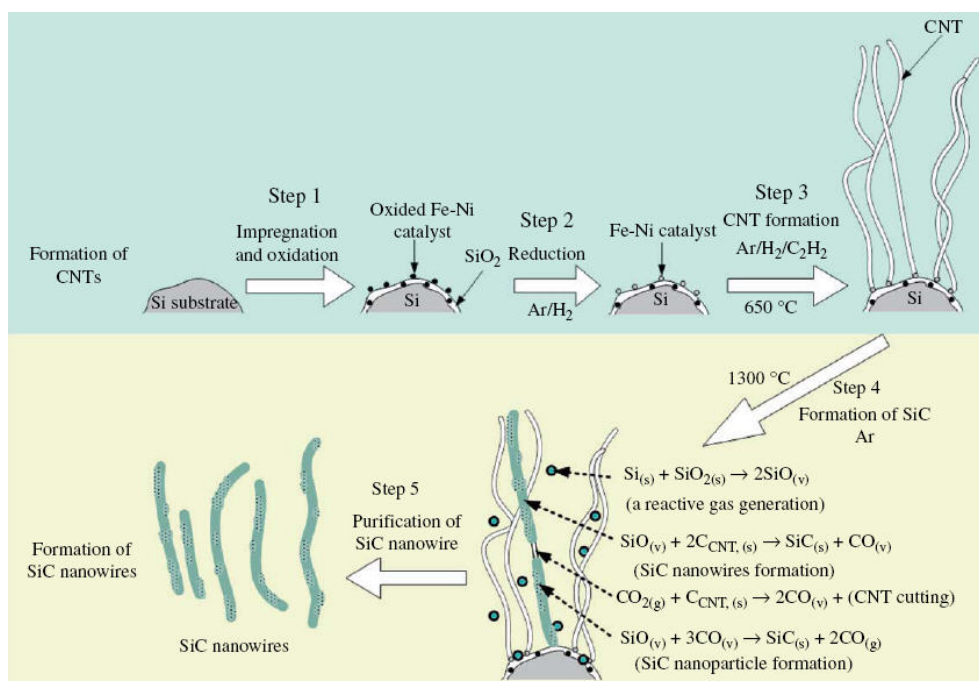


Figure 3.4: Growth mechanism of the SiCNWs using CNTs as a template.

(Fig. from J. Cryst. Growth 311 (2009) P. 1040)

In calculations, the structure and stability of SiCNTs were investigated using ab initio density functional theory [43-45]. In details, it was found that the SiCNTs with alternating Si–C bonds are more stable than the forms which contain C–C or Si–Si bonds. While CNTs have been found to be either metallic or semiconducting depending on their chirality, these calculations showed that SiCNTs are always semiconductors, with direct gaps for zigzag tubes and indirect gaps for armchair and chiral tubes. CNTs and SiCNTs differ in the type of chemical bonding. As a consequence, SiCNTs are polar materials due to electronegativity of the carbon atom with respect to the silicon atom in the SiCNTs. In addition, SiCNTs was found that they will lose stability when the ratio of Si over C increases. But they remain stable until the ratio reaches 50:50, and after that the Si-rich tubes collapse to nanowires or clusters with solid interiors [46].

In simulations or theoretical calculations, the most of the researches on SiCNTs have only been focused on single-walled SiCNTs (SWSiCNTs). However, up to now, no report is available on synthesis of the SWSiCNTs. The current calculated SWSiCNTs may be far away from the real experiments. The modeling of SiCNTs according to the experimental results is still necessary. In this work, double-walled CNTs (DWNTs) as the smallest possible units that can create a C-Si-C 3-layered structure (sp^3) with tetravalent Si will be employed as template of SiCNT growth. SiCNTs will be proved that their structures prefer to form sp^2 or sp^3 hybridization. The selection of starting DWNT structure for template is based on the previous studies by Lair et al. [47].

The starting DWNT is shown in Fig. 3.5. The selected DWNT was armchair (3,3) in armchair (8,8). The unit cell of the system includes up to 220 carbon atoms. To eliminate the length effect, periodic boundary condition was applied along the DWNT axis. Self-consistent-charge (SCC) density functional tight-binding (DFTB) was used to prepare fully optimized structures of the DWNT. It should be noted that SCC-DFTB is a fast, approximate quantum mechanical technique that can be treated as an approximated density functional theory as shown in Chapter 2. SCC-DFTB combines low numerical cost with relatively good accuracy [48-49]. It can therefore be considered as a valuable tool in the analysis of this system.

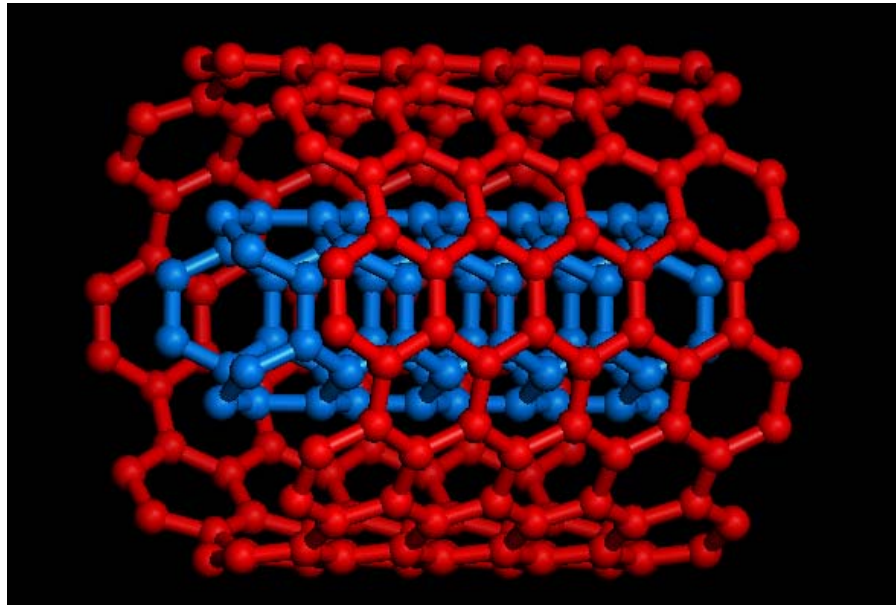


Figure 3.5: Geometry of the DWNT (armchair (3,3) in armchair (8,8)).

To model SiCNTs, adding of Si atoms to DWNT can be studied in three difference ways:

- (i) To add Si atoms between interwall space (IWS) of DWNT and optimize them by DFTB+
- (ii) To simulate SiCNTs growth via Si diffusion by DFTB+/MD simulation
- (iii) To design SiCNTs by using sp^2 and sp^3 crystal structure of SiC system and optimize them by DFTB+.

For the first task, one Si atom was manually added between IWS of the DWNT. Then, the system (DWNT+Si 1 atom) was fully optimized by using DFTB+ method. After optimization, another Si atom was added near the first Si atom (2.34 Å). For the second task (to simulate SiCNTs growth via Si diffusion), the optimized DWNT was first equilibrated at 1500 K for 10 ps. The effect of temperatures including 2000K and 3000K was studied also. Then, a gas-phase feedstock Si atom was supplied around the DWNT surface every 0.5 ps. The velocity vectors of the incident Si atoms were set with an incident energy. The system was studied both NVT and NVE ensembles. For the last task, SiCNTs were designed as SiC graphitic-like structures (sp^2) and bulk phases of SiC structures (sp^3). These designed structures

were fully optimized by using DFTB+ method. The final structures were compared with the experimental results.

3.3 Results and Discussion

The optimized structure of the DWNT and its C-C bond length is shown in Fig. 3.6.

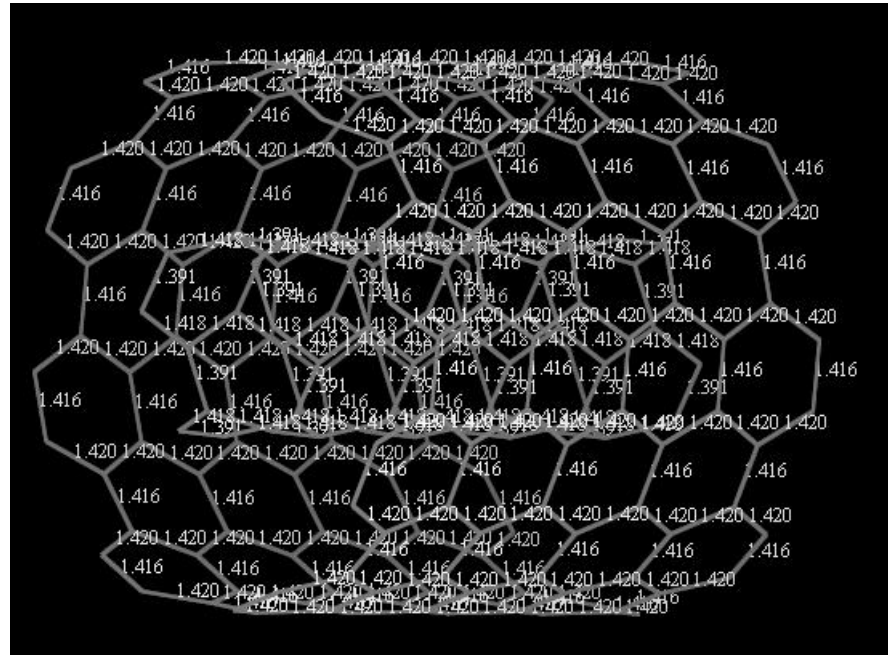


Figure 3.6: Optimized structure of armchair (3,3) in armchair (8,8).

To analyze geometrical features, main bond length (MBL) and ring bond dispersion (RBD) of optimized structure of the DWNT were plotted as shown in Fig. 3.7a and Fig. 3.7b, respectively. The MBL is defined as the mean value for all bonds composing a particular ring:

$$MBL = \frac{1}{6} \sum_{i=1}^6 x_i \quad (3.1)$$

The RBD is defined as a measure of the ring anisotropy:

$$RBD = \sqrt{\sum_{i=1}^6 (x_i - \bar{x})^2} \quad (3.2)$$

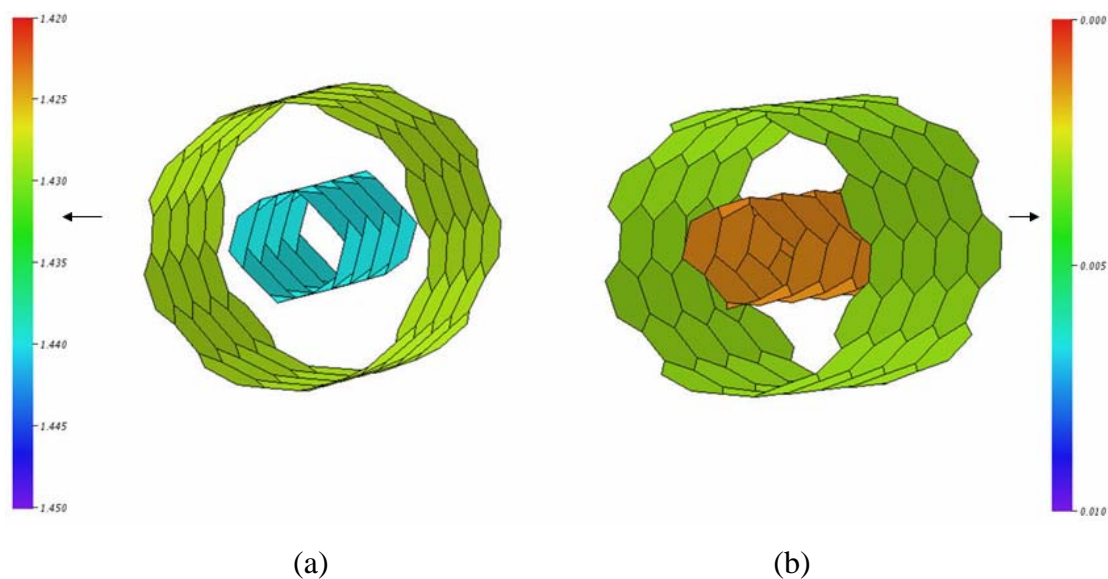


Figure 3.7: (a) MBL and (b) RBD of optimized structure of the DWNT (analyzed by the TubeAnalyzer software).

From MBL plot in Fig. 3.7, one can be seen that the MBL of inner tube ($\sim 1.440 \text{ \AA}$) is a bit larger than that of outer tube ($\sim 1.433 \text{ \AA}$) corresponding to average values of C-C bond length as shown in Table 3.1. The C1–C2 and C2–C3 (see Fig. 3.8) are defined to lie on the circumference and parallel with the tube axis, respectively.

Table 3.1: Average C-C bond length of optimized structure of the DWNT obtained by DFTB method.

	C1-C2 (\AA)	C2-C3 (\AA)	Diameter (\AA)
Inner Tube	1.441	1.438	4.12
Outer Tube	1.431	1.424	10.88

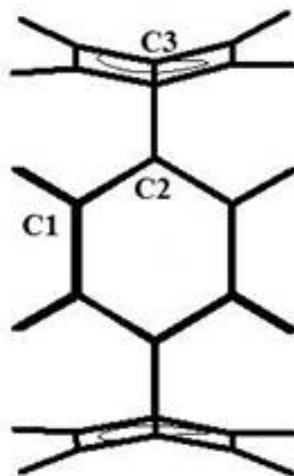


Figure 3.8: Definition of C1–C2 and C2–C3 bonds.

The RBD plot (see Fig. 3.7b) shows the uniform DWNT after optimization by DFTB+. Especially, dispersion of bonds of inner tube is less than 0.003 Å.

3.3.1 Adding of Si atoms between IWS

One Si atom was added between IWS. Initial and optimized structures were shown in Fig. 3.9.

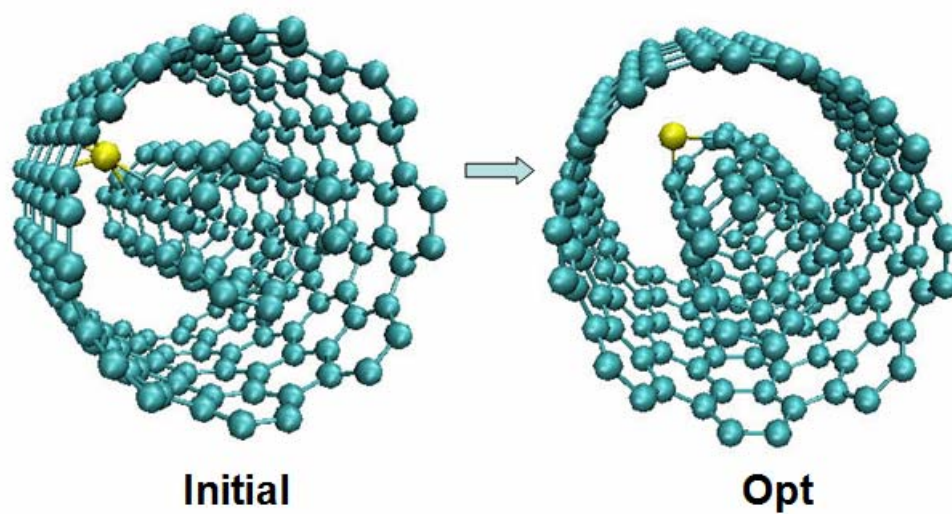


Figure 3.9: Adding of one Si atom.
(Yellow color = Si atom, Green color = C atoms)

After optimization, Si atom prefers to bond sp^2 with C atom of inner tube (See Fig. 3.9). More Si atoms were added with different initial structure as displayed in Fig. 3.10.

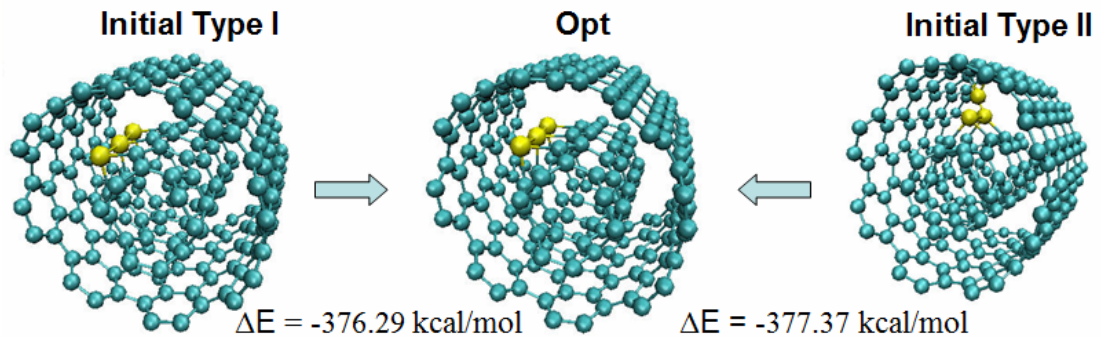


Figure 3.10: Adding of three Si atoms.

(Yellow color = Si atom, Green color = C atoms)

Even though the initial structure has the different Si position, the final structures and interaction energies are quite the similar after optimization (SCCTolerance = $1E-6$). The interaction energy (ΔE) is evaluated via the equation:

$$\Delta E = E(\text{tot}) - E(\text{DWNT}) - nE(\text{Si}) \quad (3.3)$$

where $E(\text{tot})$ denotes the total energy of the DWNT presented with Si atoms. $E(\text{DWNT})$ represents the total energy of the DWNT. n is the number of Si atoms and $E(\text{Si})$ is the total energy of one Si atom.

The MBL and RBD plots of the optimized 3Si-DWNT are shown in Fig. 3.11. The optimized structure tends to preserve the symmetry in X-axis. The MBL plot of inner tube is a bit smaller than that of the original one. The defect at Si positions makes the shrinkage of C-C bond network. It seems to less effect on outer tube since RBD plot of the outer tube shows the uniform bond dispersions (less than 0.003 \AA). However, when more Si atoms were added between IWS, the optimized structure strongly depends on the initial structure as shown in Fig. 3.12. From ΔE , one can be proved that Si atoms prefer to form sp^2 morm than sp^3 since ΔE of sp^2 structure is lower that that of sp^3 structure ($\sim 170 \text{ kcal/mol}$).

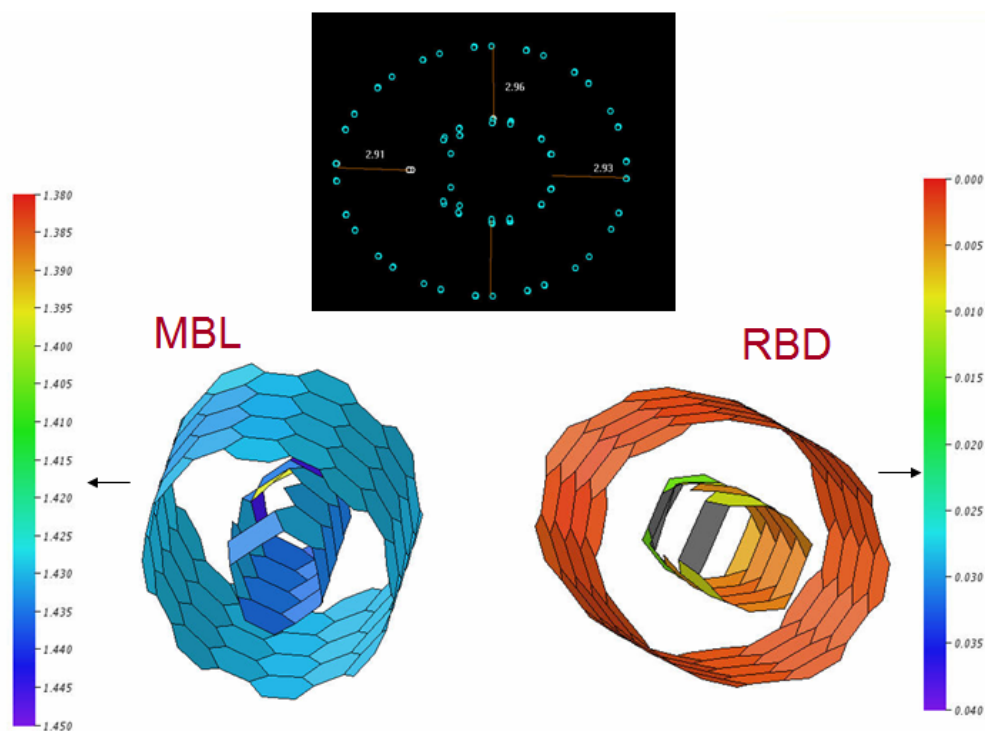


Figure 3.11: MBL and RBD plots of optimized structure of the 3Si-DWNT.
(analyzed by the TubeAnalyzer software)

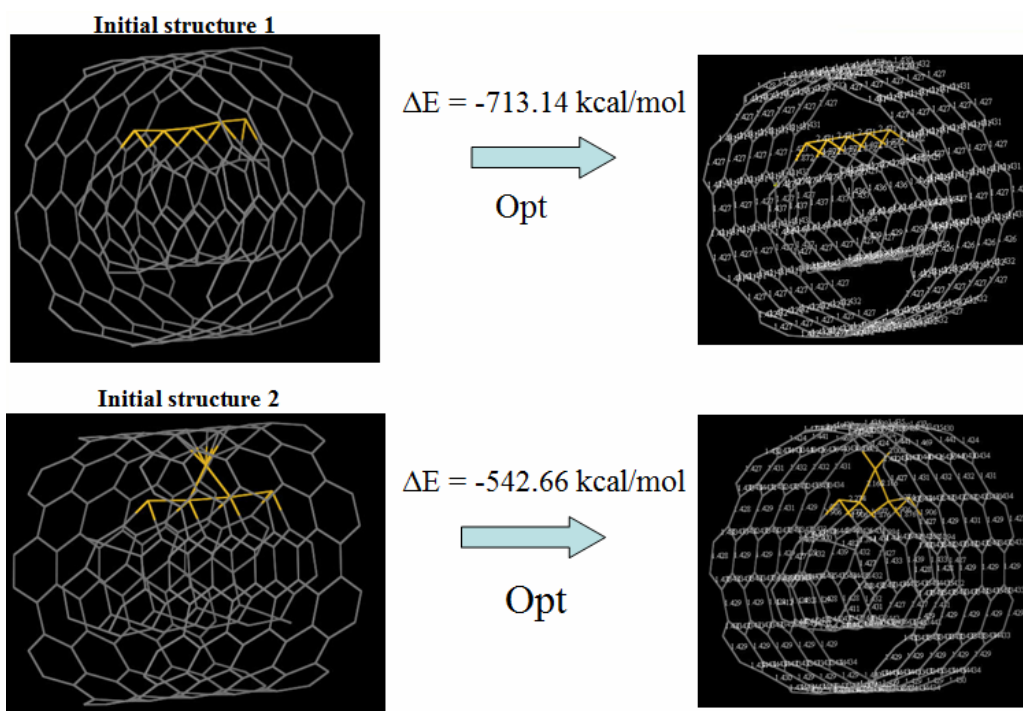


Figure 3.12: Adding of five Si atoms.

3.3.2 Shooting of Si atoms on DWNT surface

In NVT ensemble, Nosé-Hoover chain thermostat [50] was employed. The main advantage of the Nosé-Hoover chain thermostat is that the dynamics of all degrees of freedom are deterministic and time-reversible. No random numbers are used. The Si atoms was randomly supplied around the DWNT surface every 0.5 ps. The results are displayed in Fig. 3.13. Total simulation time was 10 ps.

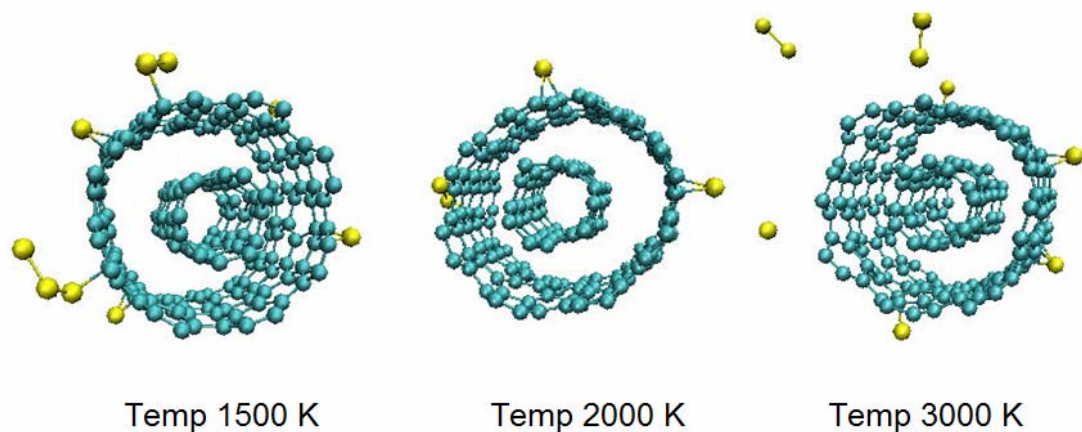


Figure 3.13: Snapshots of shooting of Si atoms around the DWNT surface at 1500 K, 2000K and 3000K. (Yellow color = Si atom, Green color = C atoms)

From Fig. 3.13, it is clearly shown that Si atoms can not come into IWS through the perfect sidewall of DWNT. They try to bond with C atoms of outer tube only. All temperatures show the similar behavior. The mechanism of Si shooting around DWNT surface is displayed in Fig. 3.14. At 0 ps, Si atom is initially at a position. The first C-Si bond occurs at 0.1 ps. At 0.15 ps, the Si atom forms 2 bonds with C atoms and occupies onto the side wall. However, the C-Si bonds are not so strongly. When other Si atoms close to the attached Si atoms (at 2.13 ps), they always make Si clusters (at 4.94 ps) that are easy to leave from sidewall. Therefore, a few Si atoms can occupy at DWNT sidewall. In addition, the kinetic energy of Si atoms is not enough to overcome the binding energy of C-C network. Therefore, they can not go to inside DWNT. To solve this problem, NVE ensemble with increasing incident energy of Si atom was used. The incident energy of Si was set by assignment of an specific Si velocity. The Table 3.2 shows velocities in x-,y-, and z-axis compared with normal Si velocity generated by $T = 1500$ K.

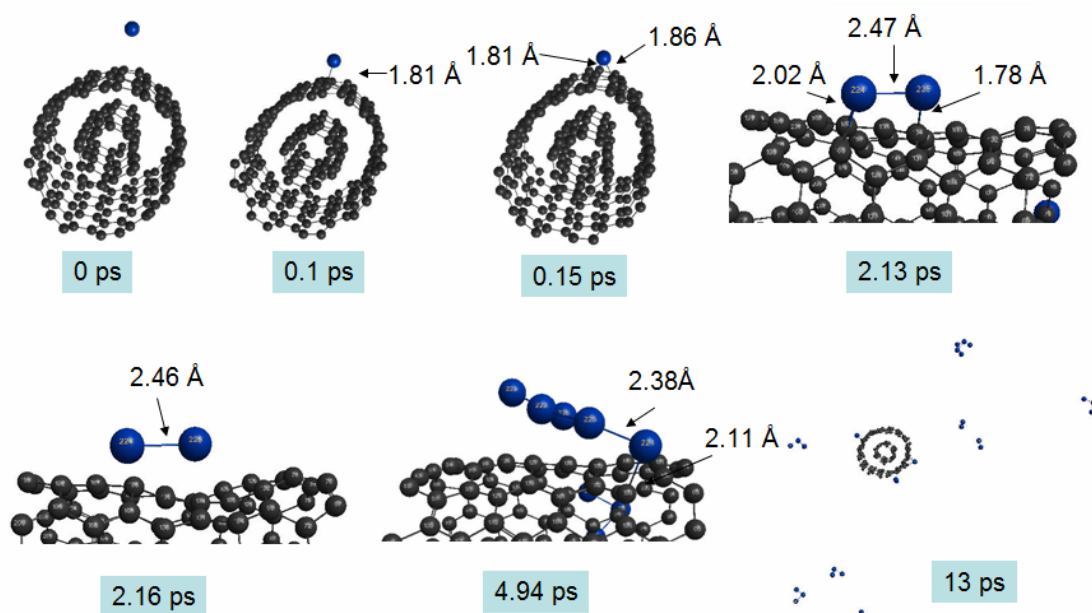


Figure 3.14: Snapshots of shooting of Si atoms around the DWNT surface as a function of time at 1500 K. (Blue color = Si atom, Black color = C atoms)

Table 3.2: Initial velocities assigned to Si atoms.

	V(x)	V(y)	V(z)
2V	0.000378	-0.00032	-6.5E-05
5v	0.000946	-0.0008	-0.00016
10v	0.001891	-0.00161	-0.00033
20v	0.003782	-0.00322	-0.00065
23v	0.00435	-0.0037	-0.00075
25v	0.004728	-0.00402	-0.00082
27v	0.005106	-0.00434	-0.00088
28v	0.005295	-0.0045	-0.00091
29v	0.005484	-0.00466	-0.00095
30v	0.005674	-0.00482	-0.00098
35v	0.006619	-0.00563	-0.00114
40v	0.007565	-0.00643	-0.00131
45v	0.00851	-0.00724	-0.00147
50v	0.009456	-0.00804	-0.00163

The relationship between temperature and kinetic energy can be calculated from Boltzmann distribution. In summary, the equation can be written down as:

$$\frac{1}{2}mv^2 = \frac{3}{2}kT \rightarrow T = \frac{mv^2}{3k} \quad (3.3)$$

From the simulations, it was found that Si atom needs at least 29 times of normal velocity to enter into IWS through the perfect DWNT sidewall as shown in Fig. 3.15. However, if kinetic energy of Si atom is so high, it is easy to destroy the pristine DWNT.

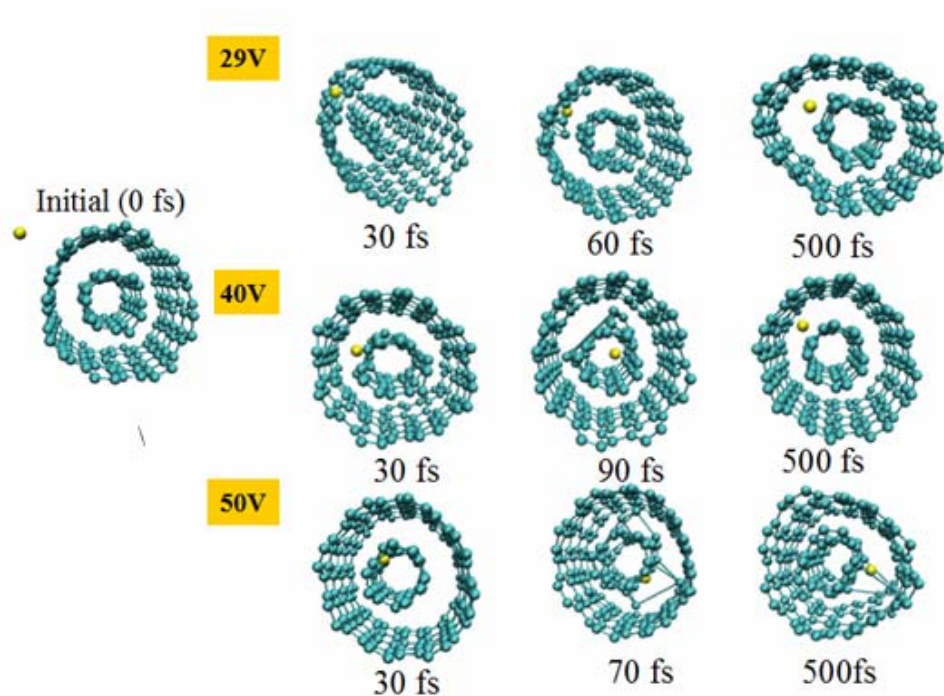


Figure 3.15: Snapshots of shooting of one Si atom at different velocity as a function of time. (Yellow color = Si atom, Green color = C atoms)

The Si with 29 times of normal velocity was selected to continue the shooting. One Si atom was shot around the DWNT surface at this velocity every 0.5 ps. The total simulation was 3 ps (Total Si atoms = 6 atoms). The results are shown in Fig. 3.16. At high energy of Si atoms, the Si atoms can enter into IWS but they hit C atoms of DWNT backbone resulting to decompose inner tube and unzip outer tube.

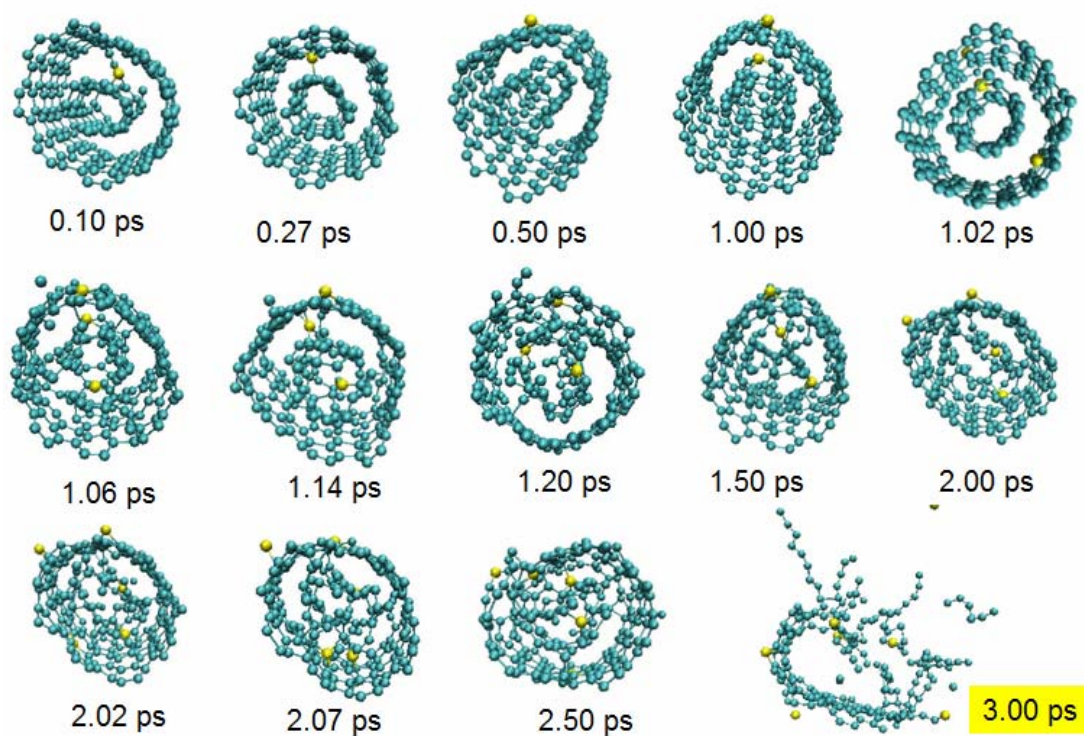


Figure 3.16: Snapshots of shooting of Si atoms at high velocity as a function of time.
(Yellow color = Si atom, Green color = C atoms)

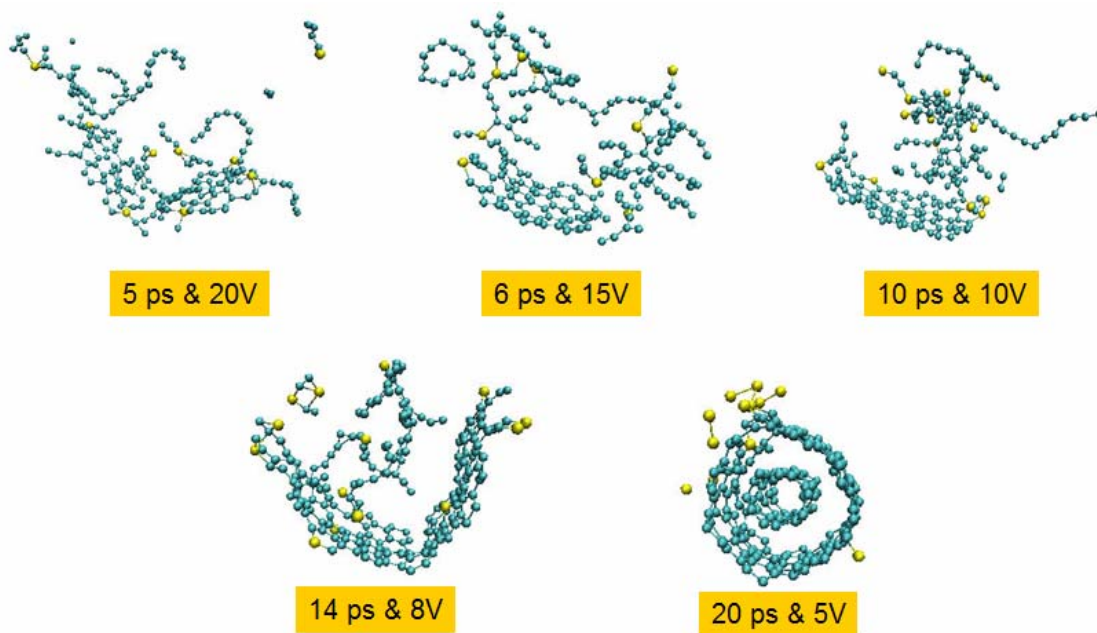


Figure 3.17: Snapshots of shooting of Si atoms at different high velocities.
(Yellow color = Si atom, Green color = C atoms)

The lower energies of Si atoms were tested. The results are shown in Fig. 3.17. Even though, kinetic energy of Si atoms was reduced more than 50%, the decomposition of DWNT still occurs. The lower energies of Si atom only extend the time to decompose the pristine DWNT. From the results, it can be believed that Si atom can not go inside DWNT through the perfect sidewall to form a SiC nanotube. Introduction of defects on sidewall may play the important role for real SiC formation. This hypothesis was proved by the one vacancy defect on DWNT sidewall. The optimized structure of DWNT with one vacancy defect is displayed in Fig. 3.18.

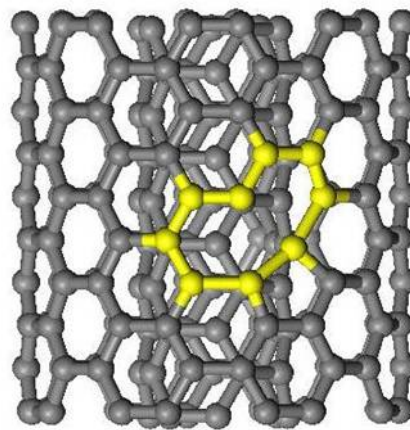


Figure 3.18: Optimized structure of DWNT with one vacancy defect using DFTB+. (Yellow color shows the defect region)

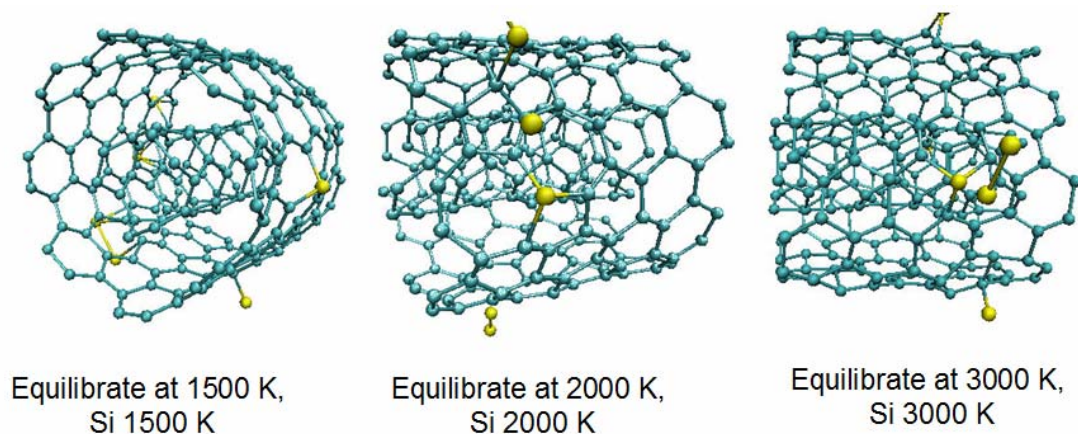


Figure 3.19: Snapshots of shooting of Si atoms onto defect DWNT. (Yellow color = Si atom, Green color = C atoms)

After shooting 6 Si atoms (Total simulation time = 3ps), the results are displayed in Fig. 3.19. A Si atom can form sp^2 with C-C network on sidewall. It does not generate any distortions of DWNT structure. Based on this study, it can be concluded that formation of SiC nanotube uses defects during synthesis.

3.3.3 Model final structure of SiCNT

The SiCNT can be designed to two models including SiC graphitic-like structures (sp^2) and bulk phases of SiC structures (sp^3). In case bulk phases of SiC, hexagonal and cubic structures were employed to design zigzag and armchair SiCNTs, respectively. The initial structures of such SiCNTs are displayed in Fig. 3.20.

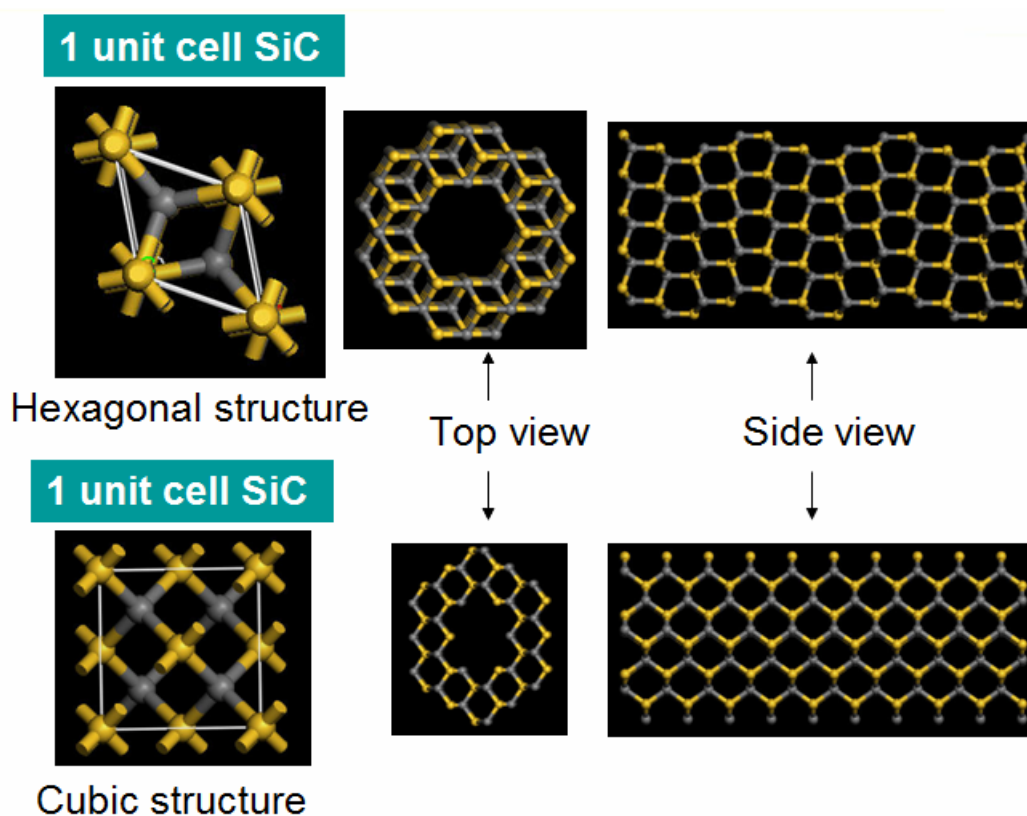


Figure 3.20: Initial structures of SiCNTs designed from bulk phases of SiC structures. (Yellow color = Si atom, Black color = C atoms)

After optimization by DFTB+, the final structures are shown in Fig. 3.21. One can be seen that zigzag SiCNT has a good cylinder structure with sp^3 hybridization.

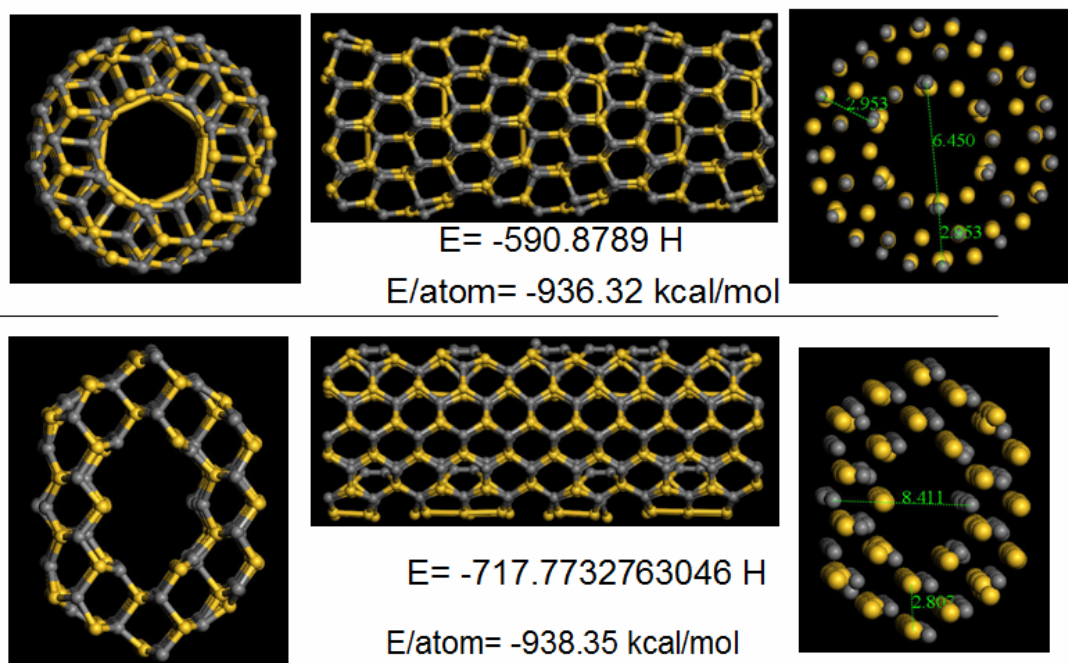


Figure 3.21: Optimized structures of SiCNTs (sp^3) based on DFTB+. (Yellow color = Si atom, Black color = C atoms)

In case of SiC graphitic-like structures (sp^2), C atoms were substituted by Si atoms reached to Si:C = 1:1. The optimized structure of SiC graphitic-like structures is displayed in Fig. 3.22.

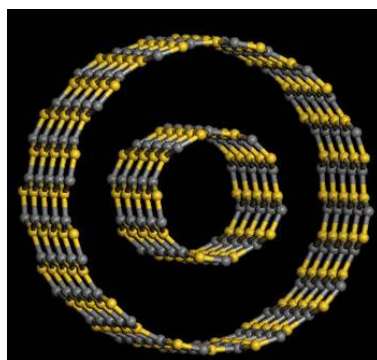


Figure 3.22: Optimized structures of SiCNTs (sp^2) based on DFTB+. (Yellow color = Si atom, Black color = C atoms)

To compare the models with experimental results (see Fig. 3.23), typical multiwalled SiCNTs have the interlayer spacing in range of 3.5-4.5 Å [36] corresponding the sp^2 model.

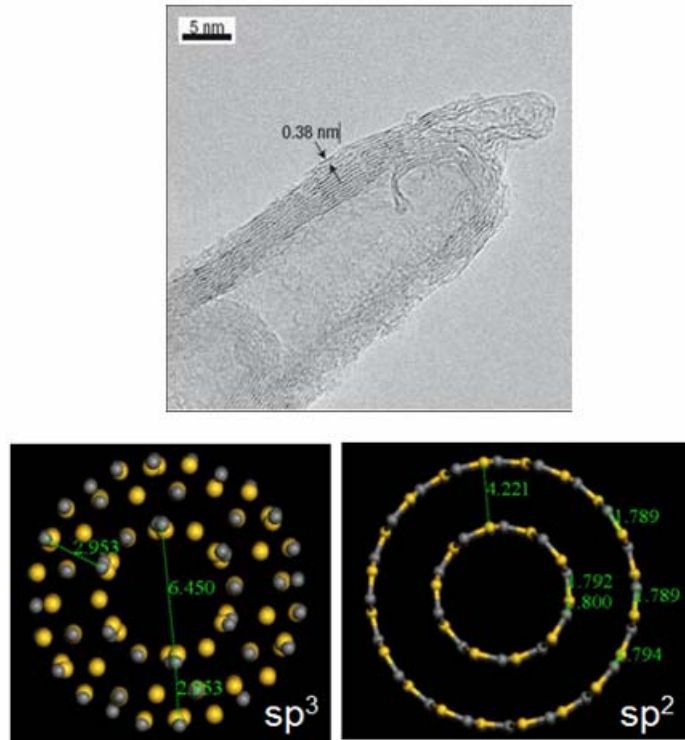


Figure 3.23: Comparison between experimental result and model SiCNTs.
(Upper picture from X. H. Sun, *J. Am. Chem. Soc.* 124 (2002) pp. 14467)

3.4 Conclusion

- Si atoms can not go into the IWS through a perfect sidewall. The Si atoms trends to be adsorbed on the sidewall of outer tube and they are easy to leave out from tube sidewall due to formation of Si cluster.
- At high energy of Si atoms, Si atoms will decompose inner tube and unzip outer tube.
- Defects on side wall of CNTs are necessary to form SiC nanotube.
- SiCNTs prefers to form sp^2 bonds between a Si atom and a C atom.

CHAPTER IV

SYNTHESIS OF NANOMATERIALS

4.1 Top-down and Bottom-up Methods

In general, there are two approaches for the manufacture of nanoscale materials, namely; (I) top-down and (II) bottom-up methods. The top-down method refers to the uses of the traditional workshop or microfabrication method to cut, mill, and shape materials into the desired shape and order. The best known example of top-down method is lithography process (see Fig. 4.1). For example, a silicon wafer is coated with a layer of photoresist by spin coating technique. The photo resist-coated wafer is then prebaked to drive off excess on a hotplate. After prebaking, the photoresist is exposed to a pattern of intense light. The lithography is used to shine light on only certain parts of the wafer. Some lithography (i.e. E-beam) can provide patterns down to 10 nm. For most photoresists, the light breaks down that portion of the coating and frees it up for etching and doping. This is top-down method because it starts from a bulk material.

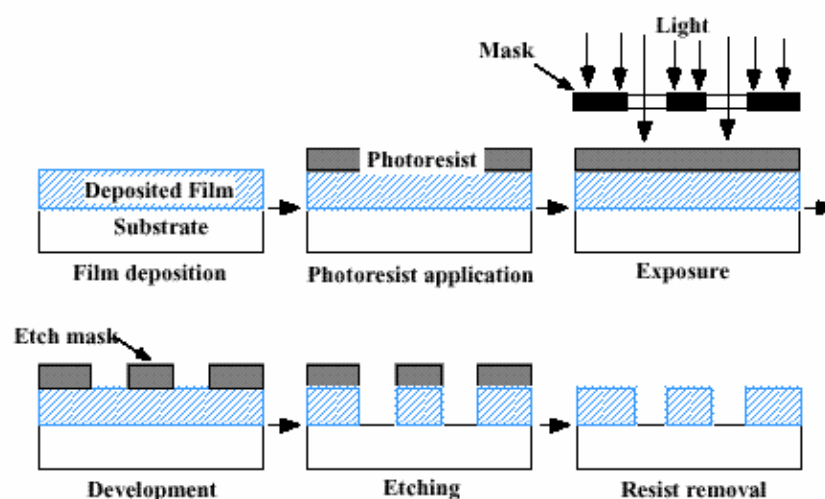


Figure 4.1: Photolithography process.

(Fig. from >> <http://www.hitequest.com/Kiss/VLSI.htm>)

The bottom-up method refers to methods that can create from smaller components (usually molecular) built up into more complex assemblies. There are two fundamentally different ways of fabricating things from the bottom up [51].

- Self-assembly: is common throughout nature and involves components from the molecular (e.g. protein folding) to the planetary scale (e.g. weather systems) and even beyond (e.g. galaxies).

- Molecular assembly: is proposed that device is able to guide chemical reactions by positioning reactive molecules with atomic precision. Example of bottom-up method is ZnO nanostructure which appeared as a bear shape as shown in Fig. 4.2.

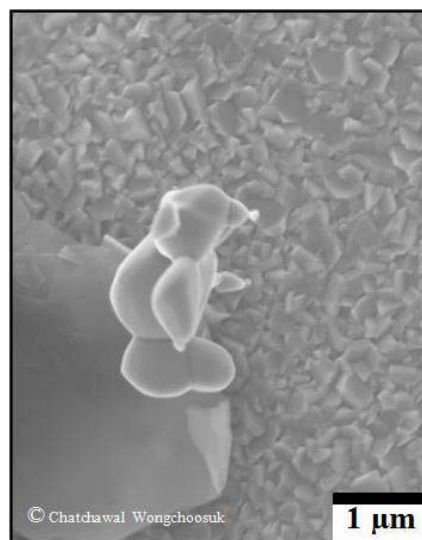


Figure 4.2: ZnO nanobear.

4.2 Vapor–Liquid–Solid & Vapor–Solid Mechanisms

The vapor-liquid-solid (VLS) [52] and vapor-solid (VS) methods are the mechanisms for the growth of one-dimensional structures from chemical vapor deposition such as nanowires. In principal, the VLS growth process is characterized by the presence of a metal particle at the NW tip and offers the possibility for diameter and arrangement control via the patterned arrays of catalyst [53]. The VLS mechanism is typically described in three stages. At first, a liquid alloy droplet is prepared upon the substrate. It should be noted that a nanowire is grown at the liquid alloy droplet position. Next, the vapor source material adsorbs on to the liquid

surface, and diffuses in to the droplet. In last stage, supersaturation and nucleation at the liquid/solid interface occur. It leads to axial crystal growth.

In case of the VS mechanism, nanowire growth is still based on using metal dots as starting points. However, surface defects or dislocations on the substrate can also provide energetically favored nucleation sites to grow nanowire. In VS process, the growth parameters are controlled in a way that the dots remain mainly solid [54]. Schematic demonstration of the two different nanowire growth modes namely VLS and VS mechanism is shown in Fig. 4.3. In addition, VS nanowires were observed that they grow slower (10-100 times) than VLS nanowires because of the lower diffusivity, the contributions of desorption, and the weaker surface reactivity in the solid phases [53].

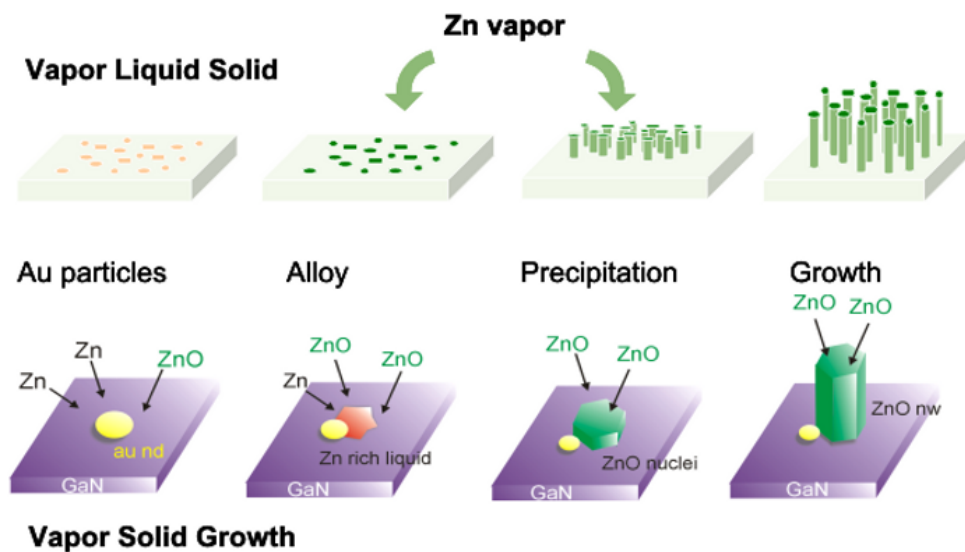


Figure 4.3: VLS & VS mechanisms.

(Fig. From Advances in Solid State Physics 48 (2009) pp. 5)

CHAPTER V

GROWTH OF UNIFORM LARGE-SCALE ARRAYS OF ZINC OXIDE NANOSTRUCTURES

5.1 Introduction of ZnO Nanostructures

Semiconducting nanowires (NWs) in general and ZnO NWs in particular have been widely studied in the last decade due to their unique properties facilitated by their nano size. Initially, much work focused on demonstration of “application or device concepts” based on single nanowires [55]. It is, however, currently most desirable to develop the level of understanding and control of nanowire growth required to obtain reliable, narrowly distributed and reproducible structure and properties necessary for real industrial applications [56]. The unique combination of properties of ZnO nanowires provides additional options for its utilization for electronic, optical and mechanical applications particular if the p-doping issue is solved [57].

ZnO nanomaterials can be grown in an amazingly rich variety of shapes and nanostructures such as nanowires [58], nanobelts [59], nanocombs [60], nanohelices [61], nanowalls [62], and others. The vapor phase transport process allows a simple fabrication of these various nanoproducts by modifying the growth parameters such as the growth precursors, the carrier gas composition, its pressure and flow, the nature of the substrate on which the nanostructures grow, and the source and substrate temperatures. The difficulty of defining the large number of intertwined parameters involved in the variety of systems applied is a big obstacle for obtaining a meaningful correlation between the growth conditions and the resulting morphology applicable to the variety of different systems used.

This chapter presents a systematic study of the growth of ZnO nanostructures in a thermal CVD system focusing on the source powder temperature (T_p) and on the substrate temperature (T_s) by keeping all other parameters constant.

This provides a shape diagram which relates the different ZnO nanostructures to T_s and T_p . This diagram is applicable to a variety of systems (as demonstrated by a selective comparative study with a laser ablation system) and provides insight into the mechanisms leading to the evolution of these nanowires.

5.2 Experimental Details

ZnO nanowires were grown by a vapor phase transport process in a two-zone heating furnace (allowing independent control of the temperature profile of these two zones) with a horizontal quartz tube (5 cm inner diameter and 106 cm long) as shown in Fig. 5.1a.

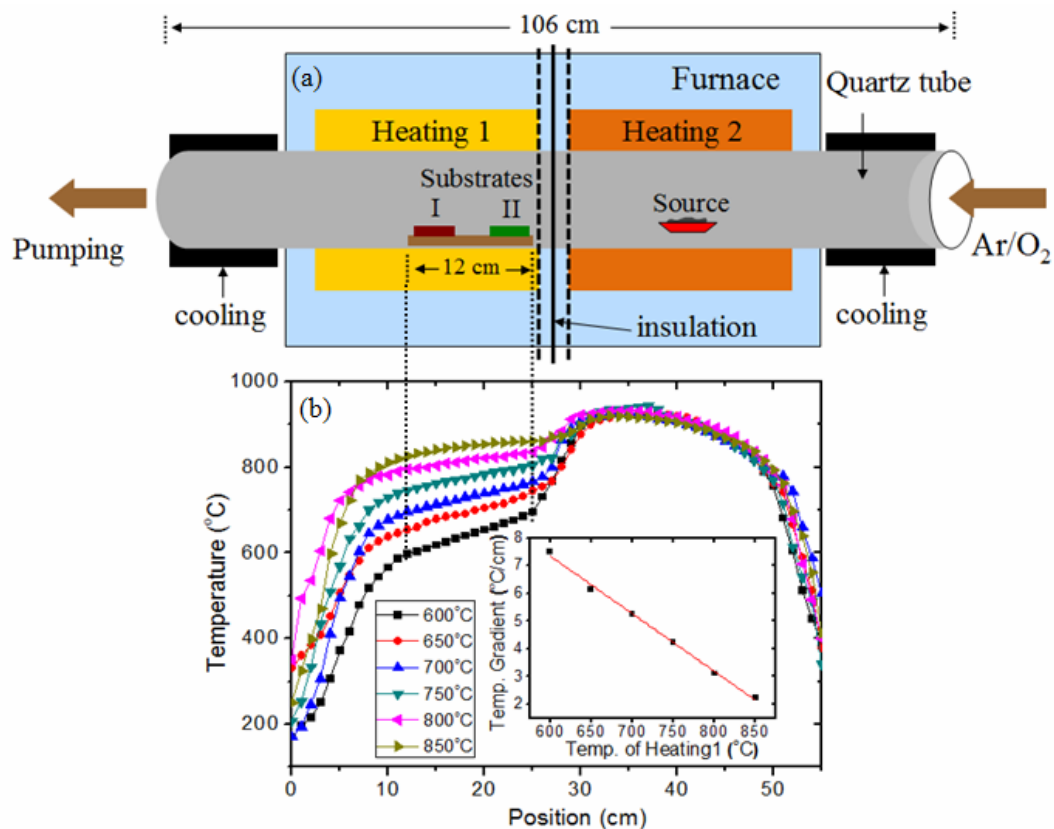


Figure 5.1: (a) Schematic diagram of the thermal CVD growth system. (b) Temperature profile of the two-zone heating furnace. The inset in (b) shows temperature gradient versus temperature of heating 1 with a fixed heating 2 temperature of 950 °C. Heating 1 temperature is measured 12 cm away from the right edge of heating 1 zone (the edge neighboring heating zone 2).

GaN/sapphire substrates deposited by 5 nm Au were used. The substrates were placed at downstream positions (with respect to the source) marked as I and II in Fig. 5.1a. A 1:1 weight mixture of ZnO (99.999% purity) and graphite (99.99% purity) powders was placed in a quartz boat in the center of heating zone 2. The tube was pumped to a base pressure of 4×10^{-5} mbar. The flow shutter approach [63] was applied to suppress undesirable ZnO deposition during the heating ramp in the following way: The tube was kept at a pressure of 1 bar, a flow of 30 sccm Ar (99.9999%) and 1.5 sccm Ar/O₂ mixture (90/10at% Ar/O₂, purity 99.999%) during the heating up period. T_s and T_p were chosen in the ranges of 650–950 °C and 850–1050 °C, respectively. When both T_s and T_p reached the desired set point temperatures, the pressure inside the tube was reduced from 1 bar to 30 mbar for 10 minutes enabling deposition. The flow shutter was operated again after these 10 minutes of deposition. The furnace was then slowly cooled down to room temperature. The morphology of the samples was examined by scanning electron microscopy (SEM, FEI Nova™ NanoSEM). A selective number of samples under similar T_s , pressure and flow conditions were grown using a laser ablation system described elsewhere [64]. The structure of selected samples was studied using high-resolution transmission electron microscopy (HRTEM).

5.3 Temperature Profile of the Two-zone Furnace

The temperature profiles of the two-zone furnace tube for different T_s and T_p are displayed in Fig. 5.1b. The temperature gradient depends linearly on the temperature of heating zone 1 as shown in the inset of Fig. 5.1b. All growth experiments were performed on substrates that were partially deposited by Au and partially not deposited (using a shadow mask). As shown in Fig. 5.2, ZnO nanostructures growth was observed only on the Au deposited parts indicating catalyst assisted nucleation for all samples studied in the present work in the specific parameter window.

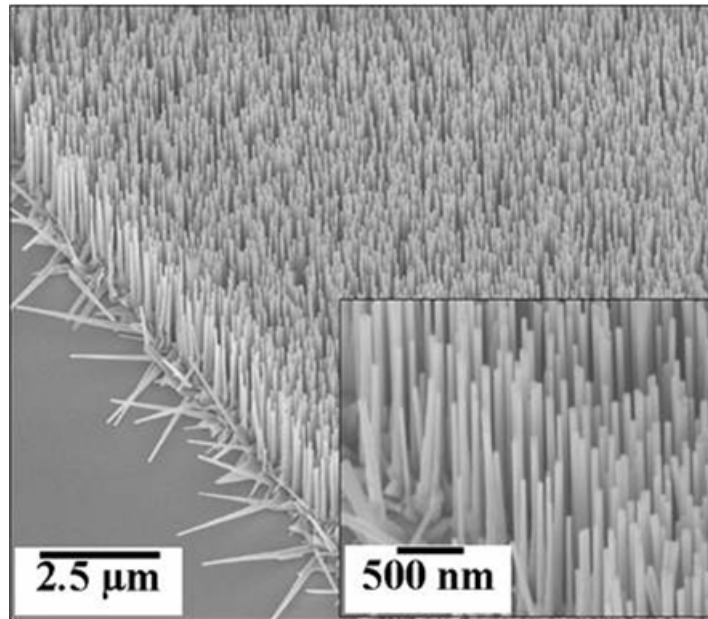


Figure 5.2: SEM images of ZnO nanowires grown at position II with $T_p = 950^\circ\text{C}$ and $T_s = 800^\circ\text{C}$. No Au tips are noticed indicating catalyst free VS growth.

5.4 Shape Diagram of ZnO Nanostructures as a Function of T_s and T_p

Fig. 5.3 presents a diagram of the evolving morphologies of ZnO nanostructures at different T_s (650-950°C) and T_p (850-1050°C) fixing all other growth parameters as previously described [65]. No nucleation occurs at low T_p ($< 900^\circ\text{C}$) and T_s ($< 800^\circ\text{C}$). ZnO nanostructures start nucleating on the GaN substrates at $T_p = 900^\circ\text{C}$ and $T_s > 800^\circ\text{C}$ (samples A). ZnO nuclei develop below the Au droplets at 820°C and at slightly larger T_s of 875°C (faster kinetics) one already observes short ZnO nanowires with Au dots at the tip indicating catalyst assisted growth. Similar structures were observed for 820 °C for laser ablation as demonstrated in Fig. 5.4. Well-aligned, uniform (hundreds of nm long) ZnO nanowires free of Au dots at their tips were observed at T_p of 950 °C and T_s in the range of 700 - 800 °C as shown in Fig. 5.3b (samples B). The lack of Au at the tips indicates a catalyst free (e.g. VS) growth process at this parameter region. The T_s effect on the nanowire diameter and length in this growth regime at fixed T_p of 950°C (samples B) was studied by either doing separate experiments with different T_s at

position II or by putting two samples at two different locations in the same experiment (I and II in Fig. 5.1) using the advantage of the weak thermal gradient in between. In both cases the diameter of the NWs decreased with increasing T_s while their length increased with T_s .

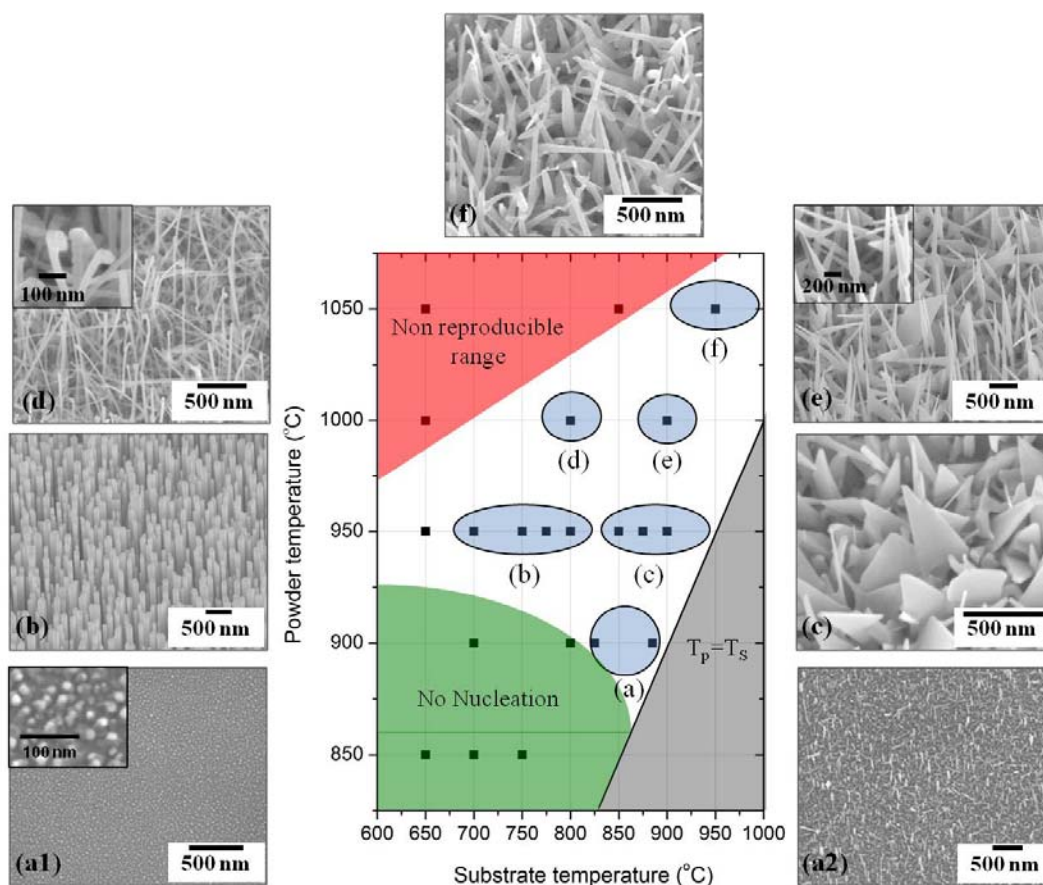


Figure 5.3: Shape diagram of ZnO nanostructures formed at different T_s and T_p which includes: (a) nanowires nuclei (sample A), (b) aligned nanowires (sample B), (c) mostly triangular nanosheets (sample C), (d) nanohammers (sample D), nanospars (sample E), and nanopins (sample F). Note that pure catalyst free (VS) growth is observed only at B and all others are catalyst assisted (VLS) as deduced from the Au dots at the nanostructures tips. No growth was observed on the bare surface of the samples, i.e. the nucleation was *always* catalyst assisted.

However, if the T_s is too low ($< 650\text{ }^\circ\text{C}$), a ZnO film was formed prior to the evolution of nanowires leading to randomly oriented nanowires on GaN substrates. When T_s increases to $850\text{-}900\text{ }^\circ\text{C}$, keeping a fixed T_p of $950\text{ }^\circ\text{C}$, the ZnO nanostructures contain Au dots in their tips indicating that a catalyst assisted growth process (e.g. VLS) becomes active, in contrast with the growth at lower T_s . This is associated with a morphology change from purely aligned nanowires to a mixture of morphologies including (typically triangular) nanosheets (samples C) as shown in Fig. 5.3c. Further increase of T_p to $1000\text{ }^\circ\text{C}$ and to $1050\text{ }^\circ\text{C}$ leads to the growth of different morphologies, all having Au dots at their tips. ZnO hammer-like (sample D) and spear-like (sample E) structures were obtained at $T_s = 800\text{ }^\circ\text{C}$ (Fig. 5.3d) and $T_s = 900\text{ }^\circ\text{C}$ (Fig. 5.3e), respectively. ZnO pin-like structures (sample F) with tip sizes in the range of $10\text{-}20\text{ nm}$ are observed for $T_p = 1000\text{ }^\circ\text{C}$ and $T_s = 950\text{ }^\circ\text{C}$ as shown in Fig. 5.3f. In the red colored zone of the shape diagram the synthesized products are made of inhomogeneous structures indicating unstable growth conditions at this part of the diagram.

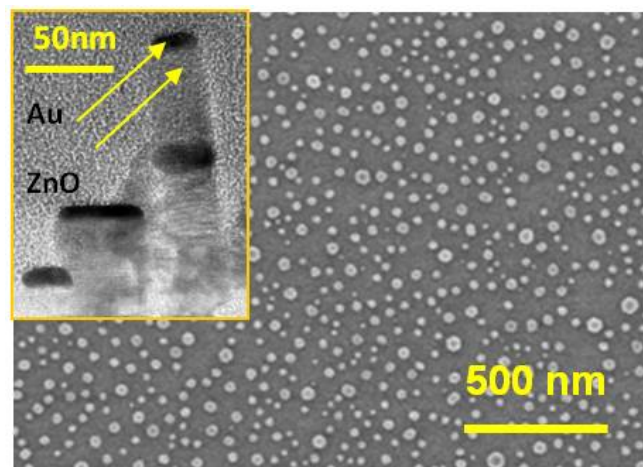


Figure 5.4: SEM image of ZnO nanostructures grown using laser ablation at $T_s=820\text{ }^\circ\text{C}$ (Ar 300 mbar, 30 sccm Ar) having a similar morphology to that of samples A in the shape diagram. The inset TEM image reveals an Au dot at the tip.

5.5 Mechanisms of the ZnO nanostructures

Many parameters affect the growth of nanostructures in general and that of ZnO nanostructures in particular. These include (1) the source (nature and generation rate of growth species), (2) the transport of the growth species to the substrates on which the nanostructures grow (type of carrier gas, its pressure and flow), (3) the system geometry affecting the amount and nature of growth species reaching the substrate, (4) the substrate (type, use of a catalyst), (5) the substrate temperature (affecting the kinetics and the thermodynamics of the condensation and the growth).

Table 5.1: Reduction of ZnO with C at different T_p temperatures, forming Zn vapor calculated following Rao [66]

T_p (°C)	Zn vapor partial pressure (bar)
827	0.158
877	0.361
927	0.770
977	1.545
1027	2.939
1077	5.330
1127	9.265
1177	15.50
1227	25.06

In the present work we have chosen to fix all parameters except two: the substrate temperature (T_s), and the source temperature (T_p). While the effect of T_s is relatively simple to evaluate, that of T_p in our case is more complex. Most of the present work was performed using an evaporation source of a 1:1 weight mixture of ZnO and carbon which react upon heating to yield Zn, CO and CO₂. We additionally feed the system by O₂ so that ZnO vapor is also available in the vicinity of the target,

as well as the other species mentioned. We assume as a first order approximation that the flux of the growth species is the only parameter changed by increasing T_p and that their composition is not changing with T_p . Reduction of the ZnO with carbon results in an increase of the partial pressure of Zn vapor with increasing T_p in the temperature range (850-1050°C) by more than a factor of 10 as calculated by Rao [66] (see Table 1).

In order to overcome the complex nature of the source we verified some of the findings of the present work by adding data coming from a laser ablation system in which the only growth species are ablated ZnO molecules with no carbon containing molecules involved [64].

The growth of ZnO nanostructures involves two separate stages: **nucleation and growth**. In previous work (performed using a laser ablation system [64]) it was shown that three different growth modes are possible: (i) *catalyst free nucleation and catalyst free growth* (use of bare, catalyst free substrates), (ii) *catalyst assisted nucleation and catalyst free growth* [67] (catalyst deposited substrates, grown nanostructures do not have catalyst tips), (iii) *catalyst assisted nucleation and growth* (catalyst tips observed). A catalyst free stage is associated with a vapor-solid (VS) nucleation/growth while a catalyst assisted stage is associated with a vapor-liquid-solid (VLS) nucleation/growth. In our previous work [64], we proposed that the catalyst assisted growth is not the classical VLS mechanism associated with diffusion through the catalyst and precipitation in the catalyst-substrate interface but a surface diffusion process to the lower hemisphere of the catalyst droplet, minimizing the surface energy by precipitating at the interface as was discussed before for micrometer sized whiskers [68].

By establishing the shape diagram shown in Fig. 5.3, we are now able to provide some insight into the role of T_p and T_s in the development of ZnO nanostructures. First, we note that all nanostructures evolving in the present study nucleated via a catalyst assisted process and no nucleation was observed on bare substrates (compare Fig. 5.2). This nucleation requires a minimal concentration of growth species (no nucleation below $T_p=900^\circ\text{C}$) and a minimal substrate temperature (T_s) to facilitate the appropriate surface adsorption as well as surface diffusion rate of the growth species to allow both nucleation and growth (see samples A). By

increasing T_p from 900 to 950°C we increase the evaporation rate of the Zn vapor by nearly a factor of two, hence enhancing the adsorption probability. At relatively low T_s (700-800°C) the condensation rate of the growth species is sufficiently large to promote VS growth (the driving force of which is the asymmetry of the ZnO crystal with the [0001] as the fast growth direction). At this stage the concentration of the growth species and their surface diffusion rate around the Au droplet are still too low to facilitate catalyst assisted growth so that we observe ZnO nanowires uniquely grown by VS (samples B). Moreover, the ZnO base on which the nanowire nucleates should be larger for lower T_s (larger condensation rate) so that one expects larger diameter but shorter wires (slower growth kinetics as dictated by diffusion) to form with decreasing T_s as we indeed observed (Fig. 5.5).

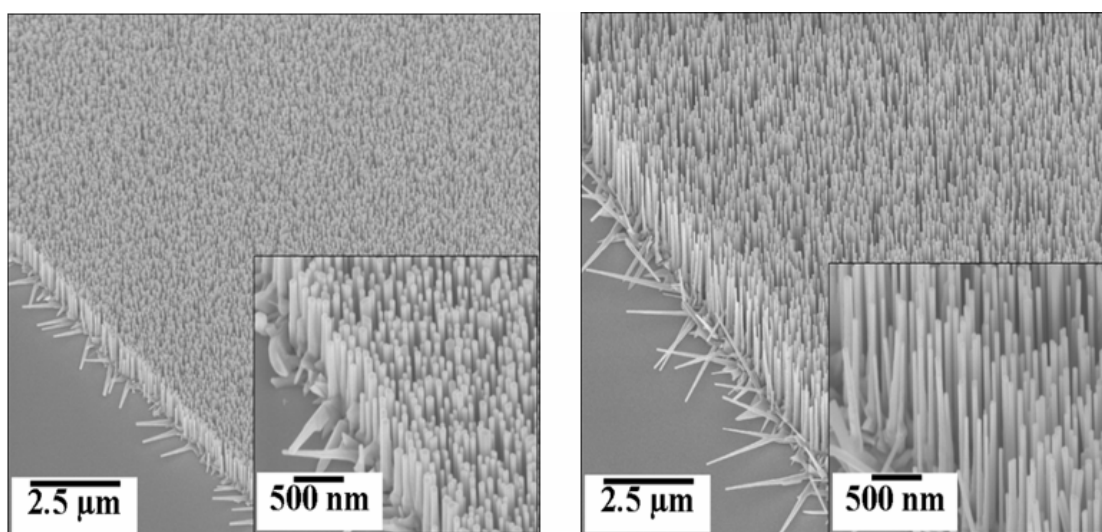


Figure 5.5: ZnO nanowires with decreasing T_s .

Once T_s increases above 800°C the diffusion rate increases and catalyst assisted growth becomes feasible. The dominating morphology (samples C) becomes that of triangular nanosheets with Au observed at their tips. Similar nanosheets were also observed in ZnO nanostructures grown by laser ablation at $T_s=900^\circ\text{C}$ (Fig. 5.6). TEM images of these nanosheets indicate that the growth direction of the triangle sides is always [0001] while that of the Au tip may have different directions (Fig. 5.6 b, c). This leads us to the conclusion that in this regime both the catalyst free (VS) and

the catalyst assisted (VLS) modes are occurring simultaneously, leading to triangular nanosheets.

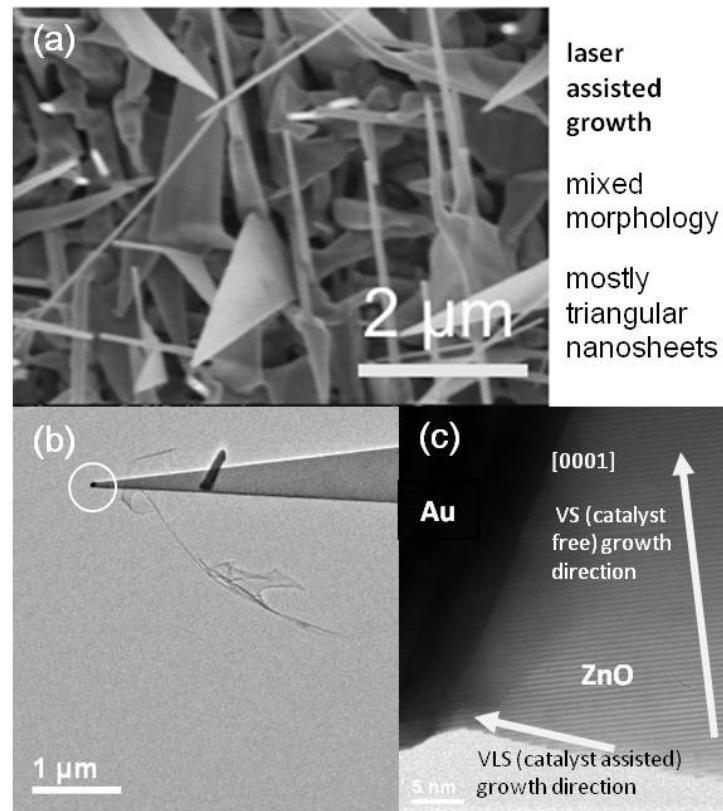


Figure 5.6: ZnO nanostructures grown using laser ablation at $T_s=900^\circ\text{C}$ (70 torr, 50 sccm Ar) having a similar morphology to that of samples C in the shape diagram. (a) SEM image, (b) TEM image revealing an Au dot at the tip, (c) Cross-sectional HRTEM image of the tip indicating that the growth direction dictated by the tip is different than the growth direction ([0001]) of the free side of the triangular sheet. The sheet thus grows by a combination of the VS (catalyst free) and VLS (catalyst assisted) mechanisms.

We now understand that sufficient T_p and T_s would lead to catalyst assisted growth as observed for samples D, E and F (Fig. 5.3). If the Zn incorporation rate by a catalyst assisted VLS growth is not large enough to consume a large concentration of Zn (as expected for large T_p) we might get not only catalyst assisted growth, but also side growth which becomes thicker with time. This is the origin of

the spear-like morphology observed for sample E (Fig. 5.3 e). The present study applied the flow shutter approach to eliminate growth under uncontrolled conditions especially those prevailing at the end of the process (cooling of the system). Such varying conditions may nevertheless explain the hammer-like morphologies obtained in (D) since the hammer is always at the tip of the wires no matter what their length is. This might indicate that the flow shutter approach does not guarantee stable conditions in all parameter cases during the cooling down period.

5.6 Conclusion

In summary, the role of T_p and T_s in determination of ZnO nanostructured morphologies was studied utilizing a carbothermal CVD approach with a two zone furnace. A shape diagram of the dependence of the morphology on T_s and T_p was constructed. Zones of catalyst free (VS) and catalyst assisted growth were identified and explained in terms of the effects of T_s and T_p in these different growth mechanisms. Selective comparative studies of ZnO growth via a laser ablation system yielded morphologies in accord with the carbothermal CVD work showing the validity of our hereby suggested phase diagram.

CHAPTER VI NANOSTRUCTURE GAS SENSORS

6.1 Fundamental Principles of Metal Oxide Gas Sensors

Metal oxide semiconductor (MOS) sensors such as SnO₂ sensor are widely used in the sensing element due to low cost and response on various volatile organic compounds. Basic principle of principle can be expressed as follows from Ref [69]. In details, MOS such as SnO₂ can be operated at high temperature in air. When it is heated, oxygen will be adsorbed on the crystal surface with a negative charge. Then, donor electrons in the crystal surface are transferred to the adsorbed oxygen, resulting in leaving positive charges in a space charge layer. Thus, surface potential is formed to serve as a potential barrier against electron flow as shown in Fig 6.1a.

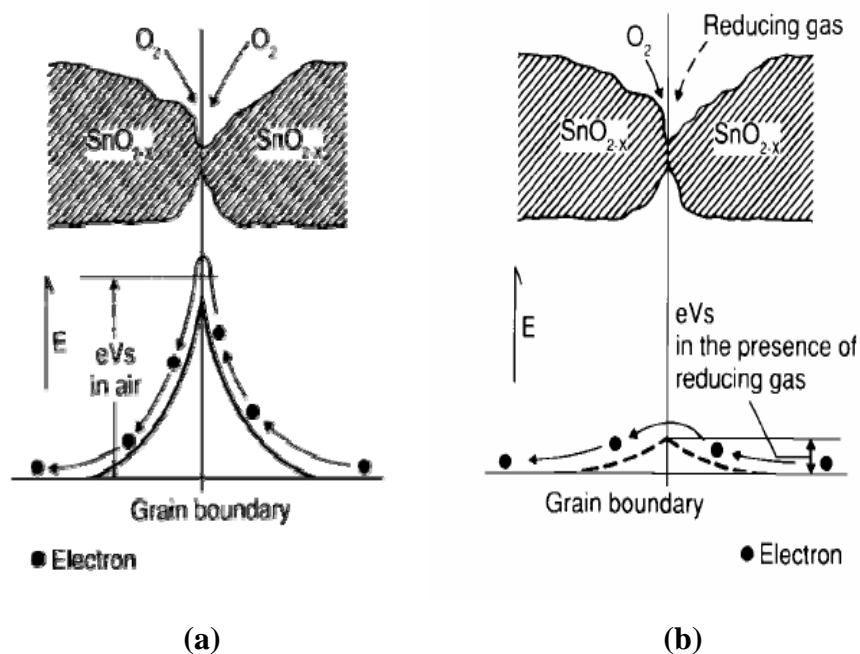


Figure 6.1: Model of inter-grain potential barrier in (a) absence and (b) presence of gases. (Fig. from >> <http://www.figarosensor.com/products/general.pdf>)

Inside the sensor, electric current flows through the conjunction parts (grain boundary) of SnO₂ micro crystals. At grain boundaries, adsorbed oxygen forms a potential barrier which prevents carriers from moving freely. The electrical resistance of the sensor is attributed to this potential barrier. In the presence of a deoxidizing gas, the surface density of the negatively charged oxygen decreases, so the barrier height in the grain boundary is reduced (See Fig. 6.1b). The reduced barrier height decreases sensor resistance. The relationship between sensor resistance and the concentration of deoxidizing gas over a certain range of gas concentration can be expressed by the following equation:

$$R_s = A[C]^{-\alpha} \quad (6.1)$$

Where R_s is electrical resistance of the sensor. A is a constant. C represents gas concentration and α is the slope of R_s curve.

6.2 Fabrication of Nanostructure Gas Sensors

6.2.1 Thermal Oxidation Technique

Thermal oxidation is a technique to produce a thin layer of oxide on the surface of a substrate. The technique forces an oxidizing agent to diffuse into the substrate at high temperature (usually between 700-1300 °C) and react with it. The rate of oxide growth is often predicted by the Deal-Grove model [70].

$$t = \frac{X_0^2}{B} + \frac{X_0}{B/A} \quad (6.2)$$

From Eq. 6.2, the time (t) requires to grow an oxide of thickness (X_0) at a constant temperature on a silicon surface. The constants A and B encapsulate the properties of the reaction and the oxide layer, respectively.

Thermal oxidation is usually performed in furnaces. A furnace typically consists of I. a cabinet, II. a heating system, III. a temperature measurement and control system, IV fused quartz process tubes where the wafers undergo oxidation, V a system for moving process gases into and out of the process tubes, and VI. a loading station used for loading (or unloading) wafers into (or from) the process tubes. The schematic diagram of thermal oxidation furnace is displayed in Fig. 6.2.

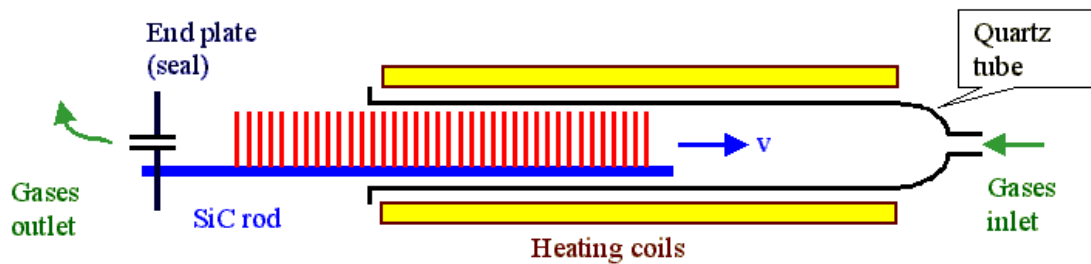


Figure 6.2: Typical thermal oxidation furnace.

(Fig. from >> http://www.tf.uni-kiel.de/matwis/amat/elmat_en/kap_6/backbone/r6_2_1.html)

6.2.2 Electron Beam Evaporation Technique

Electron beam (E-beam) evaporation process is a physical vapor deposition that yields a high deposition rate from 0.1 $\mu\text{m}/\text{min}$ to 100 $\mu\text{m}/\text{min}$ at relatively low substrate temperatures. The E-beam process offers extensive possibilities for controlling film structure and morphology with desired properties such as dense coating, high thermal efficiency, low contamination, high reliability and high productivity. The schematic diagram of E-beam evaporation system is displayed in Fig. 6.3. In E-beam evaporation system [71], the deposition chamber is evacuated to a pressure of 10^{-5} Torr or less. The material to be evaporated is in the form of ingots or compressed materials. The E-beams can be generated from electron guns by thermionic emission, field electron emission or the anodic arc method. The generated electron beam is accelerated to a high kinetic energy and focused towards the starting material. When the accelerating voltage is between 20 kV – 25 kV and the beam current is a few amperes, 85% of the kinetic energy of the electrons is converted into thermal energy as the beam bombards the surface of the starting material. The surface temperature of the starting material increases resulting in the formation of a liquid melt. The liquid material evaporates under vacuum and deposited on substrates. The deposition rate depends on starting material and E-beam power. The deposited film thickness can be measured in situ by quartz crystal monitor.

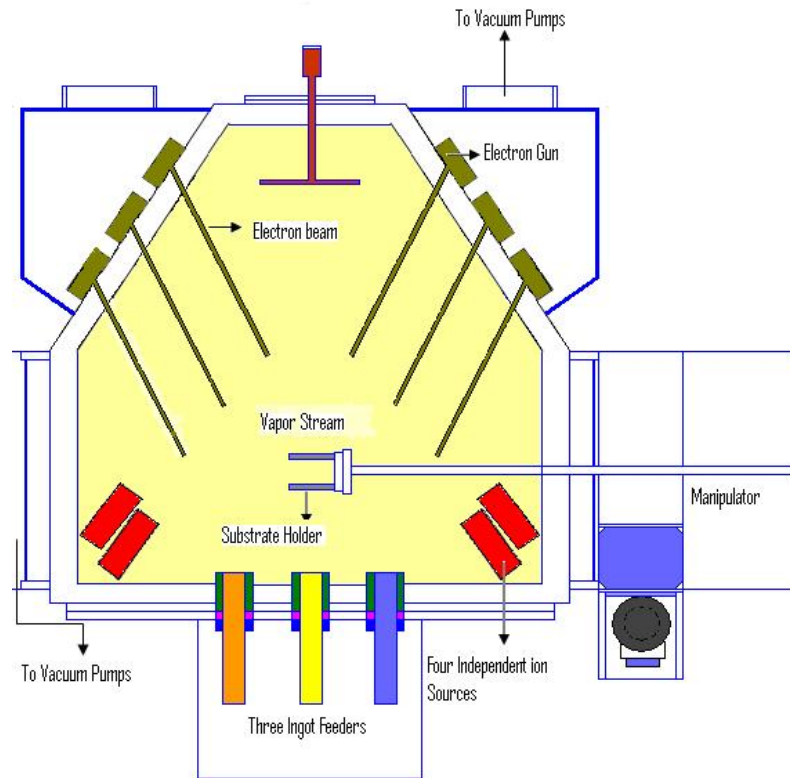


Figure 6.3: Typical electron beam vapor deposition.

(Fig. From http://en.wikipedia.org/wiki/Electron_beam_physical_vapor_deposition)

6.3 Au-doped ZnO Nanostructure Gas Sensors

6.3.1 Background

MOS such as ZnO, SnO₂ and TiO₂, are among the most popular sensing materials for gas sensors. These sensors utilize the changes of electrical conductivity upon exposing to target gases. Doping these materials with some metal catalysts can enhance sensing properties. For examples, Gong et al. [72] reported an improvement in the sensitivity and selectivity of Cu-doped ZnO to CO. Shishiyan et al. [73] demonstrated that doping ZnO with Sn can increase the sensitivity of this gas sensor to NO₂. At present, most developments of selective MOS sensors are based on the ZnO thin films doped with different impurities such as Fe, Al, MnO₂, Bi, etc. [74-78] From the authors' point of view, Au is very interesting for doping in gas sensor since it is well known to be a good catalyst when they have particle size smaller than 10 nm [79]. The Au catalysts have been shown potentials for both selective and non-selective oxidation of hydrocarbons [80-82]. In addition, it was reported that Au-

doped ZnO sensor exhibited and improvement of sensitivity toward ethanol [83,84]. In this section, fabrication and gas sensing properties of undoped and Au-doped ZnO nanostructure sensors have been reported.

6.3.2 Preparation of ZnO and Au-doped ZnO Nanostructure Sensors

Pure and Au-doped ZnO nanostructure sensors were prepared using thermal oxidation technique. The oxidation was performed by heating zinc powder (purity 99.9%) and a mixture of zinc powder and 10 wt% Au powder. Such mixtures were screened as a thick film onto an alumina substrate. The thick films were sintered at 700 °C for 24 h under oxygen atmosphere with flow rate of 500 ml/min. The ZnO nanostructures were characterized using field emission scanning electron microscopy (FESEM). The FESEM images of ZnO and 10 wt% of Au-doped ZnO nanostructure sensors on the alumina substrate are displayed in Fig. 6.4.

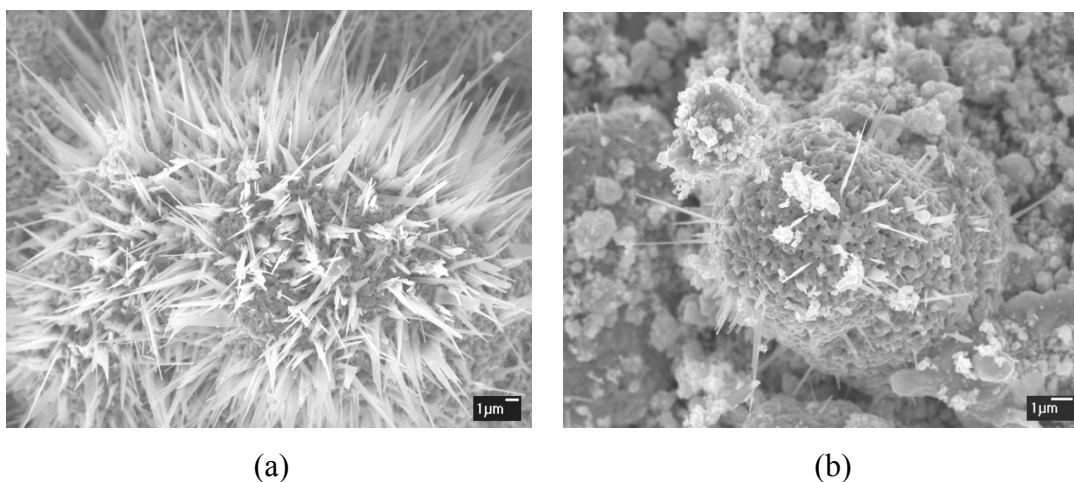


Figure 6.4: FESEM images of (a) ZnO and (b) 10 wt% Au-doped ZnO nanostructure.

The wire-like or belt-like nanostructures outward from microparticle are observed. The diameter and length of ZnO nanostructures are within the range of 250–750 nm and 1.7–7.0 μm respectively. The sensors were simply fabricated by putting gold contact and heating coil underneath alumina substrate. The successfully produced ZnO and Au-doped ZnO nanostructure sensors are displayed in Fig. 6.5.

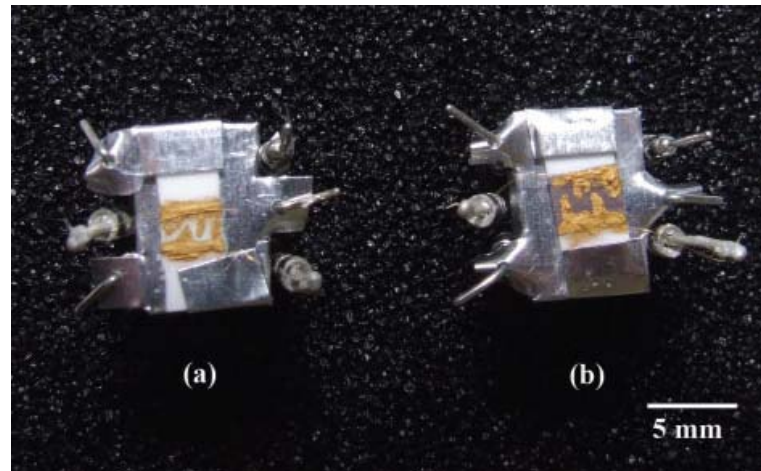


Figure 6.5: Produced (a) ZnO and (b) 10 wt% Au-doped ZnO nanostructure sensors.

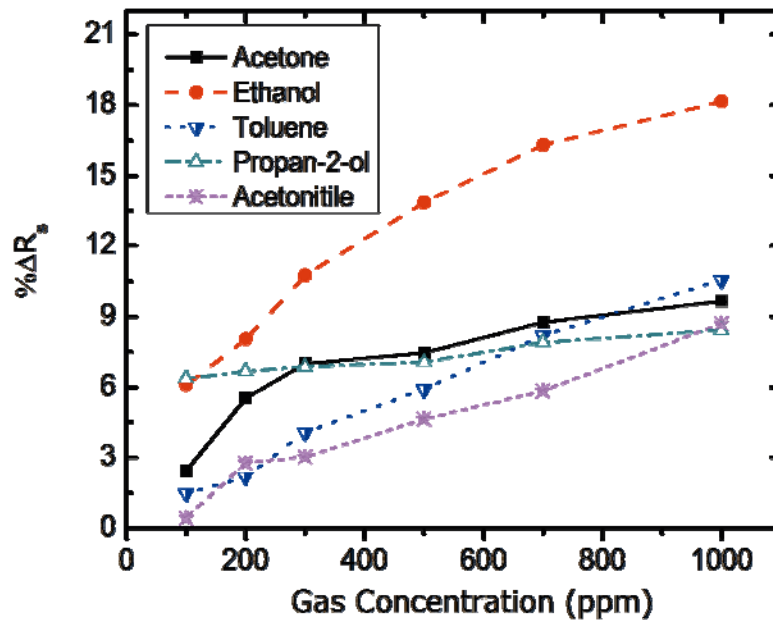
6.3.3 Sensor Responses on Volatile Organic Compounds

To compare sensitivity of two sensors on different volatile organic compounds (VOCs), it is better to calculate the percentage change of resistance ($\% \Delta R_s$) via

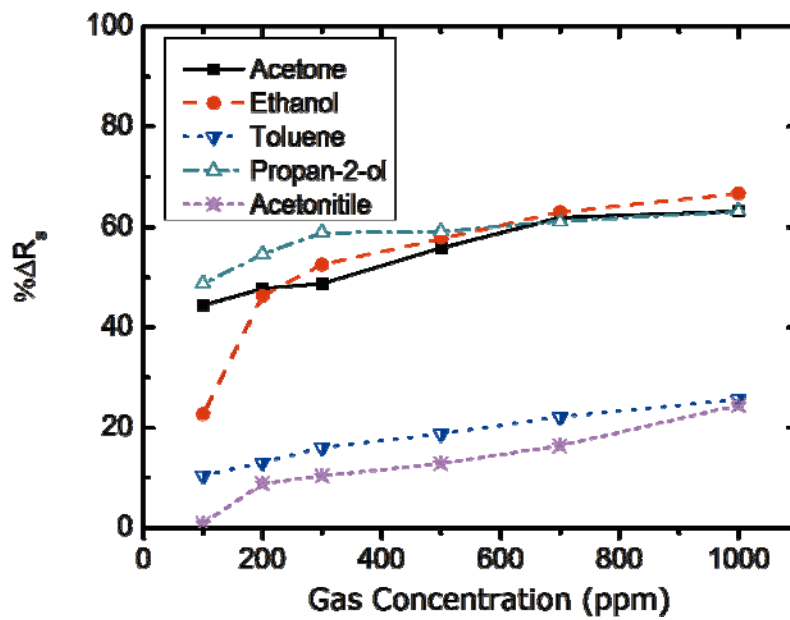
$$\% \Delta R_s = \left| \frac{\bar{R}_{sam} - \bar{R}_o}{\bar{R}_o} \right| \times 100 \quad (6.3)$$

Where \bar{R}_{sam} and \bar{R}_o are the mean sensor resistance in the presence and the absence of the testing gas, respectively.

Fig. 6.6 shows the sensor responses of pure and Au-doped ZnO to acetone, ethanol, toluene, propan-2-ol, acetonitrile. From Fig. 6.6, it indicates that the sensor responses of both sensors work linearly with gas concentration. At the same concentration, the sensor response of Au-doped ZnO sensor on all VOCs is higher than that of ZnO sensor. The Au in ZnO enhances the adsorption reaction between the VOCs and the adsorbed oxygen ion on the crystal surface with a negative charge. The species of oxygen ion previously determined to be O^{2-} [85]. At the grain boundaries, the surface density of the negatively charged oxygen decreases immediately and abundantly. Therefore, the changing of resistance of Au-doped ZnO sensor is much more than that of ZnO sensor. Moreover, such ZnO nanosensor shows the strong response on ethanol. Therefore, it is suitable to employ in detecting alcoholic solution and beverages.



(a)



(b)

Figure 6.6: The sensor response of (a) ZnO and (b) 10 wt% of Au-doped ZnO sensors to concentrations of VOCs.

6.4 Carbon Nanotube-doped SnO₂ Gas Sensors

6.4.1 Background

From session above, doping has long been used as a traditional mean to obtain new MOS gas sensors that exhibit gas-sensing properties differentiated from the original ones. Recently, carbon nanotube (CNT) have become as potential dopant, due to its special electronic properties and high specific surface area that can boost catalytic reactions occurring at the metal oxide surface. The hybrid CNT–SnO₂ gas sensors prepared by different techniques have been reported to have excellent responses to NO₂ [86,87], CO [87], NH₃[88], H₂ [89], CHOH [90] and indoor air pollutants [91]. Among such techniques, co-evaporation of SnO₂/CNT is a relatively new concept to form hybrid CNT–SnO₂ gas sensors [92,93]. It offers extensive possibilities for controlling the film structure and morphology with high deposition rates, low contamination, high reliability and high productivity. However, there have been very few reports on CNT–SnO₂ gas sensors prepared by this technique. In this section, fabrication based on prepared by electron beam (E-beam) evaporation and sensing mechanism of hybridized CNT–SnO₂ gas sensors have been reported.

6.4.2 Fabrication of Gas Sensors

The gas sensors were fabricated by E-beam evaporation. Top and cross-sectional views of sensor structure are shown in Fig. 6.7a and b, respectively.

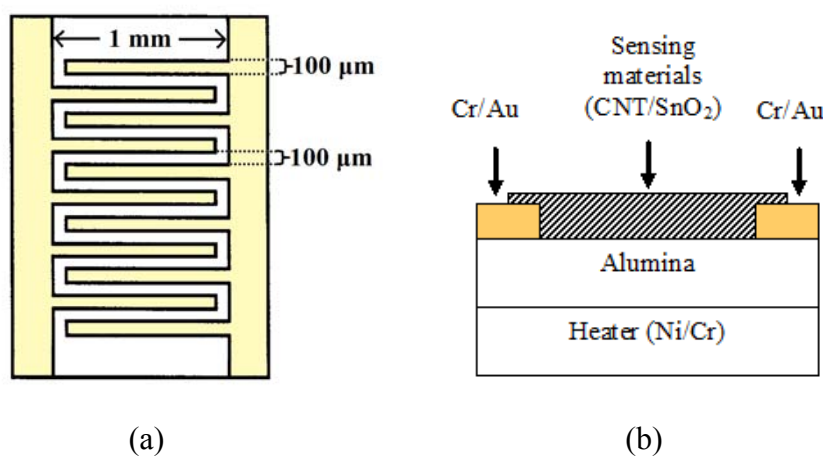


Figure 6.7: Structure of the gas sensor; (a) top view of interdigitated electrode, (b) cross-sectional view.

First, Cr/Au interdigitated electrodes on alumina substrates were prepared. Prior to deposition of the electrodes, the substrates were cleaned by oxygen-ion bombardment under a vacuum pressure of $\sim 10^{-4}$ Torr in order to improve the adhesion of the film to the substrates. Cr and Au layers were then successively E-beam evaporated over the alumina substrates through electroplated-Ni shadow masks. These shadow masks were fabricated by means of standard photolithography and electroplating of Ni. The masks were employed by attaching them to the substrates using strong magnets. The resulted thickness of Cr and Au layers were ~ 50 nm and ~ 200 nm, respectively. The width, spacing, and length of the interdigitated electrodes are approximately $100 \mu\text{m}$, $100 \mu\text{m}$, and 1mm , respectively.

Multi-walled CNT powder was synthesized by thermal chemical vapor deposition (CVD) in a lab-made horizontal tube furnace. Iron catalyst powder was loaded in the tube furnace and heated up until the growth temperature of 700°C was reached. The system was then maintained under the hydrogen gas flow of 1.5 l/min at the atmospheric pressure. Next, acetylene gas was introduced into the system for 2 h for CNT synthesis. The flow ratio between acetylene and hydrogen was approximately $1:4$. The remaining catalysts were removed from CNTs by chemical oxidation in 4M nitric acid at room temperature for 4 h . Then, CNTs were rinsed with DI water and dehydrated at 150°C for 2 h [94]. Transmission electron microscope (TEM) images of the CNT before and after chemical oxidation treatments are shown in Fig. 6.8a and b, respectively. It is evident that the iron catalysts were effectively removed and the number of CNT walls was reduced. CNT-SnO₂ mixed powders were prepared with 0.5 wt\% and 1 wt\% concentrations by mixing 15 g of SnO₂ powder with 0.075 g and 0.15 g of CNT powders, respectively. The mixed powders were thoroughly mixed by grinding in a mortar for 30 min . The pure SnO₂ and mixed powders were compressed into cylindrical pellets in a hard steel mold by a hydraulic compressor at a pressure of 15 tons . Next, the compressed SnO₂ and mixed CNT-SnO₂ materials (0.5 wt\% and 1 wt\% CNTs) were loaded in E-beam chamber and evaporated over the interdigitated electrodes through an electroplated shadow mask with square window pattern that aligned to the interdigitated area at an operating vacuum of $\sim 10^{-5}$ Torr. The evaporation condition was based on the previous studies

by Wisitsoraat et al. [92,93]. The film thickness of sensing materials is $\sim 300\text{nm}$ as measured in situ by quartz crystal monitor. The evaporated film was then annealed at $500\text{ }^{\circ}\text{C}$ for 3 h. Finally, a NiCr (Ni 80% and Cr 20%) layer was also E-beam evaporated over the backside of substrate to perform as a heating unit. The NiCr heater can perform heating up to $350\text{ }^{\circ}\text{C}$. A photograph of fabricated sensor is shown in Fig. 6.9.

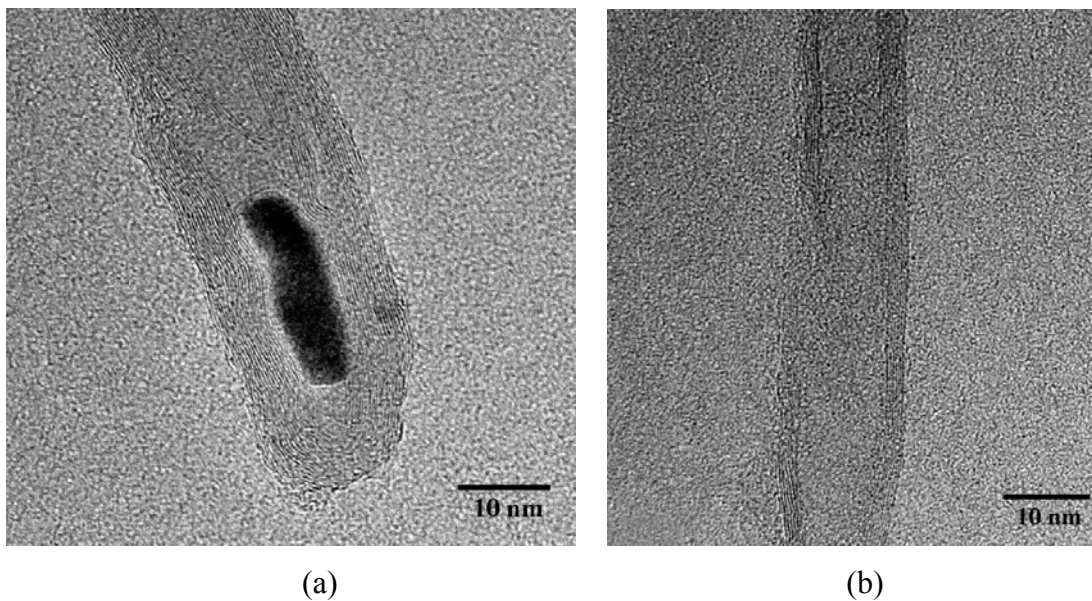


Figure 6.8: Typical TEM images of multi-walled CNT (a) before and (b) after purification.

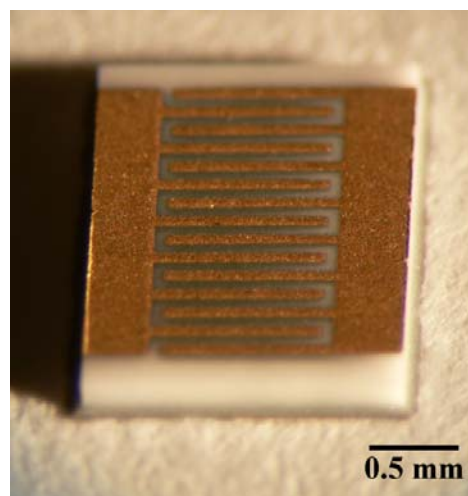


Figure 6.9: Photograph of the fabricated sensor.

6.4.3 Characterization of Gas-sensing Films

Fig. 6.10a–c illustrates morphology of the sensing films by scanning electron microscopy (SEM), showing the presence of metal oxide grains.

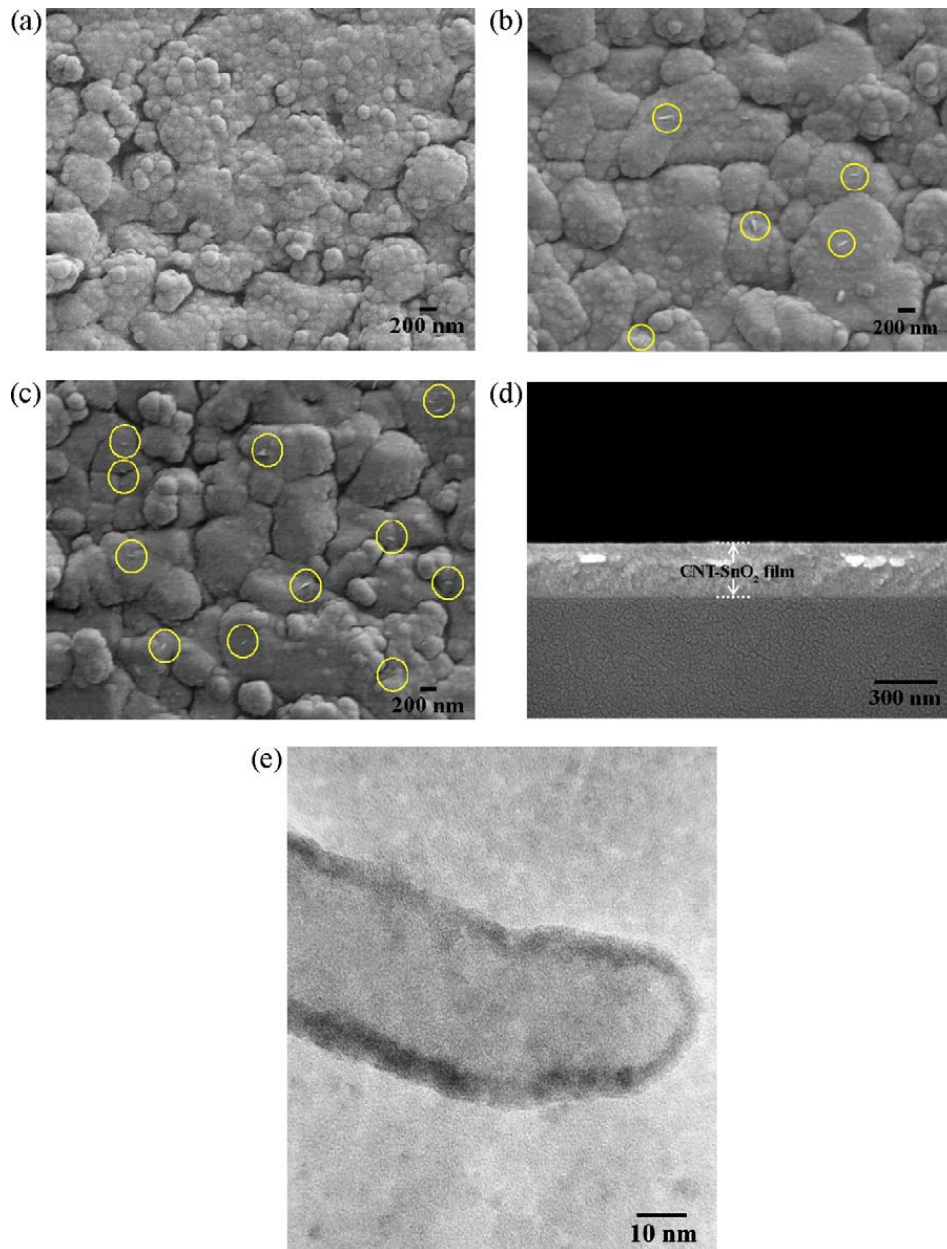


Figure 6.10: SEM images of sensing films; (a) undoped SnO₂ film, (b) 0.5 wt% CNT-SnO₂ film and (c) 1wt% CNT-SnO₂ film. The yellow circles in (b) and (c) indicate CNT fragments, (d) typical cross-sectional SEM image of CNT-SnO₂ film and (e) typical HRTEM image of CNT-SnO₂ film.

Spherical SnO₂ particles are clearly observed in the undoped tin oxide film (see Fig. 6.10a). In the CNT-doped SnO₂ films, such spherical particles are smoothed out and smaller SnO₂ grain sizes are observed. In addition, the CNTs are well embedded and randomly arranged inside the SnO₂ film as circled in Fig. 6.10b and c. It can be seen that although the distributions of CNTs in the films are quite random, the densities of the observed CNTs are proportional to the concentration of CNTs in the initial mixed powders. Therefore, the amount of CNTs in the film can be well controlled by varying the percentage of CNTs in the initial mixed powder.

Typical cross-sectional SEM image of CNT-doped SnO₂ film is shown in Fig. 6.10d. It indicates that the film thickness is about 270 nm, slightly lower than the expected value of 300 nm. The small discrepancy should be due to some calibration inaccuracies of quartz crystal monitor. The detailed structure of CNT–SnO₂ composite was characterized by high-resolution TEM (HRTEM). The samples were prepared by E-beam evaporation of SnO₂/CNT onto carbon coated copper TEM grid, which was done at the same time as coating on interdigitated electrodes. A typical HRTEM image of CNT–SnO₂ composite is shown in Fig. 6.10e. From the HRTEM image, it can be identified that a single multi-walled CNT fragment is indeed embedded in the nanocrystalline SnO₂ layer. The diameter of CNTs and the crystal size of SnO₂ were estimated to be in the range of ~20–40nm and 3–10 nm, respectively. Comparing to the TEM image of pure CNT (Fig. 6.8b), the nanotube walls cannot be resolved due to the presence of SnO₂ nanocrystalline thin film surrounding the surface of CNT.

A plausible mechanism for CNT–SnO₂ co-evaporation can be drawn as follows. When SnO₂ was evaporated at temperature of ~1500 °C in a vacuum of ~10⁻⁵ Torr, CNTs fragments that are small and very light, were carried into the vapor by surrounding SnO₂ molecules. It should be noted that CNTs themselves were not decomposed during evaporation because this temperature is well below CNTs' sublimation point (>3000 °C) in a high vacuum condition. Thus, these results prove our new concept that CNTs can be co-evaporated with SnO₂ material with no significant decomposition at the evaporation temperature of ~1500 °C. In addition, CNTs can endure treatment of high-energy electron beams (~7.67 kV) in a

high vacuum of 10^{-5} Torr. When CNT molecular fragments arrived at the substrate that was held at $130\text{ }^{\circ}\text{C}$, SnO_2 vapor was condensed and coated around them. As the substrate was cooled down, CNTs remained in the lattice of SnO_2 due to physicochemical binding between SnO_2 and CNTs. This result is evident as seen in the TEM and SEM images. The fact that there should be physical binding between SnO_2 and CNTs can also be inferred from other reports that demonstrate SnO_2 coating around CNTs [86–91].

6.4.4 Sensor Responses

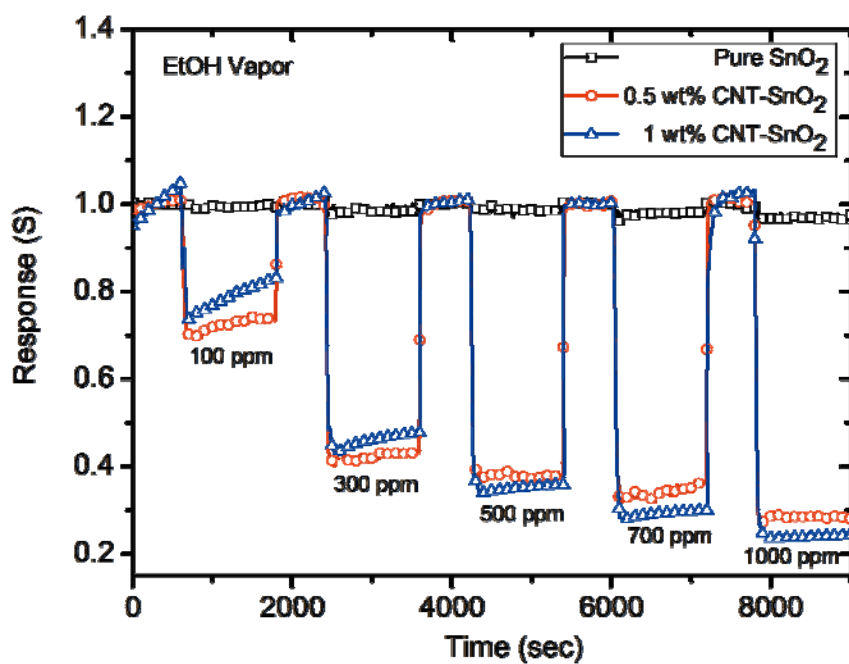
The produced sensors were placed in a desiccator that served as a gas sensitivity test chamber. The total volume of the chamber is 22.35 l. Gas response (S) is calculated as follows:

$$S = \frac{R_{\text{gas}}}{R_{\text{air}}} \quad (6.4)$$

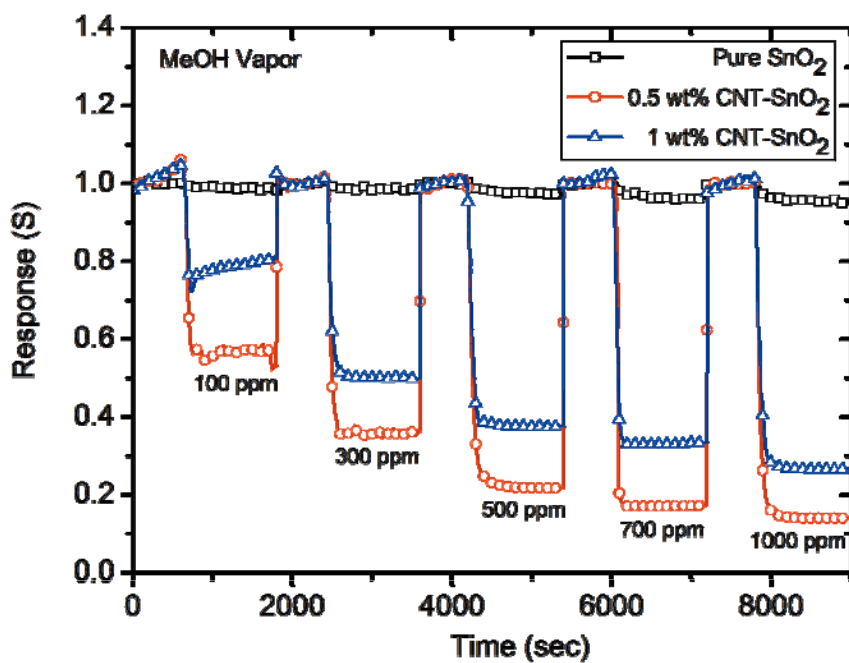
where R_{air} and R_{gas} are the resistances of the sensor in air and in the presence of desired gas, respectively.

The undoped SnO_2 sensor, 0.5 wt% CNT– SnO_2 sensor and 1 wt% CNT– SnO_2 sensor show response to ethanol (EtOH) and methanol (MeOH) as shown in Fig. 6.11a and b, respectively. It should be noted that the selected film thickness of 300 nm is an optimized value for electrical conductivity and sensitivity. It was found from our study that sensors with thickness of less than 200 nm and more than 400 nm will have too low and too high electrical conductivity, respectively. In addition, the gas-sensing response is increased as thickness increases from 50 nm to 200 nm and the response becomes quite independent of thickness as the thickness increases from 200 nm to 400 nm and begins to slowly decrease as the thickness increases further. In addition, a variation of less than 30% was found among ten tested sensors and the sensors have a long term drift of less than 20% over 6 months of operation. Thus, the fabricated sensors have reasonably good reproducibility and stability.

From Fig. 6.11, it can be seen that these materials behave as n-type semiconductors since their resistance decreases in the presence of a deoxidizing gas, whereas MWCNT– SnO_2 film prepared by spin coating technique behave as p-type semiconductors [88].



(a)



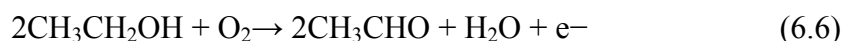
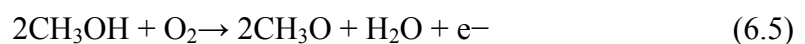
(b)

Figure 6.11: Sensor responses of undoped SnO_2 sensor, 0.5 wt% CNT- SnO_2 sensor and 1 wt% CNT- SnO_2 sensor to different concentrations of (a) EtOH and (b) MeOH.

Under the operating temperature range ~250–300 °C, CNT doping can improve the response of gas sensor on EtOH and MeOH compared with the pure SnO₂ sensor. The response of native SnO₂ sensor is lower than 2% while CNT-doped SnO₂ sensors give the response higher than 65% at concentration 1000 ppm under such temperature range. The amount of CNT doping exhibits different change in response to EtOH and MeOH vapors. Hence, the 0.5 wt% and 1 wt% of CNTs show highest response toward MeOH and EtOH, respectively. These results confirm that varying of CNT concentration can be used to tune sensitivity and selectivity of SnO₂ sensor to a desired gas. In this case, the modified gas sensors can be employed to target MeOH vapor in the MeOH/EtOH mixture. Nevertheless, if CNT amount exceed, the gas sensitivity will be reduced because the CNTs begin to connect together and result in shorter resistance path [92].

6.4.5 Sensing Mechanism of CNT–SnO₂ Gas Sensors

From the gas-sensing data, small percentage of CNT doping significantly enhances the sensing of MeOH and EtOH. The results are consistent with other reports based on CNT–SnO₂ composites [86–92]. In these reports, various explanations for gas-sensing enhancement by CNTs have been proposed, for examples, amplification effect of the PN junction structure between n-SnO₂ and p-SWCNT [86], the oriented growth of SnO₂ along the CNTs during heat treatment and its consequent enhancement of the local electric field favorable for the gas-sensing reaction [91] and increased surface area due to the formation of CNT protrusions [92]. The PN junction structure between SnO₂ and SWCNT is not applied in the present case because MWCNTs are used. In this work, we propose that the observed enhancement effect is attributed to the nanochannels formed by MWCNTs embedded in SnO₂. The formation of the nanochannels in SnO₂ surface can increase the diffusion of the gas molecules into the metal oxide surface as well as enhance local electric field at CNT–SnO₂ interface. This can considerably enhance dehydrogenation reactions of MeOH and EtOH as described by [95]:



Since the effect of CNTs on gas sensing is primarily on the surface, the gas-sensing response is not significantly dependent on the thickness when the thickness is sufficiently large. This is in accordance with our observations. Increasing surface area due to CNTs intrusion and observed smaller grain size due to CNTs doping can partly contribute to enhancing gas reaction. However, the contribution from these effects is relatively small because CNT concentration is so low that the specific surface area is only slightly affected by CNTs inclusion.

6.5 Conclusion

In this chapter, fabrications, sensing properties and sensing mechanism of nanostructure gas sensors including ZnO, Au-doped ZnO, SnO₂ and CNT-doped SnO₂ prepared by using both thermal oxidation and E-beam evaporation techniques have been reported. In case of Au-doped ZnO gas sensors, the results show that doping 10 wt% Au could improve the sensitivity of gas sensors on VOCs. The responses of the sensors are linear with gas concentrations varying from 100 to 1000 ppm. Therefore, it can be used for predicting the gas concentrations of unknown VOCs. In case of CNT-doped SnO₂, the doping of CNTs could enhance the sensitivity of SnO₂ sensor while their concentration plays an important role in selectivity to VOCs such as EtOH and MeOH.

CHAPTER VII

HYDROGEN GAS SENSOR

7.1 Introduction

Hydrogen (H_2) is one of the most useful gases, being used in many chemical processes and various industries including aerospace, medical, petrochemical, transportation, and energy [96-98]. In recent years, H_2 has attracted a great deal of attention as a potential clean energy source for the next generation of automobiles and household appliances due to its perfectly clean combustion without any release of pollutants or greenhouse gases [99]. However, this low molecular weighted gas can easily leak out and may cause fires or explosions when its concentration in air is between 4% and 75% by volume [100]. Moreover, H_2 is a colorless, odorless and tasteless gas that cannot be detected by human senses. Therefore, it is very essential to develop the effective H_2 gas sensors for monitoring of H_2 leaks.

Tungsten Oxide (WO_3) is one of the most widely studied gas-sensing materials due to its fast, high sensitivity response toward NO_x [101-104], H_2S [105-108], C_2H_5OH [108,109] CO [110], NH_3 [110-114] and O_3 [115]. In case of H_2 detection, it is well known that H_2 molecules are not activated on the smooth WO_3 surface of single crystals [116]. Addition of some noble metals such as Pt, Pd, or Au [117-121] to WO_3 usually improves the sensitivity and selectivity to H_2 gas. These metal doped WO_3 films can be prepared by several methods, including screen printing [117], sputtering [118,119] and sol-gel process [120,121].

In the chapter, multi-walled carbon nanotube (MWCNT)-doped WO_3 thin films fabricated by an electron beam (E-beam) evaporation process and their application for H_2 gas sensing are reported for the first time. The E-beam process offers extensive possibilities for controlling film structure and morphology with desired properties such as dense coating, high thermal efficiency, low contamination

high reliability and high productivity. MWCNTs were selected for doping because of their larger effective surface area, with many sites available to adsorb gas molecules, and their hollow geometry that may be helpful to enhance the sensitivity and reduce the operating temperature. Furthermore, MWCNTs were reported to be sensitive to H_2 , with good recovery times [122].

7.2 Experimental

7.2.1 Preparation of Materials

Commercial WO_3 powder was obtained from Merck and used without further purification. MWCNTs were grown by the thermal chemical vapor deposition (CVD) process. The catalyst layer of aluminium oxide (10 nm) and stainless steel (5 nm) was deposited on the silicon (100) substrates (Semiconductor Wafer Inc.) using reactive sputtering apparatus. The synthesis of MWCNTs was performed under a flow of acetylene/hydrogen at a ratio of 3.6:1 at 700 °C for 3 min. To obtain high purity MWCNTs, the water-assisted selective etching technique [123] was applied after each CNT's growth stage. Water vapor (300 ppm) was introduced into the system by bubbling argon gas through liquid water at room temperature for 3 min. The sequence of acetylene/hydrogen and water vapor flows was repeated for five cycles. Based on the scanning electron microscopic (SEM) image, as shown in Fig. 7.1, the diameter and length of the MWCNTs are ~35 nm and ~26 μm , respectively.

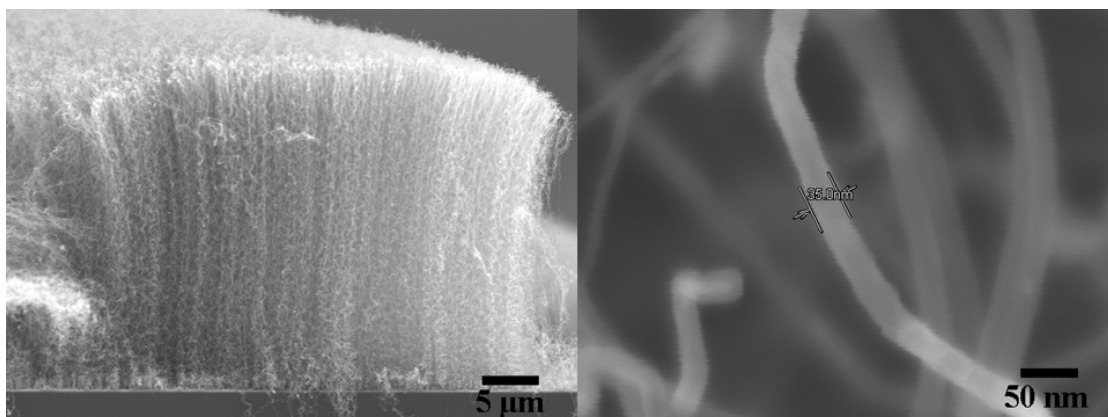


Figure 7.1: SEM images of the produced MWCNTs grown by the CVD process.

The electrical conductivity of MWCNTs was ~ 75 S/cm, as measured by a four-point probe method at room temperature. In addition, high-resolution transmission electron microscopic (HR-TEM) imaging, as shown in Fig. 7.2, confirms that CNTs are multi-walled, with the width and number of walls being ~ 4.6 nm and 14, respectively. Thus, the spacing between two graphitic layers is ~ 0.33 nm, which is in good agreement with theoretical and experimental values.

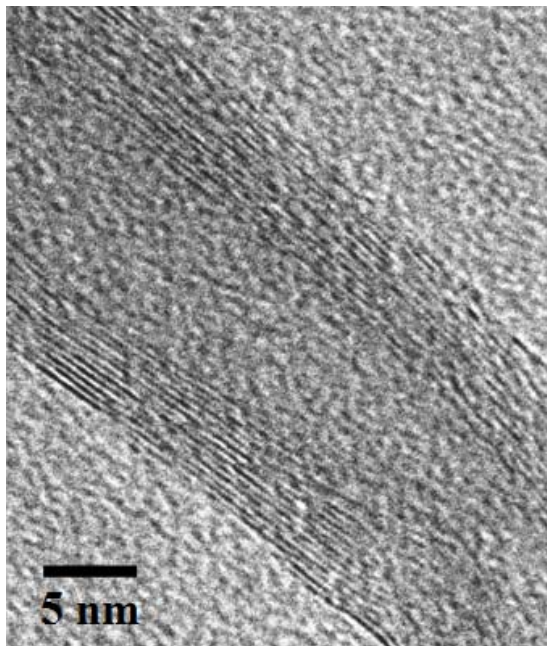


Figure 7.2: High resolution TEM image of the produced MWCNT grown by the CVD process.

7.2.2 Fabrication of MWCNTs-doped WO_3 Thin Film

MWCNT-doped WO_3 thin film was fabricated by the E-beam evaporation technique onto Cr/Au interdigitated electrodes on an alumina substrate [124]. The target was prepared by mixing 99 wt% of WO_3 powder with 1 wt% of MWCNT powder using a grinder in a mortar for 30 min and then pelletizing with a hydraulic compressor. Deposition was performed at a pressure of 5×10^{-6} Torr in the evaporation chamber. The substrate was rotated and kept at 130°C during the deposition in order to obtain a homogeneous thin film. The deposition rate was $2 \text{ \AA}/\text{sec}$ and the final film thickness was 150 nm, as controlled by a quartz crystal monitor. After E-beam

evaporation, the film was annealed at 500 °C for 3 h in air to stabilize the crystalline structure. In addition, an undoped WO₃ thin film was also fabricated using the same conditions for comparison.

7.2.3 Measurement of Gas Sensing

To evaluate the gas sensing properties of the thus prepared thin films, MWCNT-doped WO₃ and undoped WO₃ gas sensors were placed inside a stainless steel chamber and the resistance measured using a 8846A Fluke multimeter with 6.5 digit resolution. The gas sensing measurements were made within a dynamic flow system with control of sensor operating temperatures (200–400 °C) under variable gas concentrations (100–50,000 ppm). Hydrogen (H₂), ethanol (C₂H₅OH), methane (CH₄), acetylene (C₂H₂), and ethylene (C₂H₄) were used to test the sensing properties and selectivity of the thin films. The sample gas flow time and the clean air reference flow time were fixed at 5 min and 15 min, respectively. It should be noted that these switching interval was selected so that the resistance change is at least 90% of the saturated value. The sensor resistances were sampled and recorded every second using LabVIEW with a USB DAQ device for subsequent analyses.

7.3 Characterization of Thin Films

Surface morphology, particle size and crystalline structure of the films were characterized by SEM and TEM. Figure 7.3 shows the SEM surface morphology of MWCNT-doped WO₃ thin film deposited on an alumina substrate. It was seen that the film coated on the rough alumina substrate has approximate grain sizes ranging from 40 to 80 nm. The nanometer grain size together with the roughness of the alumina substrate can enhance the gas sensitivity of thin films [125,126] because more gas adsorption sites are available due to the increased surface area and porosity. With the SEM resolution, CNT structure cannot be observed on the thin film surface. Therefore, TEM characterization was used to confirm CNT inclusion into the WO₃ film. It should be noted that copper TEM grid samples were loaded inside the evaporation chamber for sample deposition at the same time as coating on the Cr/Au interdigitated electrodes. TEM observation clearly shows CNT inclusion into the

nanocrystalline WO_3 , while the electron diffraction pattern exhibits polycrystalline phase in the film, as shown in Figure 7.4a and b, respectively.

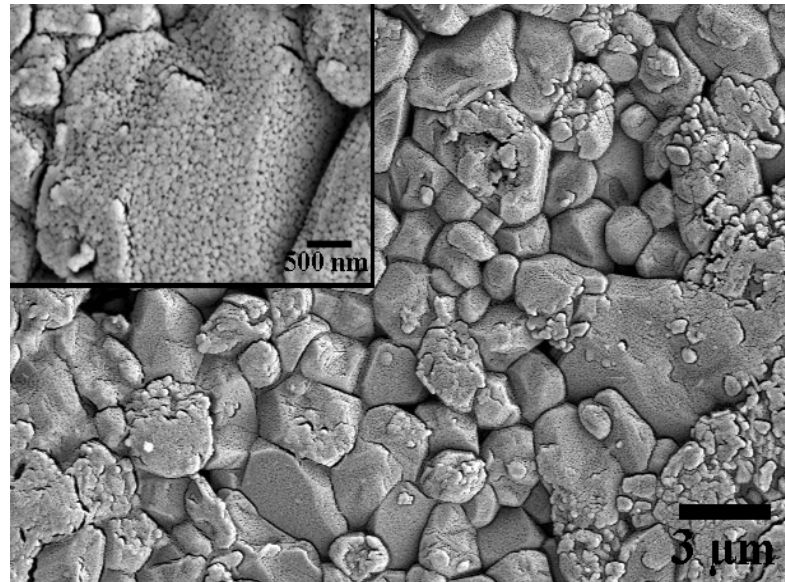


Figure 7.3: SEM image of MWCNT-doped WO_3 thin films on alumina substrate.

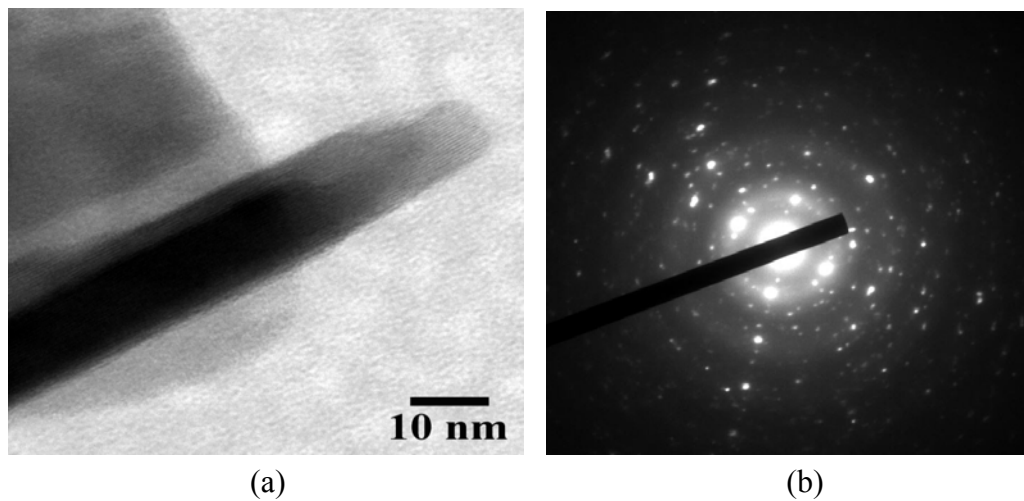


Figure 7.4: (a) High-resolution TEM image and (b) corresponding selected area diffraction pattern of MWCNT-doped WO_3 thin film.

The film morphology obtained in our study is in accordance with observations on nanocrystalline WO_3 films grown by other methods [127,128].

Doping of CNT does not change the phase or surface morphology of the film, but it may help form nanochannels in WO₃ films, leading to the enhancement of the sensitivity and reduction of the operating temperature.

7.4 Sensing Properties of Thin Films

The sensor response (S) of the thin films is defined as the percentage of resistance change:

$$S(\%) = \left(\frac{R_0 - R}{R_0} \right) \times 100 \quad (7.1)$$

where R₀ and R are the resistance of the thin films in pure air and test gas, respectively. Fig. 7.5 shows the response of the undoped WO₃ and MWCNT-doped WO₃ thin films to 1,000 ppm H₂ at varying operating temperatures.

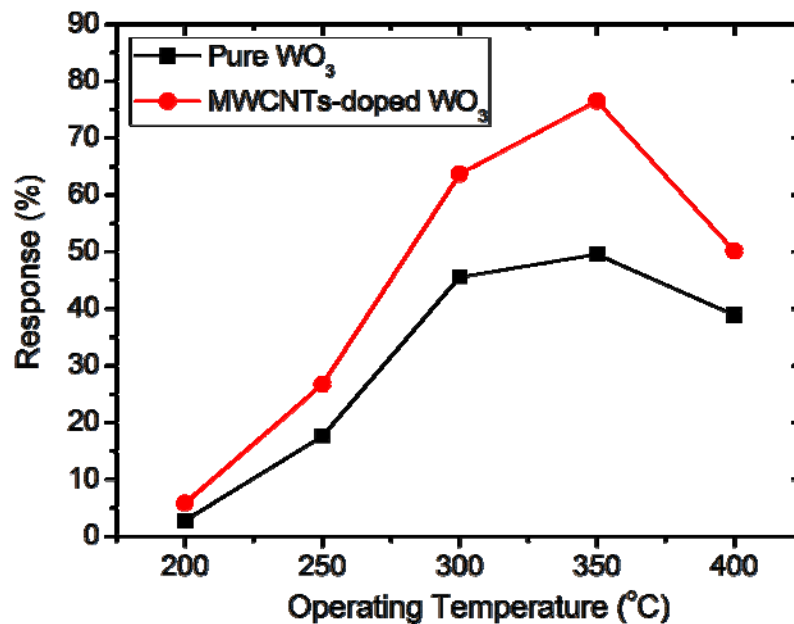


Figure 7.5: Sensing response to H₂ (1,000 ppm) at different operating temperatures.

It can be seen that the response of the films increases as the operating temperature increases up to 350 °C, and then decreases. The gas-sensing response increases with temperature in the 200–350 °C range because thermal energy helps the reactions involved overcome their respective activation energy barriers [129,130].

However, if the operating temperature becomes too high (i.e., $>350\text{ }^{\circ}\text{C}$), the adsorbed oxygen species at the sensing sites on the film surface will be diminished and less available to react with H_2 molecules [131], thereby limiting the film's response. At any operating temperature, the sensor response of the MWCNT-doped WO_3 thin film is higher than that of the undoped WO_3 thin film. Specifically, at the optimum operating temperature ($350\text{ }^{\circ}\text{C}$), MWCNT-doped WO_3 thin film yields a 26.9 % higher response than the undoped one. The doped sensor prepared in this work also shows higher response than the WO_3 films prepared by the sol-gel process [120].

One major advantage of MWCNT-doped WO_3 thin film is that the sensor can be operated at a lower operating temperature ($250\text{ }^{\circ}\text{C}$), especially if this sensor is used to measure the H_2 gas at higher concentrations (5,000–50,000 ppm). As shown in Fig. 7.6, at such a concentration range, there are sufficient numbers of H_2 molecules available to react with the surface oxygen adsorption sites. It is also well-known that MWCNTs contribute to the reduction of sensor resistance of metal oxides [132] and the activation energy between the WO_3 surface and H_2 gas. The details of the sensing mechanisms of MWCNT-doped WO_3 thin films will be discussed in the next section.

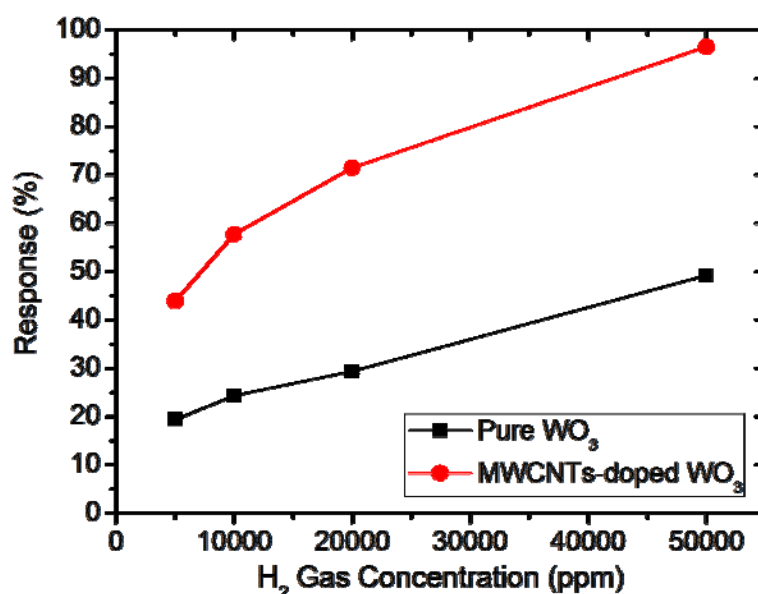


Figure 7.6: Sensing response of the undoped WO_3 and MWCNT-doped WO_3 thin films to high H_2 concentrations (5,000–50,000 ppm) at the operating temperature of $250\text{ }^{\circ}\text{C}$.

To demonstrate the selectivity of the MWCNT-doped WO_3 thin film, its sensing response (at the operating temperature of $350\text{ }^\circ\text{C}$) to various gas vapors, namely H_2 , $\text{C}_2\text{H}_5\text{OH}$, CH_4 , and C_2H_2 , was measured and plotted (Fig. 7.7). It can be seen that MWCNT-doped WO_3 thin film exhibits a strong response to H_2 , and much weaker responses to $\text{C}_2\text{H}_5\text{OH}$, CH_4 , and C_2H_2 . In particular, this thin film was found to be insensitive to C_2H_4 at the optimum operating temperature of $350\text{ }^\circ\text{C}$. It is therefore concluded that the MWCNT-doped WO_3 thin film exhibits high selectivity to H_2 .

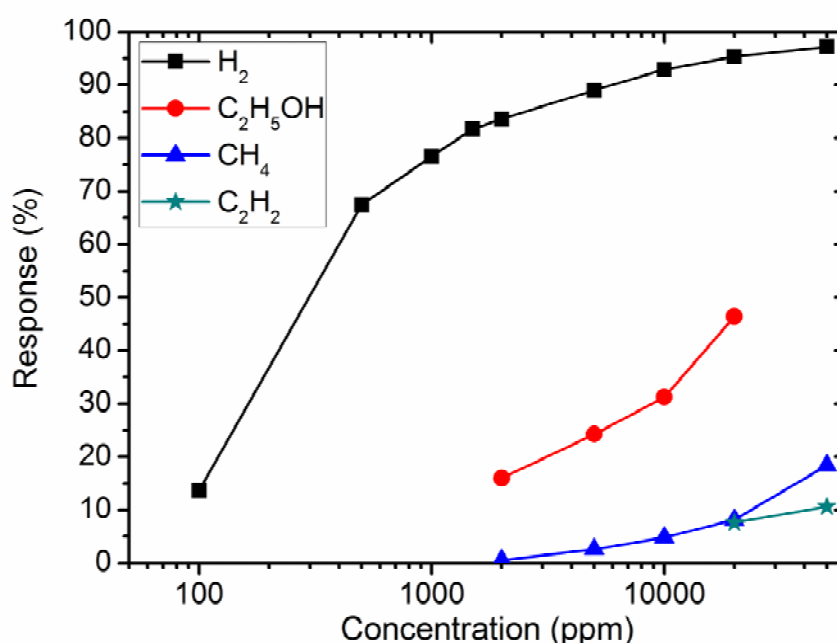


Figure 7.7: Sensing response of MWCNT-doped WO_3 thin film at the operating temperature of $350\text{ }^\circ\text{C}$ to various concentrations of different gas vapors.

7.5 Sensing Mechanism of MWCNTs-doped WO_3 Thin Film

It is well known that WO_3 is an n-type semiconductor while CNT is a p-type semiconductor. MWCNT-doped WO_3 thin film can be either p-type or n-type semiconductors depending on the quantity of MWCNTs and the operating temperature [133]. In this work, the produced MWCNTs-doped WO_3 thin film

behaves as an n-type semiconductor since the electrical conductivity of the film increases when reducing gases, i.e. H₂, are absorbed by its surface. Doping of MWCNTs into the WO₃ matrix can introduce nanochannels and form p-n heterojunctions in the thin film. These nanochannels play an important role for gas diffusion. The gas molecules can easily transport into the gas-sensing layers leading to increasing sensitivity [134,135]. In addition, MWCNT-doped WO₃ thin film p-n heterojunctions could be formed at the interface between WO₃ and the MWCNTs [133,136]. When H₂ gas is exposed to MWCNT-doped WO₃ thin film, the widths of the depletion layers at the p-n heterojunctions can be modulated. The potential barriers at the interfaces or inside the WO₃ may be changed. This change of the depletion layer in the p-n heterojunctions of MWCNT-doped WO₃ thin film may explain the enhanced response of the film at low operating temperatures. Various oxygen species chemisorbed at the thin film surface such as O²⁻, O₂⁻, and O⁻ are available for catalytic reactions with H₂, thus depending on the temperature at the metal oxide surface [137]. At the operating temperature range of 200–400 °C, O⁻ is commonly chemisorbed. Consequently, the chemical reaction underlying the H₂ gas sensing in this study is given by [138]:



The adsorbed O⁻ on the thin film surface reacts with the H₂ gas yielding H₂O and releasing electrons which contribute to the current increase through the thin film that causes the electrical conductivity to increase.

7.6 Conclusion

MWCNT-doped WO₃ thin film was successfully prepared by the E-beam evaporation technique. The 1 wt% MWCNT-doped WO₃ thin film exhibits n-type semiconductor behavior of the polycrystalline phase. Doping with MWCNTs does not significantly change any phase or surface morphology of the film, but it introduces nanochannels and form p-n heterojunctions in the WO₃ matrix. The MWCNT-doped WO₃ thin film exhibits high selectivity and sensitivity to H₂ over a relatively wide range of concentrations (100-50,000 ppm). Moreover, it can operate at a relatively low temperature. This should be useful for developing high performance H₂ gas

sensors. To our best knowledge, this is the first report on MWCNT-doped WO_3 hydrogen sensors prepared by the E-beam method.

CHAPTER VIII ELECTRONIC NOSE

8.1 Introduction of Electronic Nose

An electronic nose (E-nose) refers to an instrument which comprises an array of electronic chemical sensors with partial specificity and an appropriate pattern recognition system, capable of recognizing simple or complex odours [139]. The E-nose was developed in order to mimic human olfaction that functions as a non-separative mechanism. Analogy between the biological nose and E-nose [140] is demonstrated in Fig. 8.1.

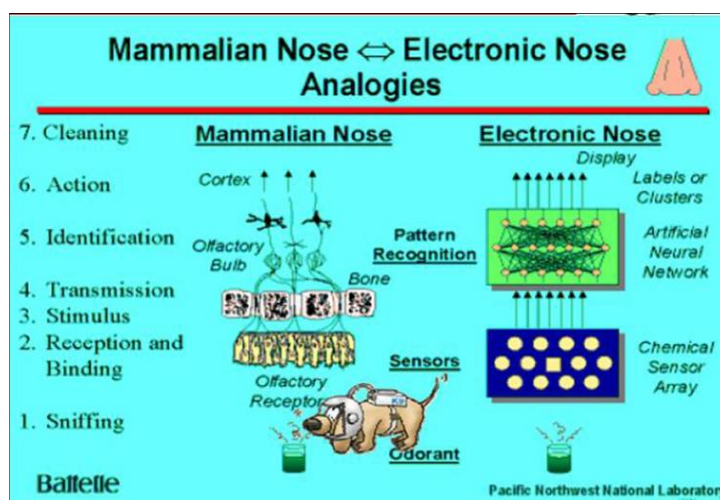


Figure 8.1: Comparison between Mammalian Nose and E-nose.

(Fig. from Pacific Northwest National Lab)

The human nose uses the lungs to bring the odor to the epithelium layer while the E-nose uses a pump. The human nose has mucous, hairs, and membranes to act as filters and concentrators. In case of the E-nose, it has an inlet sampling system that provides sample filtration and conditioning to protect the sensors and enhance selectivity. The human epithelium contains the olfactory epithelium that contains

millions of sensing cells that selected from 100-200 different genotypes which interact with the odorous molecules in unique ways. The E-nose has a variety of sensors that interact differently with the sample. The human receptors convert the chemical responses to electronic nerve impulses. The unique patterns of nerve impulses are propagated by neurons through a complex network before reaching the higher brain for interpretation. Similarly, the chemical sensors in the E-nose react with the sample and produce electrical signals. A computer reads the unique pattern of signals and interprets them with some form of intelligent pattern classification algorithm such as principal component analysis (PCA) or artificial neural network (ANN). The first E-nose experiments were conducted in the early 1980s [141]. In general, an E-nose includes three major parts: a sample delivery system, a detection system, a computing system. The construction of portable E-nose will be systematically explained in next section.

8.2 Construction of Portable E-nose

The schematic diagram of portable E-nose system is shown in Fig. 8.2. It consists of three main parts: (i) air flow system (ii) sensor chamber and (iii) data acquisition (DAQ) and measurement circuit.

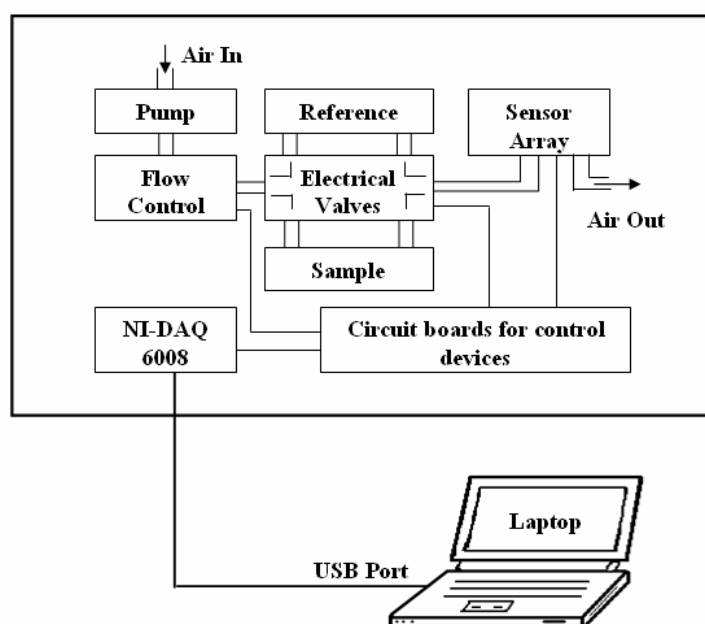


Figure 8.2: Schematic diagram of the portable E-nose system.

For the first part, the air flow system is comprised of air compressor, four electrically solenoid valves, sample and reference glass containers, stainless steel pipes, and mass flow controller. The clean air produced from air compressor carries aroma molecules of sample into a sensor chamber at a specific flow rate. The flow is controlled by a mass flow controller and four solenoid valves. The USB-DAQ card sends analog signal for flow rate adjustment and receives a set of digital signal back for reading the real-time flow rate value. When current flow rate reaches to a desired flow rate, the USB-DAQ card sends digital signal for selecting the path of air flow by controlling four solenoid valves. Switching between the reference and the sample glass containers is used to obtain the baseline and signal, respectively. Noteworthy, it can also be help to reduce the humidity effect that is a major problem in field application of the E-nose [142]. In second part, sensor chamber can be designed to deserve with the type of gas sensors. Based on our study, one of the best of sensor chambers is radially symmetric sensor chamber as shown in Fig. 8.3.

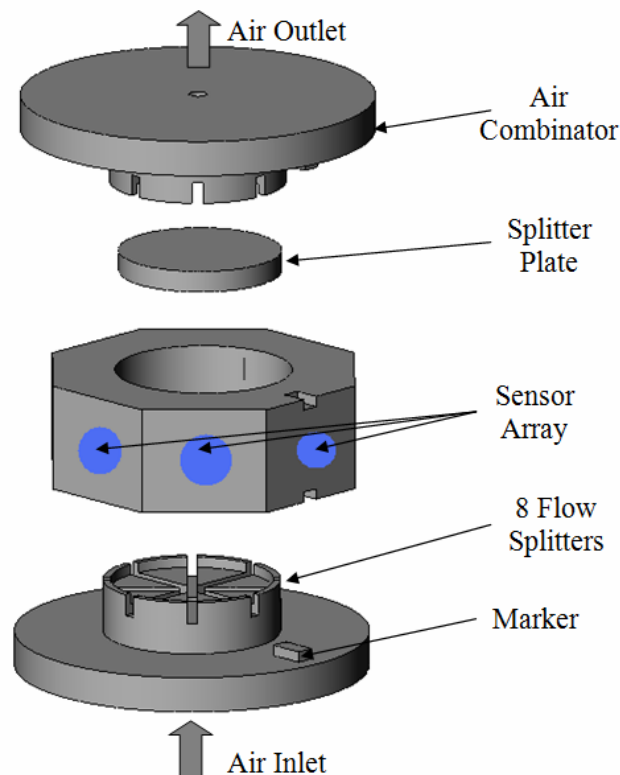


Figure 8.3: Radially symmetric sensor chamber.

This chamber has a radially symmetric flow splitter which all gas sensors can be simultaneously exposed to the same chemical samples under the same experimental conditions [143]. The air carrying the aroma molecules is introduced into the sensor chamber through 2.5 mm of caliber at the bottom of the chamber. Then, it is perpendicularly exposed to eight gas sensors by using eight flow splitters. Upper the eight flow splitters, there is a splitter plate to avoid a laminar air flow from bottom to top. The air from all sensors is combined again via air combinator while the temperature and humidity sensors are mounted underneath air combinator in order to measure the sensor chamber envelopment. For the measurement circuit, data acquisition is realized by a USB DAQ device (NI USB-6008) from National Instruments. A simple linear circuit, called as voltage divider, combined with an analog multiplexer is employed for measuring the resistance of each gas sensor. To obtain noise reduction and higher precision, RMS measurements with a low side lobe window are employed to apply to the signals [144, 145]. The main lobe is centred at each frequency component of the time domain signal and the side lobes approach zero at

$$\Delta f = \frac{F_s}{N} \quad (8.1)$$

where F_s is the frequency at which the acquired time domain signal was sampled. N is the number of points in the acquired time domain signal. The resulting values of each sensor were recorded every 1 s for subsequent analyses.

8.3 Principal Component Analysis

Principal Component Analysis (PCA) was used for pattern recognition and classification of samples measured by the portable E-nose. PCA is a statistical technique that allows an easy visualization of all correlated information [146]. In principles, PCA process contains five steps as follows:

- i. Get data from matrix, $X_{M \times N}$. The row M represents different repetition of the experiment and the column N represents the number of independent sensors.

- ii. Normalize the data matrix, $Norm(X_{M \times N})$, by the mean subtraction. The mean of each N column is calculated and subtracted from the data set. Hence, the new data set produces the mean equal to zero.
- iii. Calculate the covariance matrix, $Cov(X_{M \times N})$, and calculate eigenvectors and eigenvalues of the covariance matrix. The calculated eigenvectors must be unit eigenvectors.
- iv. Rearrange the eigenvectors and eigenvalues. The eigenvectors are ordered by eigenvalues from highest to lowest, $(\overline{Cov(X_{M \times N})})_{\max \rightarrow \min}$.
- v. Obtain the PCA result by matrix multiplication and transpose, $(\overline{Cov(X_{M \times N})})_{\max \rightarrow \min} \otimes Norm(X_{M \times N})^T$. The obtained new dataset with orthogonal linear transformation have been plotted in two or three dimensions containing the most relevant of the data set.

8.4 Feature Extraction Techniques

Preprocessing or feature extraction from the acquired sensor signal prior to the use of PCA is very necessary to get better separation. In general, only simple features, i.e., the maximum and minimum resistances as obtained from switching between the reference and sample, were extracted and used for analyses, as shown in Fig. 8.4.

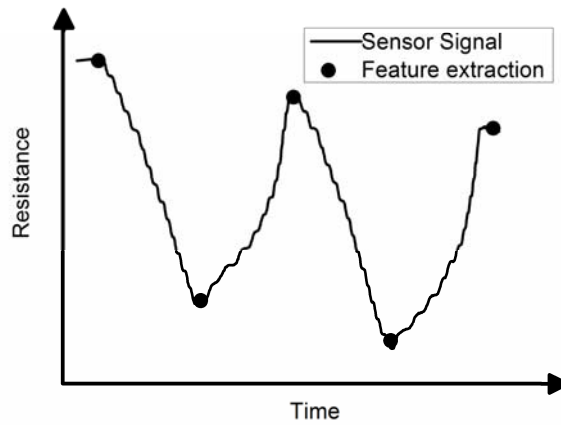


Figure 8.4: Typical raw data from a sensor and the max/min feature extraction on each curve.

The maximum and minimum resistances were the averaged values of their 10 neighboring data points. Since there is a gradual change in the reference and sample resistances over time, it is necessary to correct such baseline shift as time proceeds (See Fig. 8.5).

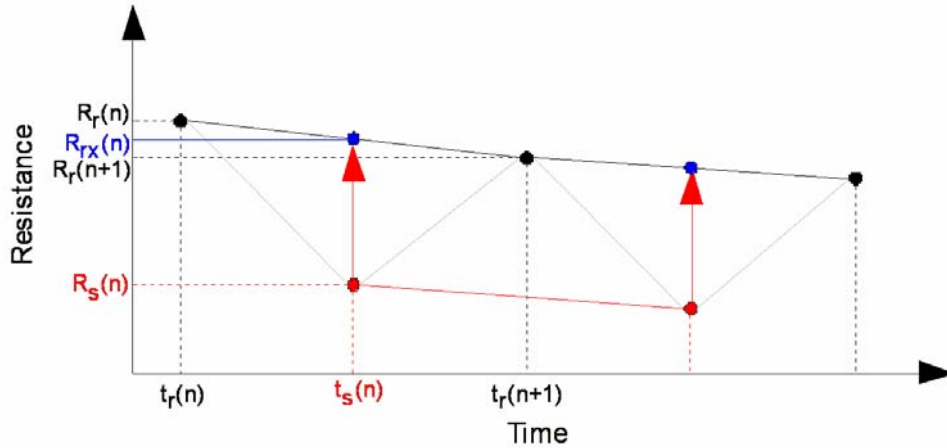


Figure 8.5: Correction method of baseline shift as time proceeds.

From Fig. 8.5, index r denotes the reference, while index s denotes the sample. Index rx is defined as a baseline-corrected reference value. The variable (n) represents the running number of measurement loop (switching between the reference and sample). A linear interpolation is used as a baseline connecting between two reference points $(R_r(n)$ and $R_r(n+1))$. The corrected reference point $(R_{rx}(n))$ is calculated by projecting the sample point onto the baseline. As a result, the baseline-corrected difference between the sample and reference resistances is calculated via the following formula:

$$\Delta R(n) = R_s(n) - R_{rx}(n) \quad (8.2)$$

$$\text{Where } R_{rx}(n) = \frac{R_r(n+1) - R_r(n)}{2} + R_r(n) \quad (8.3)$$

However, the max/min feature extraction is not enough to classification by PCA for some cases. New feature extraction methods that to higher classification performance as compared to the classical features have been proposed [124]. That is integral and primary derivative.

Two features; integral and primary derivative, having specific physical meanings were proposed as the following formulation:

$$\text{Integral; } I_i = \int_a^b V_{out} dt \quad (8.4)$$

$$\text{Primary derivative; } D_i = \frac{dV_{out}}{dt} \quad (8.5)$$

where V_{out} represents a sensor signal.

In real calculation, the integral and primary derivative of V_{out} are obtained from the elements of y_i^I and y_i^D , respectively using the following relations;

$$y_i^I = \frac{1}{6} \sum_{j=0}^i (x_{j-1} + 4x_j + x_{j+1}) dt \quad (8.6)$$

$$y_i^D = \frac{1}{2dt} (x_{i+1} - x_{i-1}) \quad (8.7)$$

Where $i = 0, 1, 2, \dots, n - 1$ and n is the number of samples.

In addition, signal integral refers to the accumulative total of the reaction degree-changing while primary derivative of signal represents the reaction rate [147,148].

8.5 Conclusion

In this chapter, we have reported how to invent a portable E-nose which is inexpensive, fast, reliable and suitable for use for the detection and classification of both solid and liquid samples. In addition, feature extraction techniques including integral and primary derivative have been proposed for improving classification performance by PCA.

CHAPTER IX

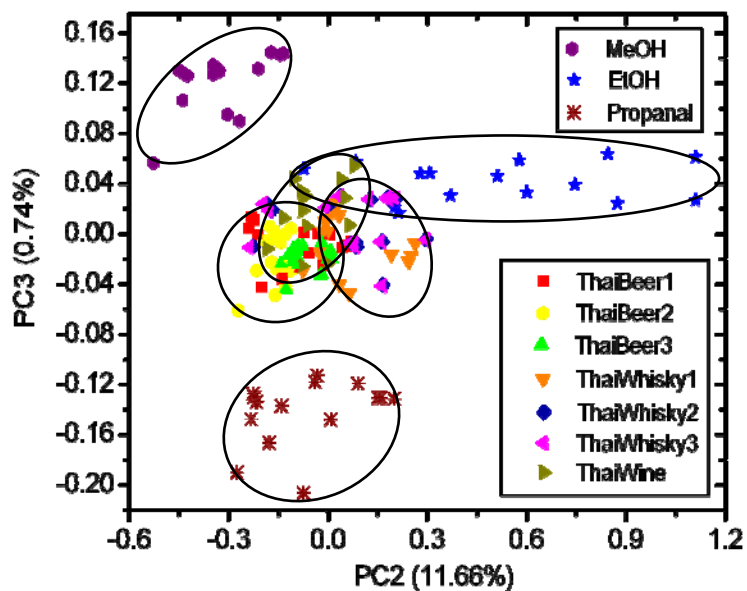
REAL WORLD APPLICATION OF E-NOSE

9.1 Detection and Discrimination of Volatile Organic Compounds

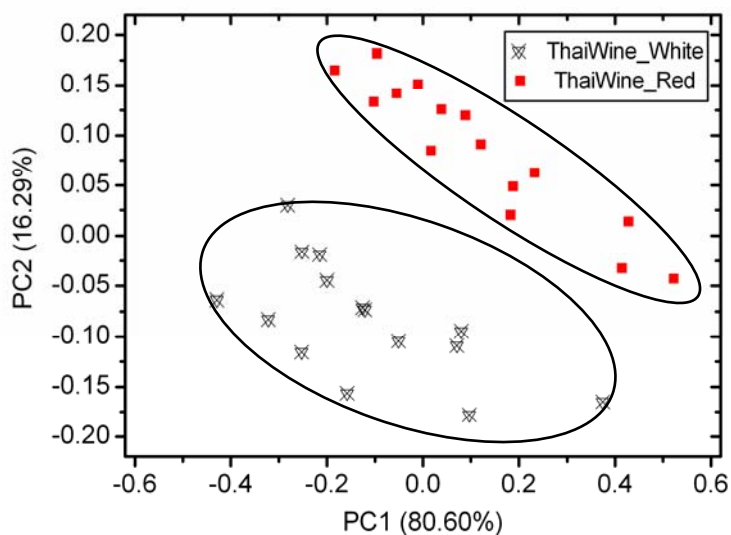
From chapter 6, pure and Au-doped ZnO nanostructure sensors prepared using thermal oxidation technique were found to be suitable to employ in detecting alcoholic solution and beverages. The ethanol, methanol, propanol and various Thai beer, Thai wine and Thai whiskey samples were measured using the E-nose based on these two nanosensors. The data were introduced into PCA for recognition and discrimination of samples. The PCA method can be used for dimensionality reduction of a dataset while retaining those characteristics of the dataset that contribute most to its variance as shown in chapter 8.4. The input data can be the percentage change of every sensor or only some sensors for multiple measurements of different samples. However, in this E-nose, there are only two sensors. It means that the dataset only has two dimensions. Feature extraction techniques need to be applied to raw data for selecting the appropriate data and for increasing the dimension. The last 10 samples of each sensor before and after switching to another line were averaged. The difference of both values was used. Another feature can be extracted from the range of decay times. The difference of slope for the sample measurement was also used. Therefore, one experiment can give four different sensor output features.

Figure 9.1 shows two-dimensional PCA results for discrimination of alcohols. In Fig. 9.1a, it can be observed that the E-nose based on two nanosensors can discriminate quite well between the ethanol, methanol and propanol with PC2 of 11.66% and PC3 of 0.74%. Thai alcoholic beverage sample points locate around the ethanol sample points because alcoholic beverages have the contents of ethanol. However, in the case of Thai wines having the same percentage of alcohol (12.5% alcohol by volume), the E-nose can clearly discriminate the white and red wines as shown in Fig. 9.1b with PC1 of 80.60% and PC2 of 16.29%. The discrimination of

white and red wines even with the same alcohol amount indicates that the E-nose is sensitive to other vapour ingredients apart from alcohols as well.



(a)



(b)

Figure 9.1: Results of PCA for discriminate of (a) alcohols and (b) typical Thai wines.

9.2 Detection and Classification of Human Body Odor

9.2.1 Background

Nowadays, E-nose are well-known as efficient analytic devices that are widely used for many applications such as quality control of foods [149–153] and beverages [154–157], public safety [158,159], air protection [160,161] and medical applications [162–166]. Recently, there have been increasing interests in the application of E-nose for measurement of human body odors. If successful, many new applications await in such area as healthcare monitoring, biometrics and cosmetics. In principles, the human body dynamically generates unique patterns of volatile organic compounds (VOCs) under diverse living conditions such as eating, drinking, sexual activities, health or hormonal status [167]. These VOCs released from the human body can give some information about diseases, behavior, emotional state and health status of a person [168]. In addition, body odor is one of the physical characteristics of a human that can be used to identify people [169]. The human odor is released from various parts of body and exists in various forms such as exhalation, armpits, urine, stools, farts or feet. Natale *et al.* [170] developed an E-nose that can diagnose the urine odor of the patients with kidney disorders. Phillips and co-workers demonstrated the detection of lung cancer [171] and breast cancer [172] from human breath using E-nose. An E-nose was also tested to help monitor alcoholic consumption of aged persons by measuring the odors from exhalation [173]. However, to our best knowledge, no report is yet available on E-nose monitoring of human armpit odor. In fact, the armpit is a skin region where a vast number of glands and bacteria cooperate to produce a strong smell [174,175]. It can be the best source for sampling volatile chemicals released from the human body, which may give a unique pattern allowing identification of different persons.

One important obstacle to the detection the human body odor from armpits is sweat. Each day, humans produce different quantities of sweat, depending on the environment and, more importantly, life activities. Since it is well-known that most gas sensors are to some extent sensitive to humidity [176] this varying sweat content can be a problem for measurement of armpit odor samples. Therefore, a correction of the humidity effect is necessary to ensure a pure sensor response to only the volatile organic compounds that match with the identity of individual persons.

Another problem for E-nose measurement of armpit odor is the disturbance from artificial chemicals such as deodorants because most adult people utilize deodorants to reduce unpleasant body odor. An interesting question arises whether E-nose can identify persons using deodorant or not? If both problems can be solved, biometrics based on armpit odor recognition would become viable.

In this section, we propose a strategy to identify persons based on measurement of human body odor from armpits. To demonstrate this concept, we have designed and constructed an E-nose based on a set of metal oxide gas sensors as shown in Table 9.1. With this E-nose and the proposed method, identification of two persons either with or without using deodorant could be achieved.

Table 9.1: Specifications of each metal oxide sensor.

Sensor	Target Gas	Typical Detection Ranges	Heater Power Consumption
TGS 813	Combustible gases	500 - 10,000ppm	835 mW
TGS 822	Organic solvent vapors	50 - 5,000ppm	660 mW
TGS 825	Hydrogen sulfide	5 - 100ppm	660 mW
TGS 880	Cooking vapors	10 - 1,000ppm	835 mW
TGS 2602	Air contaminants	1 - 30ppm	280 mW

In this work, we have used gas sensors as commercially available from Figaro Engineering Inc (TGS gas sensor). The gas sensors, as listed in Table 9.1, were selected in order to cover the targeted gases that presented in human body odor [177].

9.2.2 Humidity Control

As discussed in the introduction, most chemical gas sensors are sensitive to humidity. Therefore, if two identical samples with a different humidity are measured, the results can be different. In our work, we propose two methods as solutions to this problem. The first is a hardware-based method, where the sample was handled so as to have almost the same humidity as the background. Under such

condition, the humidity signals will be equivalent for the sample and the reference, thereby only signals from the odors of interest result. To produce a constant humidity background, the carrier gas was directed to flow through a liquid water container that is immersed in a temperature-controlled heat bath (see Figure 9.2). The temperature of the heat bath can be adjusted until the generated humidity reaches the desired value. It is intuitive to anticipate that the native humidity would be lower than the higher generated humidity. We have done an experiment to investigate whether the generated humidity could overcome the native humidity of the samples. A humidity sensor was installed inside the sensor chamber. The temperature of the heat bath was adjusted until the reference humidity reached a desired value of 25%, 50% and 75%, respectively. Then, the humidity difference between the reference and the sample was compared and discussed (Section 9.2.5).

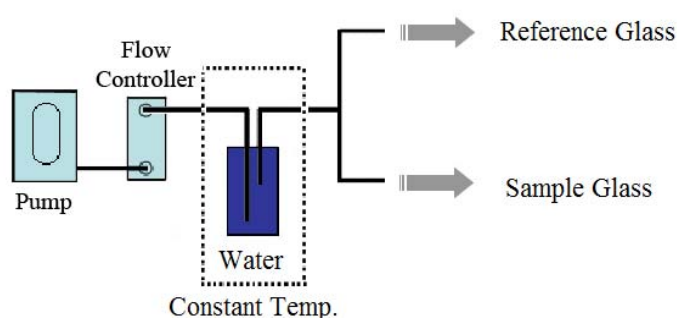


Figure 9.2: Schematic diagram of humidity control using hardware-based method.

The second solution to the humidity problem is a software-based approach. A mathematical model describing the resistance of each gas sensor at different humidity level can be calibrated to subtract the humidity signal from the total signal. Although each aforementioned approach can be used independently, we have employed both schemes concurrently to achieve maximum accuracy. In addition, it should be noted that these humidity corrections could be applied in other E-nose systems or in the field conditions. Samples other than the human body odor can also be used with this algorithm. However, varying humidity (10–90%) should be tested before a measurement of a desired sample.

9.2.3 Human Body Odor Collection

Human body odors from armpits were collected from two male volunteers. The experiment was performed for five days with a sample collection of the armpit odors in the morning right after waking up (the volunteers typically wake up around 7–8 am) and in the afternoon (8 hours later). Cotton pads were used to transfer the odors from the armpits to the E-nose. A cotton pad must be in direct contact with the armpit for 10 minutes and stored in a special sample glass bottles with a screw-on closure. Once the morning samples were collected, the glass bottles were transferred to laboratory for E-nose measurement. To minimize the odor change due to bacteria, the samples, transferred via a heat protection container, were measured within 30–50 minutes after sample collection. For the afternoon samples, E-nose measurement can be done immediately after odor sampling.

During the experiment period, the volunteers were requested to go about their ordinary life and activities: for example, they took a shower twice a day (before going to bed and after waking up following the morning sample collection). To avoid fluctuation in odor samples, they were not allowed to have sex and/or consume alcohol. To study the effects from deodorant, the volunteers were requested to use deodorant, after taking shower in the morning, but only on the right arm.

9.2.4 Evaluation of Sensor Response to Body Odor Strength

There are more refined and less subjective ways to measure odor strength in direct way. For instance, the concept of dilution-to-threshold principle can be used quite accurately to reduce uncertainties associated with subjective impressions [178–180]. In the cosmetic industry, human olfaction has been commonly employed to evaluate the odor strength of armpit for the development of deodorants. The armpit odor comprises a complex set of chemicals. Previously, isovaleric acid and volatile steroids (such as androstenone, androstadienone and androstenol) were thought to be the major contributors to armpit odor. However, armpit odor having more distinct and pungent odor involves the presence of other volatile compounds as well [181–183]. To simplify the odor strength of armpit, only a single component such as isovaleric acid can be used for training the sensory panel [184] and representing the sweaty primary odor [185,186] that contributes mainly to the armpit malodor. Hooper et al

[184,187] assigned the concentrations of isovaleric acid levels on a scale 0 to 5 corresponding to subjective impression by using human nose, as shown in Table 9.2. Their test was carried out by a team of three female assessors of ages ranging from 20 to 40 years. They were selected for olfactory evaluation on the basis that each person is able to rank correctly the odor levels of the series of aqueous isovaleric acid solution listed in Table 9.2. The scale 0 to 5 has been usually used to represent the intensity of the armpit smell in the cosmetic industry. The judges are trained to memorize this scale and classify the odor strength of the samples. In this work, we evaluated the performance of E-nose in classification of body odor strength using isovaleric acid solutions prepared according to the intensity scale. A cosmetic face-cleaning pad with 0.15 mL of aqueous isovaleric solution was placed into a glass container for measurement.

Table 9.2: The concentration of the isovaleric acid levels that correspond to subjective impression by using human nose.

Level	Concentration of aqueous isovaleric acid solution (mM)	Subjective impression
0	0	No odor
1	0.12	Slight
2	0.48	Definite
3	1.99	Moderate
4	7.88	Strong
5	32.33	Very strong

9.2.5 Correction of Humidity Effects

To investigate the sensor response to humidity, the relative humidity [%RH] was varied from 30% to 80%. Resistances arisen from humidity of TGS 813, TGS 825, and TGS 2602 sensors are displayed in Fig. 9.3a, 9.3b and 9.3c,

respectively. The graphs for TGS 822 and TSG880 are not shown in this paper of which behaviors are similar to TGS 813. Mathematical models for the sensors' response to humidity can be fitted via the following formulations.

Exponential equation of TGS 813:

$$R_{S_{813}} = 86682.00 \exp\left(\frac{-[\%RH]}{29.05}\right) + 55063.48 \quad (9.1)$$

Exponential equation of TGS 822:

$$R_{S_{822}} = 24931.58 \exp\left(\frac{-[\%RH]}{37.48}\right) + 9054.41 \quad (9.2)$$

Exponential equation of TGS 880:

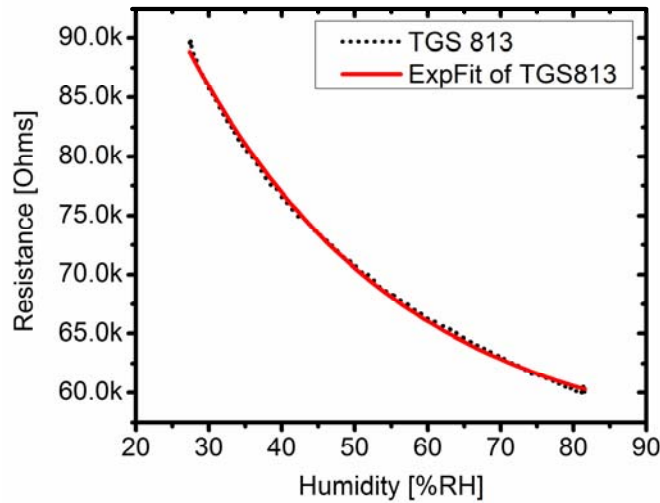
$$R_{S_{880}} = 90496.88 \exp\left(\frac{-[\%RH]}{36.33}\right) + 55135.22 \quad (9.3)$$

Polynomial equation of TGS 2602:

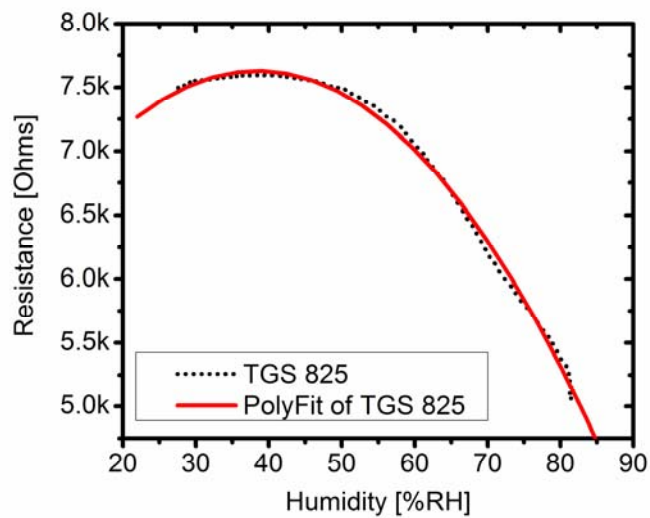
$$R_{S_{2602}} = 6958.22 + 129.172[\%RH] - 0.9788[\%RH]^2 \quad (9.4)$$

Polynomial equation of TGS 825:

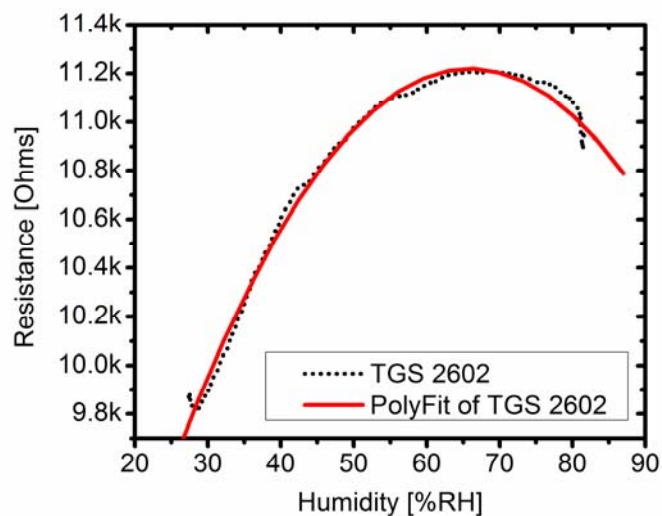
$$R_{S_{825}} = 5646.63 + 103.26[\%RH] - 1.34[\%RH]^2 \quad (9.5)$$



(a)



(b)



(c)

Figure 9.3: Resistance of sensors (a) TGS 813, (b) TGS 825 and (c) TGS 2602 versus relative humidity.

These mathematical models were included in the data acquisition and analysis codes, thus allowing the response of sensors to humidity of the samples to be corrected on the fly. However, to achieve the maximum accuracy, hardware correction as shown in Fig. 9.2 is co-employed. It was expected that, if the generated

background humidity dominates the humidity of the sample, the effect arising from the humidity difference between the reference and the sample would be minimized. We have tested this assumption by measuring the armpit odor sample of a volunteer. Various humidity references, e.g., 25%, 50% and 70%, were generated and flowed through the sample. Table 9.3 shows absolute average percentage changes of resistances of each sensor and their standard deviations (or standard error) upon varying humidity background. Each average percentage changes of resistance presented in Table 9.3 was obtained by averaging data from 3 repeated measurements, in which each measurement performs switching between the reference and sample for 5 cycles (totally 15 dataset of each sensor were averaged). It was found that the change of the resistance between the reference (pure cotton pad) and the sample (cotton pad + sweat + armpit odor) and its error value become smaller when the background humidity was increased from 25% to 75%. The variation in each measurement, as implied by the standard error, was also reduced from +/- 51% with low humidity background to +/- 7% with higher humidity background, indicating that fluctuation in the dynamic measurement was also reduced. The decreasing error indicates less fluctuation of the sensor response arising from the humidity in sweat. At a lower relative humidity, the sweat in the cotton pad can evaporate much easier and contributes in a large part for the difference of resistances between the reference and the sample. At a higher relative humidity, the generated humidity weighs off the native humidity of the sample, thereby reducing the humidity difference between the reference and the sample. As shown on the right-most column of Table 9.3, the humidity difference between the reference and the sample decreases from 2.8% to only 0.29% when the generated humidity at 25% was replaced by higher relative humidity at 75%. However, saturated humidity (100%) is not recommended because it will suppress evaporation of odor molecules, which deteriorates the measurement.

The hardware-based method helps to reduce the effect arising from the humidity reference between the reference and the sample. It can be said that the sensor signals consists in a large part contribution from the odors of interest. Thus, relative humidity at 75% was applied in all experiments for measuring the human body odors in this work.

Table 9.3: The absolute average percentage change of resistance of each sensor upon varying humidity generated by hardware correction.

Background humidity	TGS813	TGS825	TGS2602	TGS880	TGS822	Humidity sensor
25%	3.948 (± 55%)	2.211 (± 38%)	3.727 (± 38%)	4.765 (± 37%)	5.529 (± 43%)	2.823 (± 51%)
50%	0.526 (± 16%)	0.104 (± 23%)	0.264 (± 27%)	0.702 (± 25%)	2.150 (± 25%)	0.550 (± 20%)
75%	0.158 (± 4%)	0.057 (± 8%)	0.581 (± 4%)	0.160 (± 5%)	0.185 (± 7%)	0.293 (± 7%)

9.2.6 Evaluation of Sensor Response to Body Odor Strength

The response of each sensor to the isovaleric acid prepared according the intensity levels 1 to 5 is displayed in Fig. 9.4. It can be seen that all sensors can discriminate intensity level 3, 4 and 5, but fail to distinguish level 0, 1 and 2. TGS2602 exhibits the highest response to the isovaleric acid. Since the intensity level of isovaleric acid has an exponential relation with the concentration (as seen in Table 9.2), the sensor response may be mathematically adjusted in order to understand the relationship between the sensor response with the intensity level, using the logarithmic function:

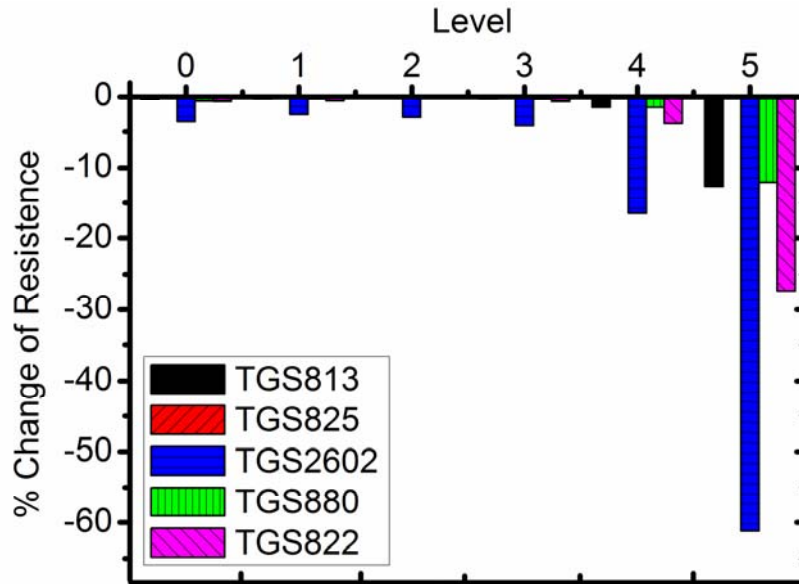
$$Y = \ln(1 - \% R_s) \quad (9.6)$$

As shown Fig. 9.4b, the logarithm of sensor response is linear with the odor strength for the intensity levels 3-5. The intensity threshold to isovaleric acid for all sensors is the intensity level 3. It implies that our E-nose may be limited to classify odor strength of persons who have at least definite armpit smell. Therefore, we have chosen two volunteers who have moderate armpit odors for E-nose measurement.

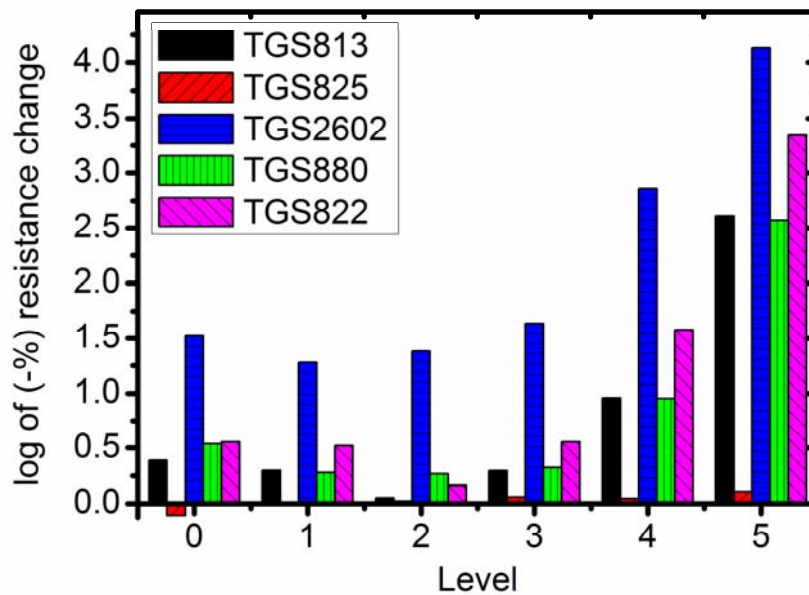
9.2.7 Detection and Classification of Human Body Odor

Armpit odors of two volunteer persons were measured by E-nose during 5 days using a combined hardware/software humidity correction. Fig. 9.5a and 9.5b

exhibit the average of sensor response over 5 days as measured on the left (denoted by L) and right (denoted by R) armpits.

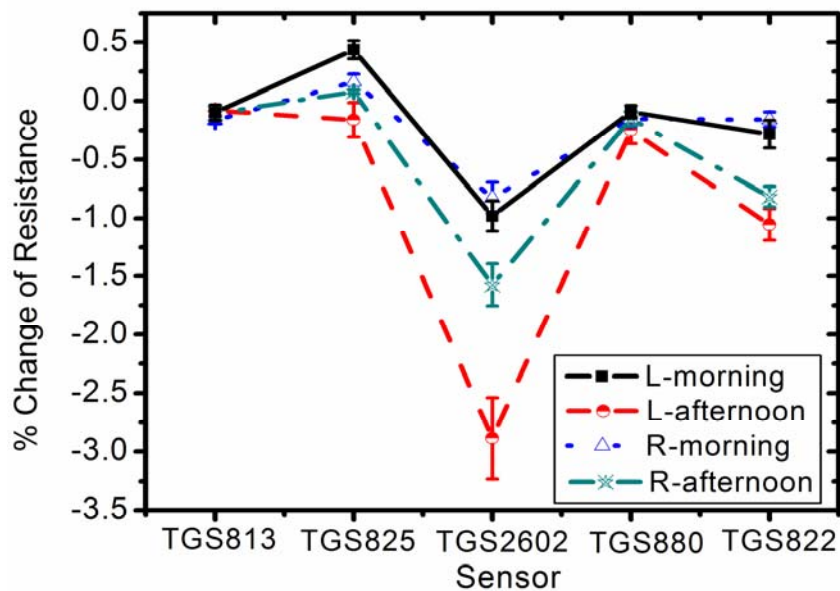


(a)

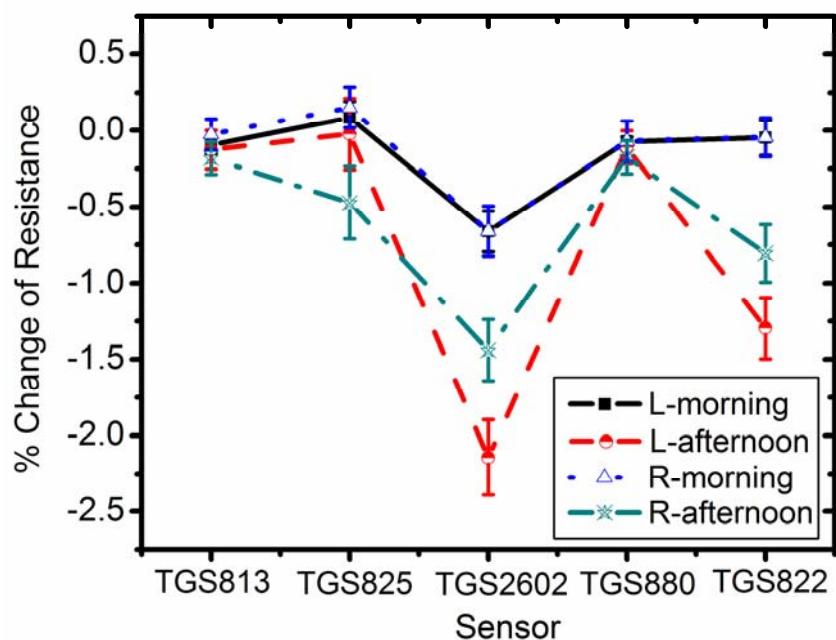


(b)

Figure 9.4: (a) Sensor response to isovaleric acid at different intensity level. (b) Logarithmic plot of the sensor response.



(a)



(b)

Figure 9.5: The sensor response with error bar of (a) person A and (b) person B in the morning and the afternoon. L and R denote the left and right armpits, respectively.

From Fig. 9.5, it was found that TGS822 and TGS2602 have high response to human body odor in agreement with previous tests with isovaleric acid. Odor analysis of each person gives an interesting pattern. In the morning, both volunteers have only weak armpit odor, while the odor strength increases markedly in the afternoon. It can be seen from all sensors that the left and right arms of a person yield almost equivalent signals in the morning, since no deodorant was allowed before sample collection. In contrast, the afternoon results of the left and right arms deviate distinctly. The deodorant-free left armpit expresses noticeably higher signal strength. The difference of signal strength between morning and afternoon of each armpit was tested using a paired t-test with a significance level of 95% confidence ($P = 0.05$). Both person A and person B have a similar pattern in the difference of signal strength between morning and afternoon. For the person A, the mean difference of left armpit and right armpit between morning and afternoon are 1.500 % change of resistance ($P=0.036$) and 0.700 % change of resistance ($P=0.250$), respectively. In case of person B, the mean difference of left armpit and right armpit between morning and afternoon are 1.365 % change of resistance ($P=0.004$) and 0.775 % change of resistance ($P=0.054$), respectively. The paired t-test shows that the signal strength of deodorant-free left armpit ($P<0.05$) have statistically significant difference between morning and afternoon at the level of 95% confidence. In contrast, the changes of deodorant right armpit between morning and afternoon ($P>0.05$) did not reach the level of statistical significance. In general, deodorants suppress the armpit smell by reducing bacteria activities. Hence, an interesting question arises, “can deodorant blind human identification by E-nose ?”

To allow an identification of human odors from two persons, Only the data from the afternoon measurement was introduced into PCA. The PCA result is shown in Fig. 9.6. The first principal component (PC1) explains 74.0% of the total variance and the second principal component (PC2) contributes 21.7% of the variation. The PCA result obviously identifies person A from person B. It indicates that each person has a specific odor pattern although these people conduct a similar life style. After both persons arrived at the laboratory, they have spent most of the time under the same humidity and temperature. The afternoon sample collection took place almost at the same time and the samples were subjected to measurement

immediately. Therefore, the afternoon measurement should be more reliable than the morning one in which the odor change from bacteria could occur. The use of deodorant may not change the odor fingerprint, though it undoubtedly reducing the strength of a key chemical such as isovaleric acid that exerts strongly on perception of body's smell. In Fig. 9.6, each data point is plotted from day 1 to day 5. It can be seen that the odor of both armpits change everyday but PCA can still group the data of each person together. Therefore, E-nose can be a prospective candidate for identification or authentication of a person like other biometrical technologies [188].

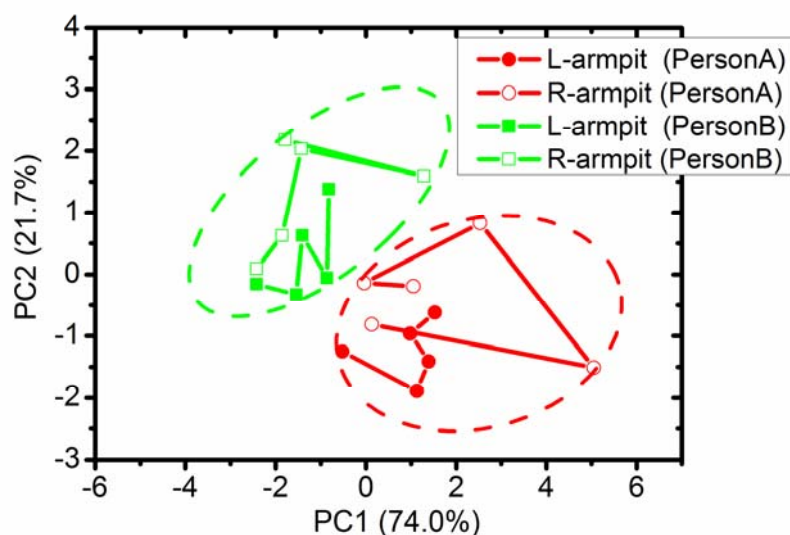
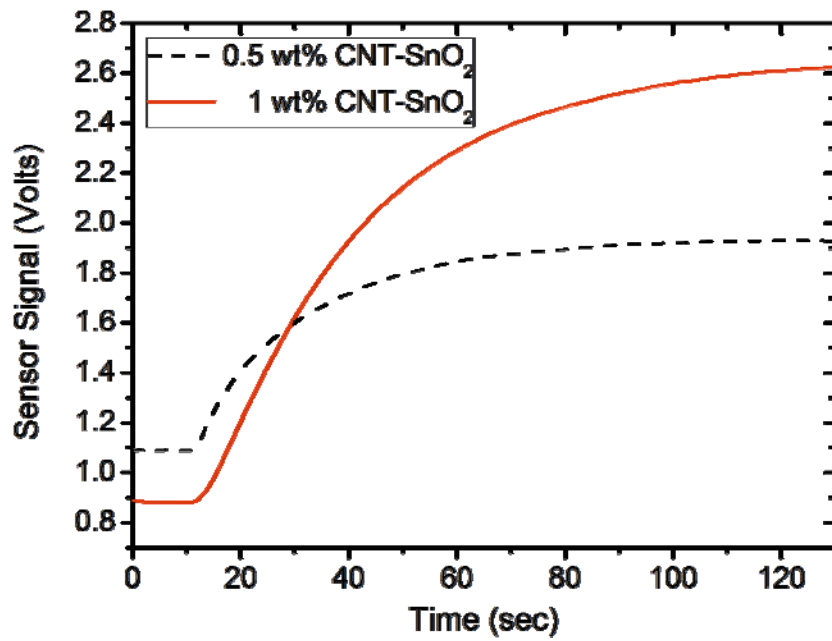


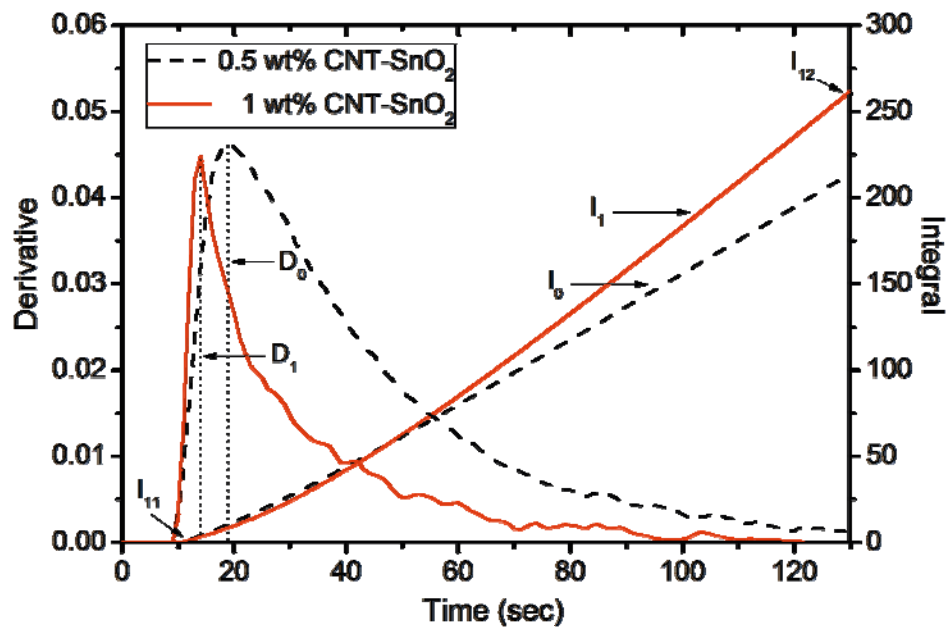
Figure 9.6: The 2D-PCA of armpit odors from two persons as measured in the afternoon during 5 days.

9.3 Detection of Methanol Contamination in Whiskeys

The last example of real-world application of our E-nose is to detect methanol contamination in whiskey. The carbon nanotube-doped SnO_2 gas sensors prepared by E-beam evaporation (see chapter 6.4) were employed in sensing part of the portable E-nose. Since the fabricated sensors show different response to EtOH and MeOH, the E-nose based on such sensors can be applied to monitor MeOH contaminant in whiskey. Typical e-nose response to a whiskey is displayed in Fig. 9.7a while the integral and primary derivative of the response are shown in Fig. 9.7b.



(a)



(b)

Figure 9.7: (a) Raw responses (b) primary derivative and integral signals of gas sensors measured using portable E-nose.

From each sensor response curve, four different features were extracted for each sample. The first feature extraction is the conductance change, defined as $\Delta R = R_{\text{gas}} - R_0$. The second feature extraction is the relative response ($\Delta R/R_0$). The third feature extraction is the integral (see section 8.4). This feature was extracted by calculation of difference accumulative total reaction in the presence of sample gas, i.e. $I_{12} - I_{11}$ (see Fig. 9.7b). The last one is the primary derivative (see section 8.4). The maximum amplitude in the same interval was employed, i.e. D_0 and D_1 (see Fig. 9.7b). Each data set extracted from each proposed feature in the form of $X_{56 \times 2}$ is introduced into the PCA process. PCA results of the datasets extracted by the proposed methods; ΔR , $\Delta R/R_0$, integral and primary derivative are shown in Fig. 9.8a-9.8d, respectively.

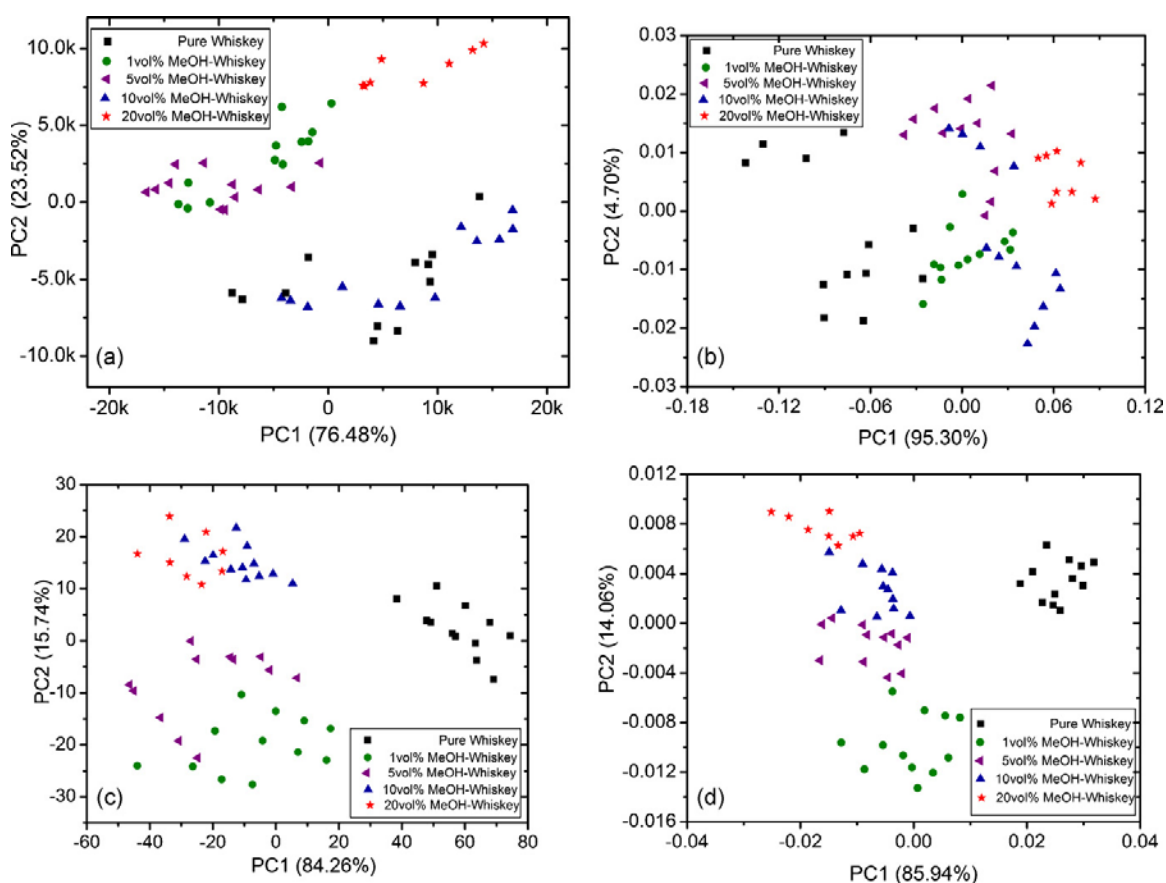


Figure 9.8: PCA results using feature extraction from (a) ΔR , (b) $\Delta R/R_0$ and (c) integral and (d) primary derivative.

The PCA results show that the feature extraction based on ΔR cannot classify the contamination of MeOH in whiskey due to the drift effect of sensor signal depending on temperature variation in the long time measurement. The classical relative response ($\Delta R/R_0$) seems to give a better result than ΔR but many samples disperse in the same region and pure whiskey results locate rather close to whiskey having 1 vol% of MeOH contamination while MeOH content exceeding 2% (v/v) would harm the consumer [189]. In such case, the resolution power is not enough to guarantee the contamination of MeOH in whiskey. For feature extraction using both the integral and primary derivative data treatments, PCA results show a perfect classification between pure whiskey and whiskey having MeOH contamination. Moreover, the primary derivative can cluster all level of MeOH contaminations (1 vol%, 5 vol%, 10 vol% and 20 vol%) in the whiskey as shown in Fig. 9.8d. These results indicate that the proposed feature extractions, integral and primary derivative, provide good capabilities in the recognition and discrimination of MeOH contamination. These may be alternative ways to replace the common methods (ΔR and $\Delta R/R_0$) which are widely used in PCA analysis.

From our PCA results together with feature extraction technique, it can be seen that although the sensors are structurally similar, they can have sufficiently distinct response such that it can be used to discriminate different kind of similar odors. However, it should be noted that features extracted from response behaviors can be dependent on some measuring details such as chamber size, gas flow rate, and sensor position in the sensor chamber. Consequently, the feature extraction result can be considerably different for different E-nose systems. Nevertheless, it should not be a problem for E-nose applications because this can be well controlled for each E-nose system and any E-nose system must always be trained under a fixed condition.

9.4 Conclusion

In this section, real world applications of our E-noses combined with various types of our gas sensors and data processing techniques have been reported. It can be summarized into three main applications:

- The portable E-nose can detect the difference between alcohol beverages and alcohol solutions and can distinguish the difference of white and red wines having the same percentage of alcohol.

- The E-nose in conjunction with PCA method was shown to differentiate the body odors of two persons with similar life style and activities. In addition, we have found that deodorant does not effect the relative identification of these two persons. This work will open the door to the field of human body odor biometrics.

- Moreover, the portable E-nose shows clearly the classification of MeOH contamination mixed in the whiskey at higher concentrations than 1% by volume. Our E-nose will be a useful tool for the whiskey industry and for quick screening of village-made whiskeys that are usually found of the MeOH contaminant.

CHAPTER X

SUMMARY

Summary of finding for this thesis can be classified into four main works:

(a) Molecular modeling

- DFTB is an approximate method based on the density functional framework.
- The DFTB can be useful in calculations of large systems with relatively good accuracy.
- To study the formation of SiC nanotube, Si atoms can not go into the IWS through a perfect sidewall.
- Defects on side wall of CNTs play an important role for formation of the clean SiC nanotube.
- SiCNTs prefers to form sp^2 bonds between a Si atom and a C atom.

(b) Synthesis of Nanomaterials

- There are two approaches for the manufacture of nanoscale materials, namely; (I) top-down and (II) bottom-up methods.
- ZnO nanomaterials can be grown in an amazingly rich variety of shapes by varying only two parameters including the powder source temperature and the substrate temperature.
- The substrate temperature affects the kinetics and the thermodynamics of the condensation and the growth while the powder source temperature affects the nature and generation rate of growth species.
- The ZnO nanowire nucleation is larger for lower substrate temperature (larger condensation rate).
- Both the catalyst free (VS) and the catalyst assisted (VLS) modes are occurring simultaneously for triangular nanosheets formation.

- Spear-like morphology can be formed in case of Zn incorporation rate by a catalyst assisted VLS growth is not large enough to consume a large concentration of Zn (as expected for large powder source temperature).

(c) Fabrication of Nanostructure Gas Sensors

- Electron beam evaporation process is one of the best methods for fabricating nanostructure gas sensors because it offers extensive possibilities for controlling film structure and morphology with desired properties such as dense coating, high thermal efficiency, low contamination, high reliability and high productivity.

- The 1 wt% CNTs-doped metal oxides, i.e. SnO₂ and WO₃, exhibit behavior of the n-type semiconductors.

- Doping of CNTs does not significantly change any surface morphology of the sensing film. Instead, it has introduced nanochannels and formed p-n heterojunctions in the metal oxide matrix.

- The CNTs-doped WO₃ sensor exhibits high sensitivity to H₂ while CNTs-doped SnO₂ sensor shows high response to EtOH and MeOH.

- Doping of CNTs can be help to reduce operating temperature of metal oxide gas sensors.

- Doping 10 wt% Au could improve the sensitivity of ZnO gas sensors on VOCs.

- The responses of the Au-doped ZnO gas sensors are linear with gas concentrations varying from 100 to 1000 ppm.

(d) E-nose and its Application

- E-nose refers to an instrument which comprises an array of electronic chemical sensors with partial specificity and an appropriate pattern recognition system, capable of recognizing simple or complex odours.

- An E-nose consists of three main parts: (i) air flow system (ii) sensor chamber and (iii) data acquisition (DAQ) and measurement circuit.

- Radially symmetric sensor chamber is one of the best of sensor chambers which all gas sensors can be simultaneously exposed to the same chemical samples under the same experimental conditions.

- The reference glass containers in air flow system can be help to reduce the humidity effect that is a major problem in field application of the E-nose.

- New feature extraction methods including integral and primary derivative can be a higher classification performance as compared to the classical features.

- Our E-noses can be widely used for many applications such as quality control of foods and beverages, air protection and human identification.

REFERENCES

1. E. Gazit, Plenty of room for biology at the bottom: an introduction to bionanotechnology, *Imperial College Press, London*, 2007.
2. P. Webster, World nanobiotechnology market, *Frost & Sullivan*, 2005.
3. K. J. Morrow, R. Bawa, C. Wei, Recent advance in basic and clinical nanomedicine, *Med. Clin. N. Am.* **9** (2007) 805-843.
4. C. Loo, A. Lin, L. Hirsch, M. H. Lee, J. Barton, N. Halas, J. West, R. Drezek, Nanoshell-enabled photonics-based imaging and therapy of cancer, *Tech. Canc. Res. Treat.* **3** (2004) 33–40.
5. M. Meyyappan, Moore and more progress in electronics and photonics, *Nanotechnology* **20** (2009) 430203.
6. M. H. Huang, S. Mao, H. Feick, H. Yan, Y. Wu, H. Kind, E. Weber, R. Russo, P. Yang, Room-temperature ultraviolet nanowire nanolasers, *Science* **292** (2001) 1897-1899.
7. http://en.wikipedia.org/wiki/Molecular_modelling
8. D. C. Young, Computational Chemistry: A practical guide for applying techniques to real-world problems, Wiley-Interscience 2001.
9. Th. Frauenheim, G. Seifert, M. Elstner, Z. Hajnal, G. Jungnickel, D. Porezag, S. Suhai, R. Scholz, A self-consistent charge density-functional based tight-binding method for predictive materials simulations in physics, chemistry and biology, *Phys. Stat. Sol. B* **217** (2000) 41-62.
10. M. Elstner, Density functional theory and the approximate SCC-DFTB method: performance and challenges, Lecture Note on the 7th Thai Summer School of Computational Chemistry, 11-14 October 2010.
11. C. J. Cramer, Essentials of computational chemistry: theories and models, John Wiley & Sons Ltd. 2004.
12. W. Koch, M. C. Holthausen, A chemist's guide to density functional theory, Wiley-VCH Verlag GmbH, 2001.

13. A. F. Oliveira, G. Seifert, T. Heine, H. A. Duarte, Density-functional based tight-binding: an approximate DFT method, *J. Braz. Chem. Soc.* **20** (2009) 1193-1205.
14. T. Frauenheim, G. Seifert, M. Elstner, T. Niehaus, C. Kohler, M. Amkreutz, M. Sternberg, Z. Hajnal, A. D. Carlo, S. Suhai, Atomistic simulations of complex materials: ground-state and excited-state properties, *J. Phys.: Condens. Matter* **14** (2002) 3015–3047.
15. P. Koskinen, V. Mäkinen, Density-functional tight-binding for beginners, *Comput. Mater. Sci.* **47** (2009) 237–253.
16. G. Dolgonos, B. Aradi, N. H. Moreira, T. Frauenheim, An improved self-consistent-charge density-functional tight-binding (SCC-DFTB) set of parameters for simulation of bulk and molecular systems involving titanium, *J. Chem. Theory Comput.* **6** (2010) 266–278.
17. M. Elstner, D. Porezag, G. Jungnickel, J. Elsner, M. Haugk, Th. Frauenheim, S. Suhai, G. Seifert, Self-consistent-charge density-functional tight-binding method for simulations of complex materials properties, *Phys. Rev. B* **58** (1998) 7260-7268.
18. G. Seifert, H. Eschrig, W. Bieger, *Z. Phys. Chemie (Leipzig)* **267** (1986) 529-539.
19. S. Iijima, Helical microtubules of graphitic carbon, *Nature (London)* **354** (1991) 56-58.
20. S. Iijima, T. Ichihashi, Single-shell carbon nanotubes of 1-nm diameter, *Nature (London)* **363** (1993) 603-605.
21. D. S. Bethune, C. H. Kiang, M. S. De Vries, G. Gorman, R. Savoy, J. Vazquez, R. Beyers, Cobalt-catalysed growth of carbon nanotubes with single-atomic-layer walls, *Nature (London)* **363** (1993) 605-607.
22. N. Hamada, S. Sawada, A. Oshiyama, New one-dimensional conductors: graphitic microtubules, *Phys. Rev. Lett.* **68** (1992) 1579–1582.
23. R. Saito, M. Fujita, G. Dresselhaus, M. S. Dresselhaus, Electronic structure of graphene tubules based on C60, *Phys. Rev. B* **46** (1992) 1804–1811.
24. R. Saito, M. Fujita, G. Dresselhaus, M. S. Dresselhaus, Electronic structure of chiral graphene tubule, *Appl. Phys. Lett.* **60** (1992) 2204–2206.

25. J. W. G. Wildoer, L. C. Venema, A. G. Rinzler, R. E. Smalley, C. Dekker, Electronic structure of atomically resolved carbon nanotubes, *Nature* **391** (1998) 59–62.
26. T. W. Odom, J. L. Huang, P. Kim, C. M. Lieber, Atomic structure and electronic properties of single-walled carbon nanotubes, *Nature* **391** (1998) 62–64.
27. M. Burghard, Electronic and vibrational properties of chemically modified single-wall carbon nanotubes, *Surf. Sci. Rep.* **58** (2005) 1–109.
28. C. Wongchoosuk, Molecular design of functionalized carbon nanotubes, M.Sc. Thesis 2007, Mahidol University.
29. M. Terrones, Science and technology of the twenty-first century: synthesis, properties, and applications of carbon nanotubes, *Annu. Rev. Mater. Res.* **33** (2003) 419–501.
30. M. S. Dresselhaus, G. Dresselhaus, A. Jorio, Unusual properties and structure of carbon nanotubes, *Annu. Rev. Mater. Res.* **34** (2004) 247–278.
31. H. J. Shen, MD simulations on the melting and compression of C, SiC and Si nanotubes, *J. Mater. Sci.* **42** (2007) 6382–6387.
32. M. W. Zhao, Y. Y. Xia, R. Q. Zhang, S. T. Lee, Manipulating the electronic structures of silicon carbide nanotubes by selected hydrogenation, *J. Chem. Phys.* **122** (2005) 214707.
33. G. Mpourmpakis, G. E. Froudakis, G. P. Lithoxoos, J. Samios, SiC Nanotubes: A novel material for hydrogen storage, *Nano Lett.* **6** (2006) 1581–1583.
34. C. Pham-Huu, N. Keller, G. Ehret, M. J. Ledoux, The first preparation of silicon carbide nanotubes by shape memory synthesis and their catalytic potential, *J. Catal.* **200** (2001) 400–410.
35. Y. Zhang, T. Ichihashi, E. Landree, F. Nihey, S. Iijima, Heterostructures of single-walled carbon nanotubes and carbide nanorods, *Science* **285** (1999) 1719–1722.
36. X. H. Sun, C. P. Li, W. K. Wong, N. B. Wong, C. S. Lee, S. T. Lee, B. K. Teo, Formation of silicon carbide nanotubes and nanowires via

- reaction of silicon (from disproportionation of silicon monoxide) with carbon nanotubes, *J. Am. Chem. Soc.* **124** (2002) 14464–14471.
37. N. Keller, C. P. Huu, G. Ehret, V. Keller, M. J. Ledoux, Synthesis and characterisation of medium surface area silicon carbide nanotubes, *Carbon* **41** (2003) 2131-2139.
38. T. Taguchi, N. Igawa, H. Yamamoto, Synthesis of silicon carbide nanotubes, *J. Am. Ceram. Soc.* **88** (2005) 459-461.
39. L. Z. Pei, Y. H. Tang, Y. W. Chen, C. Guo, X. X. Li, Y. Yuan, Y. Zhang, Preparation of silicon carbide nanotubes by hydrothermal method, *J. Appl. Phys.* **99** (2006) 114306.
40. J. Q. Hu, Y. Bando, J. H. Zhan, D. Golberg, Fabrication of ZnS/SiC nanocables, SiC-shelled ZnS nanoribbons (and sheets), and SiC nanotubes (and tubes), *Appl. Phys. Lett.* **85** (2004) 2932–2934.
41. J. Zhou, J. Liu, R. Yang, C. Lao, P. Gao, R. Tummala, N. S. Xu, Z. L. Wang, SiC-shell nanostructures fabricated by replicating ZnO nano-objects: a technique for producing hollow nanostructures of desired shape, *Small* **2** (2006) 1344-1347.
42. J. Zhou, M. Zhou, Z. Chen, Z. Zhang, C. Chen, R. Li, X. Gao, E. Xie, SiC nanotubes arrays fabricated by sputtering using electrospun PVP nanofiber as emplates, *Surf. Coat. Technol.* **203** (2009) 3219-3223.
43. M. Menon, E. Richter, A. Mavrandonakis, G. Froudakis, A. N. Andriotis, Structure and stability of SiC nanotubes, *Phys. Rev. B* **69** (2004) 115322.
44. M. Zhao, Y. Xia, F. Li, R. Q. Zhang, S. T. Lee, Strain energy and electronic structures of silicon carbide nanotubes: density functional calculations, *Phys. Rev. B* **71** (2005) 085312.
45. R. Moradian, S. Behzad, R. Chegel, Ab initio density functional theory investigation of structural and electronic properties of silicon carbide nanotube bundles, *Physica B* **403** (2008) 3623-3626.
46. A. Mavrandonakis, G. E. Froudakis, M. Schnell, M. Mu1hlhaluser, From pure carbon to silicon-carbon nanotubes: an ab-initio study, *Nano Lett.* **3** (2003) 1481-1484.

47. S. L. Lair, W. C. Herndon, L. E. Murr, Stability comparison of simulated double-walled carbon nanotube structures, *Carbon* **46** (2008) 2083–2095.
48. Y. Ohta, Y. Okamoto, S. Irle, K. Morokuma, Density-functional tight-binding molecular dynamics simulations of SWCNT growth by surface carbon diffusion on an iron cluster, *Carbon* **47** (2009) 1270–1275.
49. Y. Ohta, Y. Okamoto, S. Irle, K. Morokuma, Single-walled carbon nanotube growth from a cap fragment on an iron nanoparticle: density-functional tight-binding molecular dynamics simulations, *Phys. Rev. B* **79** (2009) 195415.
50. S. Nose, A unified formulation of the constant temperature molecular-dynamics methods, *J. Chem. Phys.* **81** (1984) 511–519.
51. <http://www.nanowerk.com/>
52. R. S. Wanger, W. C. Ellis, Vapor-liquid-solid mechanism of single crystal growth, *Applied Phys. Lett.*, **4** (1964) 89-89.
53. N. S. Ramgir, K. Subannajui, Y. Yang, R. Grimm, R. Michiels, M. Zacharias, Reactive VLS and the reversible switching between VS and VLS growth modes for ZnO nanowire growth, *J. Phys. Chem. C* **114** (2010) 10323–10329.
54. M. Zacharias, H. J. Fan, From ordered arrays of nanowires to controlled solid state reactions, *Adv. Solid State Phys.* **48** (2009) 3-12.
55. Y. Huang, X. Duan, Y. Cui, L. J. Lauhon, K. H. Kim, C. M. Lieber, Logic gates and computation from assembled nanowire building blocks, *Science* **294** (2001) 1313-1317.
56. H. J. Fan, P. Werner, M. Zacharias, Semiconductor nanowires: from self-organization to patterned growth, *Small* **2** (2006) 700-717.
57. V. Avrutin, D. J. Silversmith, H. Morkoc, Doping asymmetry problem in ZnO: current status and outlook, *Proc. of the IEEE* **98** (2010) 1269-1280.
58. P. Yang, H. Yan, S. Mao, R. Russo, J. Johnson, R. Saykally, N. Morris, J. Pham, R. He, H. J. Choi, Controlled growth of ZnO nanowires and their optical properties, *Adv. Funct. Mater.* **12** (2002) 323-331.

59. Z. L. Wang, X. Y. Kong, Y. Ding, P. Gao, W. L. Hughes, R. Yang, Y. Zhang, Semiconducting and piezoelectric oxide nanostructures induced by polar surfaces, *Adv. Funct. Mater.* **14** (2004) 943-956.
60. F. Xu, K. Yu, G. D. Li, Q. Li, Z. Q. Zhu, Synthesis and field emission of four kinds of ZnO nanostructures: nanosleeve- fishes, radial nanowire arrays, nanocombs and nanoflowers, *Nanotechnology* **17** (2006) 2855-2859.
61. Z. L. Wang, Novel nanostructures of ZnO for nanoscale photonics, optoelectronics, piezoelectricity, and sensing, *Appl. Phys. A* **88** (2007) 7-15.
62. H. J. Fan, M. J. Zacharias, Manipulation of crawling growth for the formation of sub-millimeter long ZnO nanowalls, *Mater. Sci. Technol.* **24** (2008) 589-593.
63. A. Colli, A. Fasoli, S. Hofmann, C. Ducati, J. Robertson, A. C. Ferrari, Deterministic shape-selective synthesis of nanowires nanoribbons and nanosaws by steady-state vapour-transport, *Nanotechnology* **17** (2006) 1046-1051.
64. I. Amarillio-Burshtein, S. Tamir, Y. Lifshitz, Growth modes of ZnO nanostructures from laser ablation, *Appl. Phys. Lett.* **96** (2010) 103104.
65. A. Fasoli, A. Colli, S. Hofmann, C. Ducati, J. Robertson, A. C. Ferrari, Shape-selective synthesis of II–VI semiconductor nanowires, *Phys. Stat. Sol. (b)* **243** (2006) 3301-3305.
66. Rao, Y. K. Stoichiometry and thermodynamics of metallurgical processes: Cambridge University Press: Cambridge, 1985.
67. D. S. Kim, R. Scholz, U. Gösele, M. Zacharias, Gold at the root or at the tip of ZnO nanowires: a model, *Small* **4** (2008) 1615-1619.
68. H. Wang, G. S. Fischman, Role of liquid droplet surface diffusion in the vapor - liquid - solid whisker growth mechanism, *J. Appl. Phys.* **76** (1994) 1557-1562.
69. <http://www.figarosensor.com/products/general.pdf>
70. http://en.wikipedia.org/wiki/Thermal_oxidation

71. http://en.wikipedia.org/wiki/Electron_beam_physical_vapor_deposition
72. H. Gong, J. Q. Hu, J. H. Wang, C. H. Ong, F. R. Zhu, Nano-crystalline Cu-doped ZnO thin film gas sensor for CO, *Sens. Actuat. B* **115** (2006) 247–251.
73. S. T. Shishiyanu, T. S. Shishiyanu, O. I. Lupan, Sensing characteristics of tin-doped ZnO thin films as NO₂ gas sensor, *Sens. Actuat. B* **107** (2005) 379–386.
74. Q. Zhang, C. Xie, S. Zhang, A. Wang, B. Zhu, L. Wang, Z. Yang, Identification and pattern recognition analysis of Chinese liquors by doped nano ZnO gas sensor array, *Sens. Actuat. B* **110** (2005) 370–376.
75. D. F. Paraguay, M. M. Miki-Yoshida, J. Morales, J. Solis, L. W. Estrada, Influence of Al, In, Cu, Fe and Sn dopants on the response of thin film ZnO gas sensor to ethanol vapour, *Thin Solid Films* **373** (2000) 137–140.
76. B. L. Zhu, C. S. Xie, J. Wu, D. W. Zeng, A. H. Wang, X. Z. Zhao, Influence of Sb, In and Bi dopants on the response of ZnO thick films to VOCs, *Mater. Chem. Phys.* **96** (2006) 459–465.
77. J. Xu, J. Han, Y. Zhang, Y. Sun, B. Xie, Studies on alcohol sensing mechanism of ZnO based gas sensors, *Sens. Actuat. B* **132** (2008) 334–339.
78. N. V. Russell, A. V. Chadwick, A. Wilson, Nanocrystalline nickel doped zinc oxide gas sensors, *Nucl. Instrum. Meth. B* **97** (1995) 575–578.
79. M. Haruta, Catalysis of gold nanoparticles deposited on metal oxides, *Cattech* **6** (2002) 102–115.
80. G. C. Bond, D. T. Thompson, Catalysis by gold, *Catal. Rev.* **41** (1999) 319–388.
81. J. Edwards, P. Landon, A. F. Carley, A. A. Herzing, M. Watanabe, C. J. Kiely, G. J. Hutchings, Nanocrystalline gold and gold–palladium as effective catalysts for selective oxidation, *J. Mater. Res.* **22** (2007) 831–837.
82. M. Haruta, Nanoparticulate gold catalysts for low-temperature CO oxidation, *J. New. Mater. Electrochem. Syst.* **7** (2004) 163–172.

83. A. Tubtimtae, S. Choopun, A. Gardchareon, P. Mangkornong, N. Mangkornong, Ethanol sensor based on Au-doped ZnO nanostructures, *Proc. Of IEEE-NEMS* (2007) 207–210.
84. N. Hongstith, C. Viriyaworasakul, P. Mangkornong, N. Mangkornong, S. Choopun, Ethanol sensor based on ZnO and Au-doped ZnO nanowires, *Ceram. Int.* **34** (2008) 823–826.
85. S. Choopun, N. Hongstith, P. Mangkornong, N. Mangkornong, Zinc oxide nanobelts by RF sputtering for ethanol sensor, *Physica E* **39** (2007) 53–56.
86. B. Y. Wei, M. C. Hsu, P. G. Su, H. M. Lin, R. J. Wu, H. J. Lai, A novel SnO₂ gas sensor doped with carbon nanotubes operating at room temperature, *Sens. Actuators B* **101** (2004) 81–89.
87. E. H. Espinosa, R. Ionescu, B. Chambon, G. Bedis, E. Sotter, C. Bittencourt, A. Felten, J. J. Pireaux, X. Correig, E. Llobet, Hybrid metal oxide and multiwall carbon nanotube films for low temperature gas sensing, *Sens. Actuators B* **127** (2007) 137–142.
88. N.V. Hieu, L.T.B. Thuya, N.D. Chien, Highly sensitive thin film NH₃ gas sensor operating at room temperature based on SnO₂/MWCNTs composite, *Sens. Actuators B* **129** (2008) 888–895.
89. J. Gong, J. Sun, Q. Chen, Micromachined sol–gel carbon nanotube/SnO₂ nanocomposite hydrogen sensor, *Sens. Actuators B* **130** (2008) 829–835.
90. J. Wang, L. Liu, S. Y. Cong, J. Q. Qi, B. K. Xu, An enrichment method to detect low concentration formaldehyde, *Sens. Actuators B* **134** (2008) 1010–1015.
91. J. Liu, Z. Guo, F. Meng, Y. Jia, J. Liu, A novel antimony-carbon nanotube-tin oxide thin film: carbon nanotubes as growth guider and energy buffer. Application for indoor air pollutants gas sensor, *J. Phys. Chem. C* **112** (2008) 6119–6125.
92. A. Wisitsoraat, A. Tuantranont, C. Thanachayanont, V. Patthanasettakul, P. Singjai, Electron beam evaporated carbon nanotube dispersed SnO₂ thin film gas sensor, *J. Electroceram.* **17** (2006) 45–49.

93. A. Wisitsoraat, A. Tuantranont, V. Patthanasettakul, T. Lomas, P. Chindaudom, Ion-assisted e-beam evaporated gas sensor for environmental monitoring, *Sci. Technol. Adv. Mater.* **6** (2005) 261–265.
94. H. Liu, G. Cheng, R. Zheng, Y. Zhao, C. Liang, Influence of synthesis process on preparation and properties of Ni/CNT catalyst, *Diamond Relat. Mater.* **15** (2006) 15–21.
95. S. Majumder, S. Hussain, S. N. Das, R. B. Bhar, A. K. Pal, Silicon doped SnO₂ films for liquid petroleum gas sensor, *Vacuum* **82** (2008) 760–770.
96. G. Korotcenkov, S. D. Han, J. R. Stetter, Review of electrochemical hydrogen sensors, *Chem. Rev.* **109** (2009) 1402–1433.
97. P. Moriarty, D. Honnery, Hydrogen's role in an uncertain energy future, *Int. J. Hydrogen. Energ.* **34** (2009) 31–39.
98. M. Momirlan, T. N. Veziroglu, The properties of hydrogen as fuel tomorrow in sustainable energy system for a cleaner planet, *Int. J. Hydrogen. Energ.* **30** (2005) 795–802.
99. B. Árnason, T. I. Sigfússon, Iceland—A future hydrogen economy, *Int. J. Hydrogen. Energ.* **25** (2000) 389–394.
100. M. N. Carcassi, F. Fineschi, Deflagrations of H₂-air and CH₄-air lean mixtures in a vented multi-compartment environment, *Energy* **30** (2005) 1439–1451.
101. M. Penza, M. A. Tagliente, L. Mirengi, C. Gerardi, C. Martucci, G. Cassano, Tungsten trioxide (WO₃) sputtered thin films for a NO_x gas sensor. *Sens. Actuat. B* **50** (1998) 9–18.
102. X. Wang, N. Miura, N. Yamazoe, Study of WO₃-based sensing materials for NH₃ and NO detection, *Sens. Actuat. B* **66** (2000) 74–76.
103. T. S. Kim, T. B. Kim, K. S. Yoo, G. S. Sung, H. J. Jung, Sensing characteristics of dc reactive sputtered WO₃ thin films as an NO_x gas sensor, *Sens. Actuat. B* **62** (2000) 102–108.
104. K. M. Sawicka, A. K. Prasad, P. I. Gouma, Metal oxide nanowires for use in chemical sensing applications, *Sens. Lett.* **3** (2005) 31–35.

105. W. H. Tao, C. H. Tsai, H₂S sensing properties of noble metal doped WO₃ thin film sensor fabricated by micromachining, *Sens. Actuat. B* **81** (2002) 237-247.
106. B. Frühberger, M. Grunze, D. J. Dwyer, Surface chemistry of H₂S-sensitive tungsten oxide films, *Sens. Actuat. B* **31** (1996) 167-174.
107. A. Hoel, L. F. Reyes, P. Heszler, V. Lantto, C. G. Granqvist, Nanomaterials for environmental applications: Novel WO₃-based gas sensors made by advanced gas deposition, *Curr. Appl. Phys.* **4** (2004) 547-553.
108. R. Ionescu, A. Hoel, C. G. Granqvist, E. Llobet, P. Heszler, Low-level detection of ethanol and H₂S with temperature-modulated WO₃ nanoparticle gas sensors, *Sens. Actuat. B* **104** (2005) 132-139.
109. X. Li, G. Zhang, F. Cheng, B. Guo, J. Chen, Synthesis, characterization, and gas-sensor application of WO₃ nanocuboids, *J. Electrochem. Soc.* **153** (2006) 133-137.
110. Y. Xu, Z. Tang, Z. Zhang, Y. Ji, Z. Zhou, Large-scale hydrothermal synthesis of tungsten trioxide nanowires and their gas sensing properties, *Sens. Lett.* **6** (2008) 938-941.
111. G. Neri, G. Micali, A. Bonavita, S. Ipsale, G. Rizzo, M. Niederberger, N. Pinna, Tungsten oxide nanowires-based ammonia gas sensors, *Sens. Lett.* **6** (2008) 590-595.
112. E. Llobet, G. Molas, P. Molinàs, J. Calderer, X. Vilanova, J. Brezmes, J. E. Sueiras, X. Correig, Fabrication of highly selective tungsten oxide ammonia sensors, *J. Electrochem. Soc.* **147** (2000) 776-779.
113. C. Balázsia, L. Wang, E. O. Zayim, I. M. Szilágyid, K. Sedlackováe, J. Pfeifera, A. L. Tótha, P. I. Goumab, Nanosize hexagonal tungsten oxide for gas sensing applications, *J. Eur. Ceram. Soc.* **28** (2008) 913-917.
114. U. Wang, J. Pfeifer, C. Balazsi, P. I. Gouma, Synthesis and sensing properties to NH₃ of hexagonal WO₃ metastable nanopowders, *Mater. Manuf. Process.* **22** (2007) 773-776.
115. O. Berger, T. Hoffmann, W. J. Fischer, V. Melev, Tungsten-oxide thin films as novel materials with high sensitivity and selectivity to NO₂, O₃, and

- H₂S. Part II: Application as gas sensors, *J. Mater. Sci.: Mater. Electron.* **15** (2004) 483-493.
116. V. Aroutiounian, Metal oxide hydrogen, oxygen, and carbon monoxide sensors for hydrogen setups and cells, *Int. J. Hydrogen. Energ.* **32** (2007) 1145-1158.
117. A. Ahmad, J. Walsh, Development of WO₃-based thick-film hydrogen sensors, *ECS Trans.* **3** (2006) 141-152.
118. S. J. Ippolito, S. Kandasamy, K. Kalantar-zadeh, W. Wlodarski, Hydrogen sensing characteristics of WO₃ thin film conductometric sensors activated by Pt and Au catalysts, *Sens. Actuat. B* **108** (2005) 154-158.
119. W. C. Hsu, C. C. Chan, C. H. Peng, C. C. Chang, Hydrogen sensing characteristics of an electrodeposited WO₃ thin film gasochromic sensor activated by Pt catalyst, *Thin Solid Films* **516** (2007) 407-411.
120. S. Fardindoost, A. Irajizad, F. Rahimi, R. Ghasempour, Pd doped WO₃ films prepared by sol-gel process for hydrogen sensing, *Int. J. Hydrogen. Energ.* **35** (2010) 854-860.
121. H. Nakagawa, N. Yamamoto, S. Okazaki, T. Chinzei, S. Asakura, A room-temperature operated hydrogen leak sensor, *Sens. Actuat. B* **93** (2003) 468-474.
122. P. Samarasekara, Hydrogen and methane gas sensors synthesis of multi-walled carbon nanotubes, *Chin. J. Phys.* **47** (2009) 361-369.
123. L. Zhu, Y. Xiu, D. W. Hess, C. P. Wong, Aligned carbon nanotube stacks by water-assisted selective etching, *Nano Lett.* **5** (2005) 2641-2645.
124. C. Wongchoosuk, A. Wisitsoraat, A. Tuantranont, T. Kerdcharoen, Portable electronic nose based on carbon nanotube-SnO₂ gas sensors and its application for detection of methanol contamination in whiskeys, *Sens. Actuat. B* **147** (2010) 392-399.
125. Z. A. Ansari, S. G. Ansari, T. Ko, J. H. Oh, Effect of MoO₃ doping and grain size on SnO₂-enhancement of sensitivity and selectivity for CO and H₂ gas sensing, *Sens. Actuat. B* **87** (2002) 105-114.

126. D. S. Lee, K. H. Nam, D. D. Lee, Effect of substrate on NO₂-sensing properties of WO₃ thin film gas sensors, *Thin Solid Films* **375** (2000) 142-146.
127. O. M. Hussain, A. S. Swapnasmitha, J. John, R. Pinto, Structure and morphology of laser-ablated WO₃ thin films, *Appl. Phys. A: Mater. Sci. Process.* **81** (2005) 1291-1297.
128. P. V. Ashrit, Dry lithiation study of nanocrystalline, polycrystalline and amorphous tungsten trioxide thin-films, *Thin Solid Films* **385** (2001) 81-88.
129. V. R. Shinde, T. P. Gujar, C. D. Lokhande, LPG sensing properties of ZnO films prepared by spray pyrolysis method: Effect of molarity of precursor solution, *Sens. Actuat. B* **120** (2007) 551-559.
130. Y. Zeng, T. Zhang, L. Wang, M. Kang, H. Fan, R. Wang, Y. He, Enhanced toluene sensing characteristics of TiO₂-doped flowerlike ZnO nanostructures. *Sens. Actuat. B* **140** (2009) 73-78.
131. P. P. Sahay, R. K. Nath, Al-doped zinc oxide thin films for liquid petroleum gas (LPG) sensors, *Sens. Actuat. B* **133** (2008) 222-227.
132. Y. X. Liang, Y. J. Chen, T. H. Wang, Low-resistance gas sensors fabricated from multiwalled carbon nanotubes coated with a thin tin oxide layer, *Appl. Phys. Lett.* **85** (2004) 666-668.
133. C. Bittencourt, A. Felten, E. H. Espinosa, R. Ionescu, E. Llobet, X. Correig, J. J. Pireaux, WO₃ films modified with functionalised multi-wall carbon nanotubes: Morphological, compositional and gas response studies, *Sens. Actuat. B* **115** (2006) 33-41.
134. G. Sakai, N. Matsunaga, K. Shimano, N. Yamazoe, Theory of gas-diffusion controlled sensitivity for thin film semiconductor gas sensor, *Sens. Actuat. B* **80** (2001) 125-131.
135. N. V. Hieu, N. A. P. Duc, T. Trung, M. A. Tuan, N. D. Chien, Gas-sensing properties of tin oxide doped with metal oxides and carbon nanotubes: A competitive sensor for ethanol and liquid petroleum gas, *Sens. Actuat. B* **144** (2010) 450-456.

136. B. Y. Wei, M. C. Hsu, P. G. Su, H. M. Lin, R. J. Wu, H. J. Lai, A novel SnO₂ gas sensor doped with carbon nanotubes operating at room temperature, *Sens. Actuat. B* **101** (2004) 81-89.
137. H. W. Cheong, M. J. Lee, Sensing characteristics and surface reaction mechanism of alcohol sensors based on doped SnO₂, *J. Ceram. Process. Res.* **7** (2006) 183-191.
138. O. Lupan, V. V. Ursaki, G. Chai, L. Chow, G. A. Emelchenko, I. M. Tiginyanu, A. N. Gruzintsev, A. N. Redkin, Selective hydrogen gas nanosensor using individual ZnO nanowire with fast response at room temperature, *Sens. Actuat. B* **144** (2010) 56-66.
139. J. W. Gardner, P. N. Bartlett, A brief history of electronic noses, *Sens. Actuat. B* **18** (1994) 211-220.
140. <http://www.scribd.com/doc/20473653/Electronic-Nose>
141. H. V. Shurmer, J. W. Gardner, H. T. Chang, The application of discrimination techniques to alcohols and tobaccos using tin-oxide sensors, *Sens. Actuat. B* **18** (1989) 361-371.
142. C. Wongchoosuk, M. Lutz, T. Kerdcharoen, Correction of humidity effect for detection of human body odor, Proceedings of the 5th ECTI-CON **2** (2008) 845-848.
143. F. D. Francesco, M. Falcitelli, L. Marano, G. Pioggia, A radially symmetric measurement chamber for electronic noses, *Sens. Actuat. B* **105** (2005) 295-303.
144. C. Wongchoosuk, S. Choopun, A. Tuantranont, T. Kerdcharoen, Au-doped zinc oxide nanostructure sensors for detection and discrimination of volatile organic compounds, *Mater. Res. Innovat.* **13** (2009) 185-188.
145. A. H. Nuttall, Some windows with very good sidelobe behavior, *IEEE Trans. Acoust. Speech Sign. Process.* **29** (1981) 84-91.
146. I. T. Jolliffe, Principal Component Analysis, Springer, 2002.
147. S. Roussel, G. Forsberg, V. Steinmetz, P. Grenier, V. Bellon-Maurel, Optimisation of electronic nose measurement. Part I. Methodology of output feature selection, *J. Food Eng.* **37** (1998) 207-222.

148. S. Zhang, C. Xie, D. Zeng, Q. Zhang, H. Li, Z. Bi, A feature extraction method and a sampling system for fast recognition of flammable liquids with a portable E-nose, *Sens. Actuat. B* **124** (2007) 437–443.
149. N. Barié, M. Bücking, M. Rapp, A novel electronic nose based on miniaturized SAW sensor arrays coupled with SPME enhanced headspace-analysis and its use for rapid determination of volatile organic compounds in food quality monitoring, *Sens. Actuat. B* **114** (2006) 482–488.
150. J. S. Vestergaard, M. Martens, P. Turkki, Application of an electronic nose system for prediction of sensory quality changes of a meat product (pizza topping) during storage, *LWT* **40** (2007) 1095–1101.
151. M. Vinaixa, A. Vergara, C. Duran, E. Llobet, C. Badia, J. Brezmes, X. Vilanova, X. Correig, Fast detection of rancidity in potato crisps using E-noses based on mass spectrometry or gas sensors, *Sens. Actuat. B* **106** (2005) 67–75.
152. S. Panigrahi, S. Balasubramanian, H. Gu, C. M. Logue, M. Marchello, Design and development of a metal oxide based electronic nose for spoilage classification of beef, *Sens. Actuat. B* **119** (2006) 2–14.
153. N. E. Barbri, E. Llobet, N. E. Bari, X. Correig, B. Bouchikhi, Electronic nose based on metal oxide semiconductor sensors as an alternative technique for the spoilage classification of red meat, *Sensors* **8** (2008) 142–156.
154. M. P. Martí, O. Busto, J. Guasch, R. Boqué, Electronic noses in the quality control of alcoholic beverages, *Trends Anal. Chem.* **24** (2005) 57–66.
155. H. Yu, J. Wang, Discrimination of LongJing green-tea grade by electronic nose, *Sens. Actuat. B* **122** (2007) 134–140.
156. M. García, M. Aleixandre, J. Gutiérrez, M. C. Horrillo, Electronic nose for wine discrimination, *Sens. Actuat. B* **113** (2006) 911–916.
157. R. Dutta, E. L. Hines, J. W. Gardner, K. R. Kashwan, M. Bhuyan, Tea quality prediction using a tin oxide-based electronic nose: an artificial intelligence approach, *Sens. Actuat. B* **94** (2003) 228–237.

158. E. Scorsone, A. M. Pisanelli, K. C. Persaud, Development of an electronic nose for fire detection, *Sens. Actuat. B* **116** (2006) 55–61.
159. S. Zhang, C. Xie, D. Zeng, Q. Zhang, H. Li, Z. Bi, A feature extraction method and a sampling system for fast recognition of flammable liquids with a portable E-nose, *Sens. Actuat. B* **124** (2007) 437–443.
160. H. Zhou, M. L. Homer, A. V. Shevade, M. A. Ryan, Nonlinear least-squares based method for identifying and quantifying single and mixed contaminants in air with an electronic nose, *Sensors* **6** (2006) 1–18.
161. R. M. Negri, S. Reich, Identification of pollutant gases and its concentrations with a multisensor array, *Sens. Actuat. B* **75** (2001) 172–178.
162. H. P. Chan, C. Lewis, P. S. Thomas, Exhaled breath analysis: novel approach for early detection of lung cancer, *Lung Cancer* **63** (2009) 164–168.
163. C. W. Hanson, Method and system of diagnosing intrapulmonary infection using an electronic nose, *US patent 6620109* (2003).
164. A. Pavlou, A. P. F. Turner, H. Barr, Diagnosis of gastric and lung disorders, *WO Patent 032091* (2000).
165. A. P. F. Turner, N. Magan, Electronic noses and disease diagnostics, *Nature Rev. Microbiol.* **2** (2004) 161–166.
166. X. Xu, F. Tian, S. X. Yang, Q. Li, J. Yan, J. Ma, A solid trap and thermal desorption system with application to a medical electronic nose, *Sensors* **8** (2008) 6885–6898.
167. R. L. Doty, M. Ford, G. Preti, G. R. Huggins, Changes in the intensity and pleasantness of human vaginal odors during the menstrual cycle, *Science* **190** (1975) 1316–1318.
168. D. Chen, J. Haviland-Jones, Human olfactory communication of emotion, *Percept. Mot. Skills* **91** (2000) 771–781.
169. K. Delac, M. Grgic, A survey of biometric recognition methods, 46th International Symposium Electronics in Marine (*ELMAR-2004*), Zadar, Croatia, June 16–18 (2004) 184–193.

170. C. D. Natale, A. Mantini, A. Macagnano, D. Antuzzi, R. Paolesse, A. D'Amico, Electronic nose analysis of urine samples containing blood, *Phys. Meas.* **20** (1999) 377–384.
171. M. Phillips, R. N. Cataneo, A. R. C. Cummin, A. J. Gagliardi, K. Gleeson, J. Greenberg, R. A. Maxfield, W. N. Rom, Detection of lung cancer with volatile markers in the breath, *Chest* **123** (2003) 2115–2123.
172. M. Phillips, R. N. Cataneo, B. A. Ditkoff, P. Fisher, J. Greenberg, R. Gunawardena, C. S. Kwon, F. Rahbari-Oskoui, C. Wong, Volatile markers of breast cancer in the breath, *Breast J.* **9** (2003) 184–191.
173. Z. Jin, T. Shimbo, Y. Hosoe, T. Oyabu, Breath odor characteristics after drinking and identification of sake quantity, *Sens. Actuat. B* **108** (2005) 265–270.
174. C. D. Natale, A. Macagnano, R. Paolesse, E. Tarizzo, A. Mantini, A. D'Amico, Human skin odor analysis by means of an electronic nose, *Sens. Actuat. B* **65** (2000) 216–219.
175. D. J. Penn, E. Oberzaucher, K. Grammer, G. Fischer, H. A. Soini, D. Wiesler, M. V. Novotny, S. J. Dixon, Y. Xu, R. G. Brereton, Individual and gender fingerprints in human body odour, *J. R. Soc. Interf.* **4** (2007) 331–340.
176. T. C. Pearce, S. S. Schiffman, H. T. Nagle, J. W. Gardner, Handbook of machine olfaction, electronic nose technology, Wiley-VCH: Weinheim, Germany, 2002.
177. A. M. Curran, S. I. Rabin, P. A. Prada, K. G. Furton, Comparison of the volatile organic compounds present in human odor using spme-GC/MS, *J. Chem. Ecol.* **31** (2005) 1607–1619.
178. K. H. Kim, S. Y. Park, A comparative analysis of malodor samples between direct (olfactometry) and indirect (instrumental) methods, *Atmos. Environ.* **42** (2008) 5061–5070.
179. J. A. Nicell, Expressions to relate population responses to odor concentration, *Atmos. Environ.* **37** (2003) 4955–4964.
180. P. Henshaw, J. Nicell, A. Sikdar, Parameters for the assessment of odour impacts on communities, *Atmos. Environ.* **40** (2006) 1016–1029.

181. T. Akutsu, K. Sekiguchi, T. Ohmori, K. Sakurada, Individual comparisons of the levels of (E)-3-Methyl-2-Hexenoic acid, an axillary odor-related compound, in Japanese, *Chem. Senses* **31** (2006) 557–563.
182. A. Natsch, H. Gfeller, P. Gygax, J. Schmid, G. Acuna, A specific bacterial aminoacylase cleaves odorant precursors secreted in the human axilla, *J. Biol. Chem.* **278** (2003) 5718–5727.
183. Y. Hasegawa, M. Yabuki, M. Matsukane, Identification of new odoriferous compounds in human axillary sweat, *Chem. Biodiv.* **1** (2004) 2042–2050.
184. D. C. Hooper, G. A. Johnson, D. Peter, Detergent product containing deodorant compositions, *US Patent 4322308*, 1982.
185. J. E. Amoore, Specific anosmia: a clue to the olfactory code, *Nature* **214** (1967) 1095–1098.
186. J. J. Leyden, K. J. Mcginley, E. Hölzle, J. N. Labows, A. M. Kligman, The microbiology of the human axilla and its relationship to axillary odor, *J. Invest. Dermatol.* **77** (1981) 413–416.
187. D. C. Hooper, G. A. Johnson, D. Peter, Deodorant compositions, *US Patent 4278658*, 1981.
188. B. Schoutena, B. Jacobs, Biometrics and their use in E-passports, *Image Vision Comput.* **27** (2009) 305–312.
189. A. J. Paine, A. D. Dayan, Defining a tolerable concentration of methanol in alcoholic drinks, *Hum. Exp. Toxicol.* **20** (2001) 563–568.

BIOGRAPHY

NAME	Mr. Chatchawal Wongchoosuk
DATE OF BIRTH	September 30, 1983
PLACE OF BIRTH	Songkhla, Thailand
INSTITUTIONS ATTENDED	Prince of Songkla University, 2001-2005: B.Sc. in Physics (First Class Honors) Mahidol University, 2005-2007: M.Sc. in Physics (International Program) Laboratory for Nanotechnology at the Institute of Microsystem Engineering (IMTEK), Albert Ludwigs University Freiburg, Germany. September 2009 – May 2010: Visiting Scholar Quantum Chemistry Group, Institute for Advanced Research and Department of Chemistry, Nagoya University, Nagoya, Japan June 2010 - September 2010: Visiting Scholar Mahidol University, 2007-2011: Ph.D. in Physics (International Program

SCOLARSHIPS

Teaching Assistant Scholarship

2005-2007

Institutional Strengthening Program from
Faculty of Science, Mahidol University

2007

Ph.D. scholarship under the program

“Strategic Frontier Research Network”

from the Commission on Higher

Education

2007-2011

PUBLICATIONS

1. C. Wongchoosuk, A. Wisitsoraat, D. Phokharatkul, A. Tuantranont, and T. Kerdcharoen, Tungsten Oxide Thin Film doped with Multi-walled Carbon Nanotubes for Hydrogen Gas Sensor, *Sensors* 2010, Vol. 10, pp. 7705-7715.

2. C. Wongchoosuk, A. Wisitsoraat, A. Tuantranont and T. Kerdcharoen, “Portable Electronic Nose Based on Carbon Nanotube-SnO₂ Gas Sensors: Feature Extraction Techniques and Its Application for Detection of Methanol Contamination in Whiskeys”, *Sensors and Actuators B: Chemical* 2010, Vol. 147, pp. 392-399.

3. C. Wongchoosuk, M. Lutz and T. Kerdcharoen, “Detection and classification of human body odor using an electronic nose”, *Sensors* 2009, Vol. 9, pp. 7234-7249.

4. C. Wongchoosuk, A. Udomvech and T. Kerdcharoen, "The geometrical and electronic structures of open-end fully functionalized single-walled carbon nanotubes", *Current Applied Physics* 2009, Vol. 9, pp. 352-358.

5. C. Wongchoosuk, S. Choopun, A. Tuantranont and T. Kerdcharoen, "Auroradoped Zinc Oxide Nanostructure Sensors for Detection and Discrimination of Volatile Organic Compounds", *Materials Research Innovation* 2009, Vol. 13, pp. 185-188.

6. C. Wongchoosuk, S. Kongsuk and T. Kerdcharoen, "Theoretical investigations on the tip-functionalized carbon nanotubes interacting with water", *International Journal of Nanoparticles* 2008, Vol. 1, pp. 136-151.

7. C. Wongchoosuk, K. Subannajui, A. Menzel, I. Amarilio-Burshtein, S. Tamir, Y. Lifshitz, and M. Zacharias, Controlled synthesis of ZnO nanostructures: The role of source and substrate temperatures, *Journal of Physical Chemistry C* (In Press).

PATENTS

1. Thai Patent Pending No. 0901001349: "Artificial Olfactory Device for people identification"

2. Thai Patent Pending No. 1001001840 "Briefcase Electronic Nose"

**INTERNATIONAL
CONFERENCE PROCEEDINGS**

1. C. Wongchoosuk and T. Kerdcharoen, Development of portable electronic nose and applications for monitoring armpit odor, The 3rd Biomedical Engineering International Conference (BMEICON 2010), 27-28 August 2010, Kyoto University, Kyoto, Japan.
2. A. Menzel , J. Ruhhammer, C. Wongchoosuk, K. Subannajui and M. Zacharias, ZnO nanowires for optical, electronic and sensor applications, IMTEK Postersession 2010, 24 June 2010, Building/Gebäude 101, University of Freiburg, Freiburg, Germany,
3. P. Lorwongtragool, C. Wongchoosuk, T. Kerdcharoen, Portable Artificial Nose System for Assessing Air Quality in Swine Buildings, Proceedings of the 2010 Electrical Engineering/Electronics, Computer, Telecommunications, and Information Technology International Conference (ECTI-2009), 19-21 May 2009, The Empress Hotel Convention Centre, Chiang Mai, Thailand. (IEEE Explore Database)
4. C. Karuwan, A. Wisitsoraat, D. Phokharatkul, T. Pogfai, C. Wongchoosuk, T. Kerdcharoen, A. Tuantranont, "Electronic Tongue: Plasma Functionalized Carbon Nanotube Electrochemical Sensor Array on

PDMS/Glass Chip”, IEEE International Symposium on Biomedical Engineering (IEEE ISBME 2009) , 14-18 December 2009, A Royal Méridien Hotel, Bangkok, Thailand. (IEEE Explore Database)

5. C. Wongchoosuk, A. Wisitsoraat, A. Tuantranont and T. Kerdcharoen, “Mobile Electronic Nose Based on Carbon Nanotube-SnO₂ Gas Sensors: Feature Extraction Techniques and Its Application”, Proceedings of the 2009 Electrical Engineering /Electronics, Computer, Telecommunications, and Information Technology International Conference (ECTI-2009), 6-9 May 2009, Ambassador City Jomtien Pattaya, Pattaya, Thailand. (IEEE Explore Database)

6. S. Lokavee, C. Wongchoosuk and T. Kerdcharoen, “Sidewall Functionalized Carbon Nanotubes: A Theoretical Study on the Effects of Carboxylic Group” Pure and Applied Chemistry International Conference (PACCON 2009), January 14-16, 2009, Amarin Lagoon Hotel, Phitsanulok, Thailand.

7. C. Wongchoosuk, M. Lutz, A. Tuantranont and T. Kerdcharoen, “James Bond Electronic Nose for Estimation of Thai Tea Aroma” International Conference on Tea Production and Tea Products, November 26-28, 2008, Mae Fah Luang University, Chiang Rai, Thailand.

8. C. Wongchoosuk, T. Techalertmanee, S. Sahasithiwat, A. Tuantranont and T. Kerdcharoen, "Discrimination of Thai alcoholic beverages using carbon black-polymer composite sensor array", The 4th International Conference on Technological Advances of Thin Films & Surface Coatings (ThinFilms 2008), July 13-16, 2008, Singapore.
9. C. Wongchoosuk, S. Choopun, A. Tuantranont and T. Kerdcharoen, "Au-doped zinc oxide nanostructure sensors for detection and discrimination of volatile organic compounds", The 2nd International Conference on Functional Materials and Devices (ICFMD 2008), June 16-19, 2008, Kuala Lumpur, Malaysia.
10. C. Wongchoosuk, M. Lutz and T. Kerdcharoen, "Correction of humidity effect for detection of human body odor", Proceedings of the 2008 Electrical Engineering/Electronics, Computer, Telecommunications, and Information Technology International Conference (ECTI-2008), May 14-17, 2008, Phuket, Thailand. (IEEE Explore Database)
11. C. Wongchoosuk, M. Lutz, A. Tuantranont and T. Kerdcharoen, "Development of the Hardware and Software for Human Body Odor Discrimination", The 5th International

Joint Conference on Computer Science and Software Engineering (JCSSE-2008), May 7-9, 2008, Kanchanaburi, Thailand.

12. C. Wongchoosuk, S. Choopun, A. Tuantranont and T. Kerdcharoen, "Portable electronic nose based on Au-doped ZnO nanostructure sensors for classification of Thai alcohols", First International Workshop on Nanotechnology and Application (IWNA 2007), November 15-17, 2007, Vung Tau, Vietnam.

13. C. Wongchoosuk, S. Krongsuk and T. Kerdcharoen, "First principles and MD simulation study of the interaction of functionalized carbon nanotubes with water molecules", Proceeding of the 7th IEEE International Conference on Nanotechnology (IEEE-NANO 2007), August 2-5, 2007, Hong Kong Convention & Exhibition Centre, Hong Kong, China. (IEEE Explore Database)

14. C. Wongchoosuk, S. Krongsuk and T. Kerdcharoen, "Computational molecular modeling and simulation of functionalized carbon nanotubes", Proceedings of the 2007 Electrical Engineering/Electronics, Computer, Telecommunications, and Information Technology International Conference (ECTI-2007), May 9-12. 2007, Mae Fah Luang University, Chiang Rai, Thailand.

15. C. Wongchoosuk, A. Udomvech and T. Kerdcharoen, “Open-ended functionalized single-walled carbon nanotubes: a quantum mechanics study of the effects of tubule length and functional groups”, the 1st International Conference on Applied Science (ICAS-2006), Nov, 5-7 2006, Vientiane, Laos.

**NATIONAL CONFERENCE
PROCEEDINGS**

1. C. Wongchoosuk, D. Phokharatkul, A. Wisitsoraat, A. Tuantranont and T. Kerdcharoen, “Synthesis of Vertically Aligned Open-end Carbon Nanotubes Using CVD with Water Etching Technique”, Siam Physics Congress 2009, March 19-21, 2009, Cha-am Methavalai Hotel, Phetchburi, Thailand.

2. W. Donkrajang, S. kladsomboon, C. Wongchoosuk and T. Kerdcharoen, “Study of Interactions between Metalloporphyrins with Various Volatile Substances Using Computational Quantum Mechanics and Molecular Dynamics simulations”, 13th Annual National Symposium for Computational Science and Engineering (ANSCSE-2009), March 25-27, 2009, Kasetsart University, Bangkok, Thailand.

3. P. Lorwongtragool, C. Wongchoosuk, A. Udomvech and T. Kerdcharoen, “Computational studies on the dynamics and trajectories of Li⁺ intercalated into single-walled carbon nanotube”, 13th

Annual National Symposium for Computational Science and Engineering (ANSCSE-2009), March 25-27, 2009, Kasetsart University, Bangkok, Thailand.

4. C. Wongchoosuk, S. Choopun, A. Tuantranont and T. Kerdcharoen, "Application of a portable electronic nose based on Au-doped ZnO nanostructure sensors for alcohols discrimination", The 2nd Progress in Advance Materials; Micro/Nano Materials and Applications (PAM-2008), January 16-18, 2008, Kosa Hotel, Khon Kaen, Thailand.

5. C. Wongchoosuk, M. Lutz, A. Tuantranont and T. Kerdcharoen, "Possibility of electronic nose for health-care monitoring", Proceedings of The 1st Symposium on Thai Biomedical Engineering (ThaiBME-2007), December 18-19, 2007, Rangsit University, Thailand.

6. C. Wongchoosuk, M. Lutz, A. Tuantranont and T. Kerdcharoen, "Human body odor monitoring using artificial olfaction devices", German-Thai Symposium on Nanoscience and Nanotechnology (GTSNN-2007), September 27-28, 2007, Chonburi, Thailand.

7. T. Thaneerananon, C. Wongchoosuk and T. Kerdchareon, "Modeling molecular structures and interactions of porphyrazine (Pz) with various alcohols sensing",

Proceeding of the 33rd Congress on Science and Technology of Thailand (STT-33), October 18-20, 2007, Walailak University, Nakhon Si Thammarat, Thailand.

8. N. Sreesarakham, C. Wongchoosuk and T. Kerdcharoen, "Application of an electronic nose for classification of Thai-instant coffees", Proceeding of the 33rd Congress on Science and Technology of Thailand (STT-33), October 18-20, 2007, Walailak University, Nakhon Si Thammarat, Thailand.

9. S. Traipop, C. Wongchoosuk, M. Lutz and T. Kerdcharoen, "The classification of Thai herbs using artificial olfaction device", Proceeding of the 33rd Congress on Science and Technology of Thailand (STT-33), October 18-20, 2007, Walailak University, Nakhon Si Thammarat, Thailand.

10. R. Ngenhlor, C. Wongchoosuk and T. Kerdcharoen, "Design of artificial olfaction devices for replacing human nose", The 1st Thailand National Nanotechnology Conference on Nanomaterials, Pharmaceutical, Devices and Application (NanoThai-2007), August 14-16, 2007, Chiang Mai, Thailand.

11. C. Wongchoosuk and T. Kerdcharoen, "Adsorption of volatile organic compounds

onto carbon nanotubes and graphene sheet as studied by density functional theory", The 1st Thailand National Nanotechnology Conference on Nanomaterials, Pharmaceutical, Devices and Application (NanoThai-2007), August 14-16, 2007, Chiang Mai, Thailand.

12. C. Wongchoosuk, S. Kongsuk, P. Singjai and T. Kerdcharoen, "Molecular dynamics simulations of functionalized carbon nanotube in water", 11th Annual National Symposium for Computational Science and Engineering (ANSCSE-2007), March 28-30, 2007, Prince of Songkla University, Phuket campus, Thailand.

13. C. Wongchoosuk, S. Unai, K. Katanyukunanon and T. Kerdcharoen, "Demonstration apparatus of atomic force microscope for nanoscience study" 32nd Congress on Science and Technology of Thailand (STT-32), October 10-12, 2006, Bangkok, Thailand.

14. C. Wongchoosuk, A. Udomvech and T. Kerdcharoen, "The geometry and electronic structure of the finite-sized functionalized single-walled carbon nanotubes", 10th Annual National Symposium for Computational Science and Engineering (ANSCSE-2006), March 22-24, 2006, Chiang Mai University, Thailand.

15. C. Wongchoosuk, A. Udomvech and T. Kerdcharoen, “The electronic structure of functionalized single-walled carbon nanotubes”, 31st Congress on Science and Technology of Thailand (STT-31), October 18-20, 2005, Suranaree University of Technology, Nakhon Ratchasima, Thailand.

AWARDS & HONORS

-Faculty of Science's Students with Talent and Achievement in Research of Physics Department (SC STAR of Physics 2010), 2010

-Japan-East Asia Network of Exchange for students and Youth (JENESYS)

Fellowship, Japan Society for the Promotion of Science (JSPS), Research at Nagoya University for 3 months with Prof. Stephan Irle, 2010.

-Outstanding Research Award of the Thailand Research Fund (TRF), “Electronic Nose for Agriculture and Food”, 2008.

-The 2nd Winner Poster Award in Devices & Others Session, The 2nd Progress in Advance Materials; Micro/Nano Materials and Applications (PAM-2008), Khon Kaen, Thailand, 2008.

-The Best Poster Award in Material Applications and Industrials Session, The 1st Thailand National Nanotechnology Conference on Nanomaterials, Pharmaceutical, Devices and Application

(NanoThai-2007), Chiang Mai, Thailand, 2007.

-First Class Honors and Outstanding Student Award, Science, PSU, Songkhla Thailand, 2005.

HOME ADDRESS

98/40 M.2 Soi Cityhome-saimai
Saimai Bangkok 10220 Thailand

MOBILE TEL.

0-29098643

E-MAIL

boy_nanotube@yahoo.com

WEBSITES

<http://nano-modern.blogspot.com>

<http://boy-nano.blogspot.com>